UNIVERSITY OF CRETE

DEPARTMENT OF PHYSICS

PhD THESIS

A multi-wavelength Study of Extragalactic Supernova Remnants

Maria Kopsacheili

Advisor: *Professor* Andreas Zezas - University of Crete

UNIVERSITY OF CRETE
DEPARTMENT OF PHYSICS
Institute of Astrophysics

PHD THESIS

Doctor of Philosophy
of
- Astrophysics -

Defended by
Maria Kopsacheili

A multi-wavelength Study of Extragalactic Supernova Remnants

COMMITTEE

Professor	Andreas Zezas	-	University of Crete
Professor	Iossif Papadakis	-	University of Crete
Associate Professor	Vassiliki Pavlidou	-	University of Crete
Professor	Vassilis Charmandaris	-	University of Crete
Research Director	Pablo Reig	-	University of Crete
Research Director	Panayotis Boumis	-	National Observatory of Athens
Professor	Despina Hatzidimitriou	-	National and Kapodistrian University of Athens

Date of the defense:
22/04/2021

Περὶληψη

Τα Υπολείμματα Υπερκαινοφανών (ΥΥ) παίζουν σημαντικό ρόλο στο διαστρικό μέσο (ΔΜ). Παρέχουν μεγάλα ποσά ενέργειας και εμπλουτίζουν το ΔΜ με βαριά στοιχεία. Η μελέτη των πυρηνικής κατάρρευσης ΥΥ μπορεί να μας δώσει πληροφορίες σχετικά με τον τρέχοντα ρυθμο δημιουργίας αστέρων μεγάλης μάζας, μιας και αποτελούν το τελευταίο στάδιο ζωής αστέρων μεγάλης μάζας. Συστηματική μελέτη πλυθησμων ΥΥ μπορει να μας δώσει πληροφορίες για την ανατροφοδότηση στο ΔΜ.

Σε αυτη τη διατριβή, σκοπός μας είναι να παρέχουμε νέα εργαλεία, που θα επιτρέψουν τη μελέτη διαφορετικων πληθυσμών ΥΥ, καθως και τη σύγκριση μεταξυ διαφορετικών μελετών και μοντέλων. Επίσης παρουσιάζουμε νέα υποψήφια ΥΥ σε κοντινούς γαλαξίες, αυξάνοντας σημαντικά τον αριθμό των γνωστών ΥΥ.

Κατασκευάζουμε νέα διαγνωστικά για την ταυτοποίηση ΥΥ στο οπτικό μέρος του φάσματος, πιο αποτελεσματικά σε ΥΥ χαμηλής διέγερσης, σε αντίθεση με το σύνηθες κριτήριο του [S II] $\left(\lambda\lambda 6717, 6731\text{ÅÅ}\right)$ /$H\alpha$. Τα νέα διαγνωστικά συνδυάζουν λόγους απαγορευμένων γραμμών εκπομπής σε 2 και 3 διαστάσεις. Επίσης προτείνουμε ένα διαγνωστικό μίας διάστασης που χρησιμοποιεί τη γραμμή [O I] και μπορεί να αυξήσει τον αριθμό των ταυτοποιημένων ΥΥ μέχρι $\sim 30\%$ σε σύγκριση με το διαγνωστικό του [S II] /$H\alpha$.

Επιπλέον ταυτοποιούμε ΥΥ στους γαλαξίες NGC 45, NGC 55, NGC 1313 *και* NGC 7793 ακολουθώντας έναν τελείως αυτοματοποιημένο τρόπο. Παρουσιάζουμε 97 υποψήφια ΥΥ (84 εκ των οποίων είναι νέες ταυτοποιήσεις). Η αυτοματοποιημένη προσέγγιση για την ταυτοποίση των ΥΥ, μας επιτρέπει να υπολογίσουμε την πληρότητα του δείγματος (δηλαδή το πόσο πλήρες ή μη πλήρες είναι το δείγμα μας) και να κατσκευάσουμε την Hα και την δύο διαστάσεων [S II] - Hα συναρτήσεις λαμπρότητας απαλλαγμένες από εφέ επιλογής. Εισάγουμε επίσης τη συνάρτηση διέγερσης βάσει της ορθογώνιας απόστασης των ΥΥ από τη γραμμή [S II] /$H\alpha = 0.4$. Βρίσκουμε ότι υπάρχει μια τάση για τα πιο λαμπρά ΥΥ να παρουσιάζουν χαμηλότερη διέγερση. Αυτό συμβαίνει πιθανώς γιατί τα πιο λαμπρά ΥΥ βρίσκονται σε περιοχές αυξημένου Hα, ή μέσα σε περιοχές ιονισμένου υδρογόνου.

Παρακινούμενοι από την έλλειψη θεωρητικών μοντέλων για την κατανομή λαμπροτήτων των ΥΥ, αναπτύσσουμε έναν φορμαλισμό για την κατασκευή θεωρητικών συναρτήσεων λαμπρότητας. Αυτές βασίζονται σε σοκ μοντέλα που προβλέπουν τη λαμπρότητα γραμμών εκπομπής σοκ για ένα μεγάλο εύρος παραμέτρων (ταχύτητα, πυκνότητα, μαγνητικά πεδία), λαμβάνοντας υπόψη τις ταχύτητες των σοκ που βρίσκονται στη Sedov−Taylor φάση. Έτσι κατασκευάζουμε τις θεωρητικές Hα και [S II] - Hα συναρτήσεις λαμπρότητας. Η σύγκριση μεταξύ θεωρητικών και παρατηρησιακών συναρτήσεων δείχνει πολύ καλή συμφωνία.

Abstract

Supernova Remnants (SNRs) play an important role in the interstellar medium (ISM) and consequently in the entire galaxy. They provide large amounts of mechanical energy and they enrich the ISM with heavy elements. The study of core-collapse SNRs can give us information on the on-going massive-star formation, since they are the last stage of massive stars' life. Systematic study of populations of SNRs can give us information on their physical properties and on their feedback to the ISM.

In this thesis, we aim to provide new tools, which will allow the study of different populations of SNRs, as well as, the comparison between different studies and models. We also present new candidate SNRs in nearby galaxies, increasing significantly the number of known SNRs.

We construct new diagnostics for the optical identification of SNRs which are more efficient in low excitation SNRs, unlike the commonly used [S II]($\lambda\lambda 6717, 6731$ ÅÅ)/Hα diagnostic. These new diagnostics combine emission-line ratios of strong forbidden lines, in 2 and 3 dimensions. We also propose a 1-dimension diagnostic that uses the [O I]($\lambda 6300$ Å) line and can increase the number of identified SNRs up to $\sim 30\%$, compared to the [S II]/Hα diagnostic.

In addition, we identify SNRs in the galaxies NGC 45, NGC 55, NGC 1313, and NGC 7793 following a totally automated method. We present 97 candidate SNRs (84 of which, are new identifications). The automated approach for the SNR identification, allows us to calculate the incompleteness and construct the Hα and the joint Hα - [S II] luminosity functions, free of selection effects. We also introduce the excitation function based on the orthogonal distance of SNRs from the [S II]/H$\alpha = 0.4$ line. We find that there is a trend for more luminous SNRs to exhibit lower excitation. This is probably due to the fact that the more luminous SNRs are in regions with increased Hα background, or embedded in H II regions.

Motivated by the lack of theoretical models for the luminosity distribution of SNR populations, we develop a formalism for the construction of theoretical luminosity functions. These are based on shock models that predict the emerging emission-line luminosity of shocks for a wide range of parameters (velocity, density, magnetic fields) coupled with the velocity of shocks in the Sedov-Taylor phase. This way, we construct theoretical Hα and the joint (Hα - [S II]) luminosity functions. The comparison between theoretical luminosity functions and the observational ones, shows very good agreement.

To my family...

Acknowledgements

First of all, I would like to thank my advisor Andreas Zezas, for his guidance all these years, his patience, his support, for always being there when I needed him and for his insistence on following methods sometimes more difficult but always better!

I would also like to thank Ioanna Leonidaki and Panayotis Boumis, with whom I did my first steps in astronomy, in 2014, and since then, they are next to me discussing scientific issues but also as good friends.

I would like also to thank the professors from the University of Crete: V. Charmandaris, N. Kylafis, I. Papadakis, V. Pavlidou, P. Reig, K. Tassis, for the useful discussions and the advice. I am greatly thankful to the personnel of Skinakas, A. Steiakaki, A. Kougentakis, G. Paterakis, E. Tsentelierou, and E. Palaiologou for their assistance in technical and not only issues, and their help during the observing nights.

I want also to thank my colleagues and friends, from the University of Crete: R. Skalidis, T. Diáz, J. Kypriotakis, P. Sell, J. Andrews, S. Williams, G. Maravellias, V. Pelgrims, K. Kouroumpatzakis, K. Kovlakas, P. Bonfini, D. Blinov, C. Casadio, A. Konstantinou, E. Kyritsis, J. Liodakis, and all the people from office 230, for the useful discussions and the great environment all these years.

A special thank to my friends that I first met at the Observatory of Athens, M. Kourniotis, Z. Spetzieri, A. Fytsilis, S. Derlopa, A. Chiotellis, S. Akras, for their support and the useful scientific discussions. And also I want to thank D. Hatzidimitriou from the University of Athens, that since my master, has been very supportive to me.

I want to especially thank Konstantina Anastasopoulou whom I met at the university of Crete, and she became a bosom friend, that always supports me and listens to me on a daily basis..

Last but not least, I want to thank Giorgos and my family, Alexandra, Amalia, and Vassilis, for their patience, for their immense support, for always being next to me, and for not letting me loose my courage. For the same reasons I want also to thank my friends Efi, Katerina and Nikos.

Contents

List of Figures

List of Tables

1

Introduction

Supernova Remnants (SNRs) are objects of great importance for the Interstellar Medium (ISM) and by extension for galaxies. They provide large amounts of mechanical energy into the ISM and they enrich it with heavy elements. They are related to the star-formation process within a galaxy, since under appropriate conditions of the local ISM the compression caused by the shock wave can trigger new-star formation. In addition, a complete census of the SNRs in a galaxy can give us information about the recent massive star formation rate (SFR) since they depict the last stage of the life in core-collapse massive stars ($M > 8\,M\odot$).

In our Galaxy there are ~ 295 known SNRs (Green 2019). The study of SNRs in our Galaxy has the significant advantage of resolving their structure, enabling the detailed investigation of the nebula, the evolution processes, and its interaction with the surrounding ISM. Systematic studies of Galactic SNRs in different wavelengths (e.g. Milisavljevic & Fesen 2013; Boumis et al. 2009) have yielded important information on the physics and kinematics of the shock. However, Galactic SNRs are affected by extinction within the Galaxy, which can obscure them especially in optical and the soft X-ray wavebands. In addition, the study of Galactic SNRs is limited by the difficulty in determining their distances,

Some of these limitations can be relieved by studies of extragalactic SNRs. They offer the opportunity of examining SNRs in different environments (different densities, galaxies with different metallicities etc.) giving a more complete image of their feedback with ISM with different properties. Moreover, the uncertainty in the distance of extra-galactic SNRs is minimized, since their distances (the distance of the host galaxy) is known. Studies of other galaxies have revealed a large number of SNRs and properties of their populations (i.e. luminosity distribution, size distribution, e.g. Asvarov 2014; Leonidaki, Boumis, & Zezas 2013; Blair et al. 2013; Blair & Long 1997).

In addition to the study of Galactic and extra-galactic SNRs, what can give us a more complete picture of their properties, is the multi-wavelength study. Different wavelengths give information on different evolutionary stages of SNRs, different physical mechanisms, and different regions of the shock. Also, models (i.e. shock models, morphokinematic simulations etc.) can reveal the physical properties of SNRs that cannot be obtained in other way. The combination of all of them, especially with new, higher resolution observing techniques, can give a more global image of their physical properties and their feedback to the ISM.

In the following sections we present a basic introduction on SNRs. More specifically, in § 1.1 we discuss the different types of supernovae and their physical mechanism. In 1.2 and § § 1.3 the SNR types and the evolutionary stages of SNRs are described. In § 1.4 the different radiation mechanisms of SNRs are presented and in § 1.5 we briefly discuss the feedback of the SNRs to the ISM. In § 1.6, we present the motivation for this work.

1.1 Supernovae

Supernova result from the gravitational collapse of a stellar object. Depending on the presence or absence of different optical emission lines in their spectra, they are classified in two main categories.

1.1.1 Types of supernova

Type I Supernova

Type I supernovae are characterized by lack of hydrogen-Balmer lines in their spectra. This category can be divided into more subcategories: supernova of type Ia, Ib and Ic. Type Ia supernovae present silicon absorption-lines and sometimes weak helium absorption-lines in their spectra, while type Ib supernova show only helium lines. In the spectra of Type-Ic supernovae both helium and silicon lines are absent. The light curve of type Ia supernovae is characterized by a sharp peak and a steep decline. In the light curves of type Ib and Ic supernovae the peak luminosity is usually lower and the decline shallower. These light curves can be seen in Figure 1.1. Type I SN come from stars that have lost their outer envelope of hydrogen.

Type II Supernova

The spectra of type II supernova (SN) are characterized by hydrogen-emission lines. These supernova can be further categorized in supernova type IIb, II-L, II-P and IIn, based on their spectra and the shape of their light curves. Type IIb supernovae (SNe) begin having strong hydrogen lines but they lose them ending up to type Ib. Type IIb supernova probably come from a progenitor that has lost part of its hydrogen envelope. Their light curve is similar to this of type Ib. Type II-P and II-L supernovae present broad hydrogen lines in their spectra. They usually come from the collapse of single stars. Type II-P present a constant brightness for many years which results in a plateau in their light curve, while in type II-L the luminosity declines linearly after the peak. Type IIn supernovae are characterized by narrow hydrogen lines. This type comes more likely from luminous blue variables that before the final explosion have undergone outbursts, loosing part of their outer atmosphere. The light curves of type II supernovae are shown also in Figure 1.1.

1.1.2 Supernova explosion mechanism

From the spectra of SNe, we can derive information on the explosion mechanisms. Two basic categories of SN, indicate two explosion mechanisms. These are the thermonuclear and the core-collapse SNe.

Thermonuclear Supernovae

These result in type Ia supernovae. The lack of H and He lines in their spectra indicates a common progenitor, that it has lost its outer envelope, suggesting a white dwarf. A carbon-oxygen white dwarf, which belongs to a binary system, accretes mass from a donor companion and when it reaches the Chandrasekhar limit ($\sim 1.4\mathrm{M}_\odot$), the electron degeneracy pressure cannot resist gravity and the collapse begins. The collapse increases the temperature of carbon and oxygen and they undergo fusion. The fusion takes place explosively since the thermal conductivity of the single degenerate star is high and the energy production rate has a very strong dependence on temperature. Type Ia SNe can come up via two ways: i) the single-degenerate model where a white dwarf receives mass from a main-sequence star; ii) the double-degenerate model where two white dwarfs are in the same binary system losing energy due to gravitational waves and the white dwarfs finally collide. A representation of the type Ia formation-process

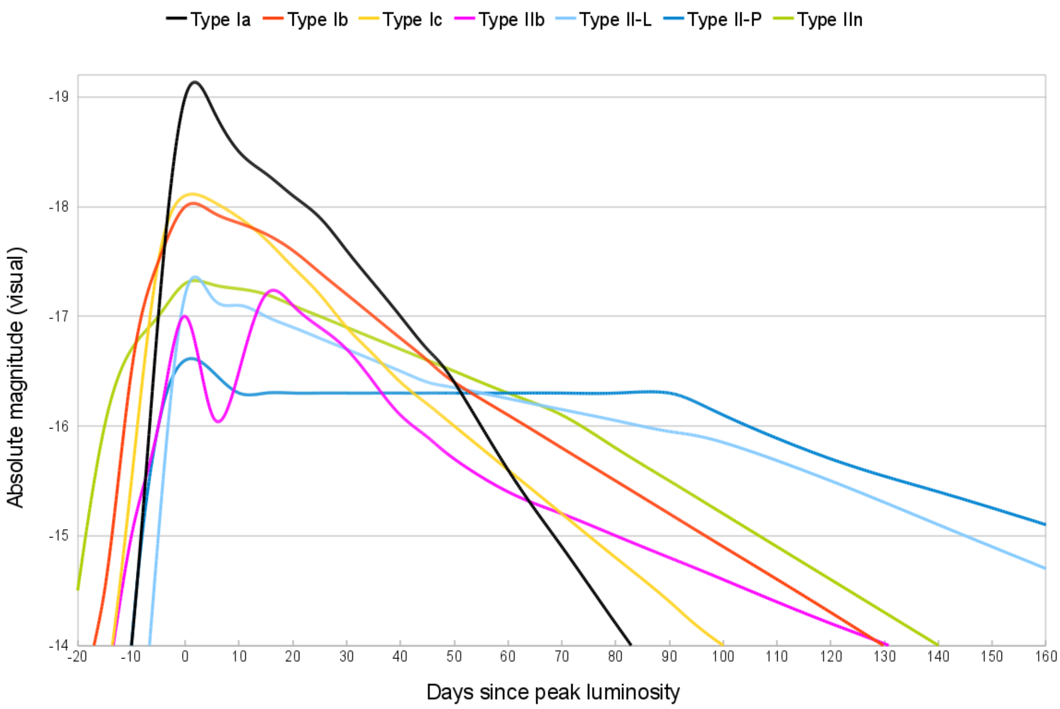

Figure 1.1: Light curves for the different supernova types.

1

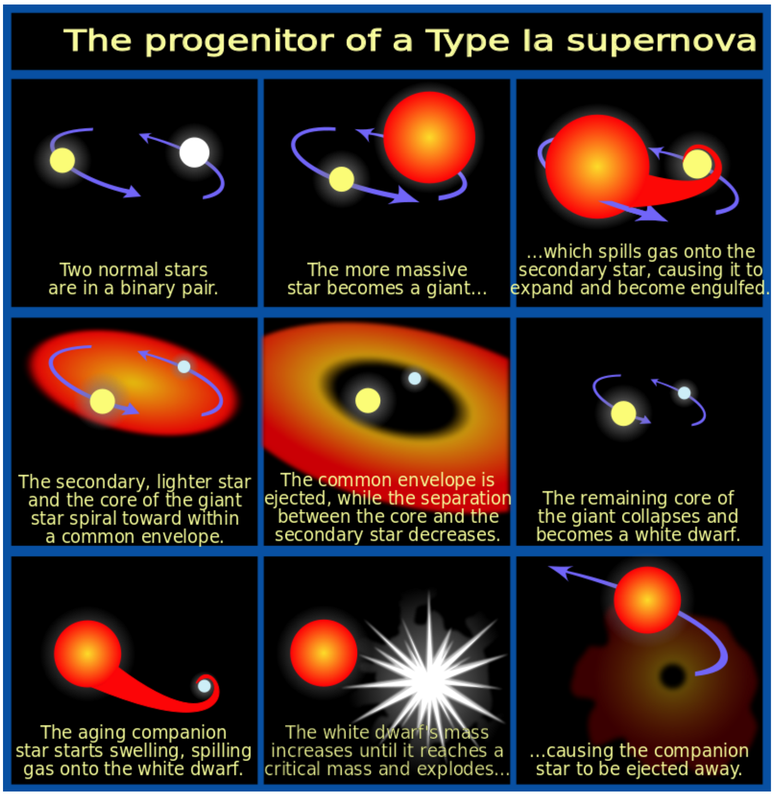

Figure 1.2: Formation process of type Ia supernova. (Credit: NASA, ESA and A. Feild (STScI))

is shown in Figure 1.2. Type Ia supernovae can take place in galaxies of all types. The fact that they come from white dwarfs ($\sim$ 15 billion years), makes them rare compared to other types of SNRs.

Core-collapse Supernovae

Massive stars ($> 8\mathrm{M}_{\odot}$) can fuse heavier elements than Sun-like stars. The stellar equilibrium is maintained from the energy generated by fusion reactions that acts against gravity. The fusion starts from hydrogen and helium and progresses up with the fusion of higher atomic number elements. Following this process, the star is layered in shells as is shown Figure 1.3, and the core consists of iron and nickel. No further fusion can take place to resist against gravity. The temperature in the core increases and hence part of the core breaks down to lighter elements releasing free protons that are combined with free electrons forming neutrons and neutrinos. Finally, gravity dominates, the core implodes, and the outer layers collapses inwards. The representation of a core-collapse supernova is presented in Figure 1.4. The energy that is released from a such explosion

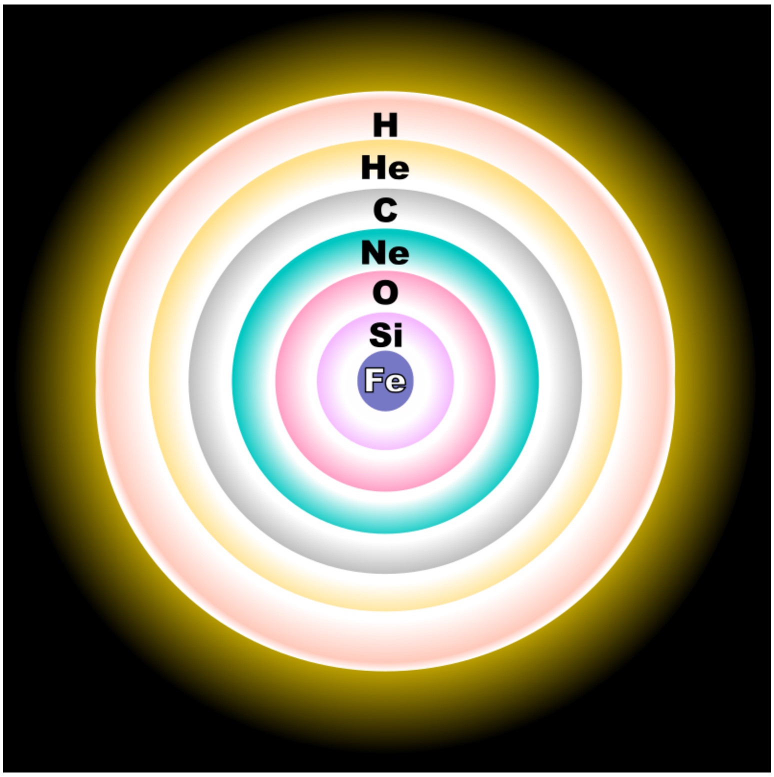

Figure 1.3: Onion-like structure of massive star before supernova explosion. (Credit: R. J. Hall)

can reach $\sim 10^{53}$erg. This type of SN is more common in spiral galaxies, and more specifically, in star forming regions, where massive stars are located.

1.2 Evolution Phases of Supernova Remnants

During the SN explosion a significant amount of mass is ejected and propagates with supersonic velocities sweeping up material of the surrounding medium creating a shock wave. When the mass of the swept up material becomes comparable with the ejected mass, the shock wave decelerates, cools down and finally dissipates in the ISM and fades away. The evolution of a SNR is divided in four stages: a) Free-expansion Phase, b) Sedov-Taylor or Adiabatic Phase, c) Snowplow Phase and d) Dissipation Phase.

a) Free − expansion Phase

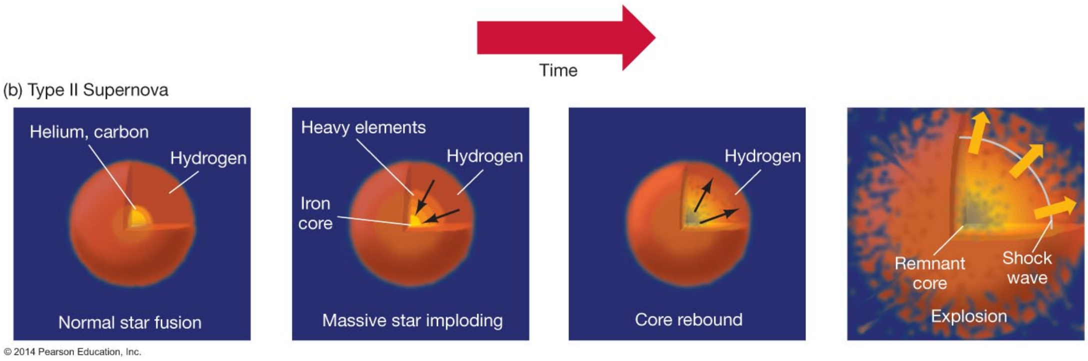

Figure 1.4: Formation process of type II supernova. (2011 Pearson education Inc.)

A supernova explosion ejects mass ($\mathrm{M_{ej}}$) with energy $\mathrm{E_0} = \sim 10^{51}$ erg. The velocity of the ejected mass is $\sim 10^4$ km/s, much higher than the sound speed in the ISM, creating a shock wave. The shock wave propagates outward heating up the surrounding medium to $\sim 10^7$ K and sweeping up material. In this phase, the mass of the swept up material is negligible compared to the ejecta mass and hence the shock wave expands almost with constant velocity. That is why this phase is called "free-expansion phase".

Since most of the explosion energy appears as kinetic energy, the mean velocity of the ejecta v_{ej} is given by the relation:

$$v_{ej} = \sqrt{\frac{2E_0}{M_{ej}}} \tag{1.1}$$

The radius R_s of the shock that propagates with constant velocity as function of the time t is:

$$R_s = v_{ej} t \tag{1.2}$$

When the mass of the swept up material (M_s) becomes equal to the ejected mass the shock decelerates and the free-expansion phase end. At this point:

$$M_s = M_{ej} = \frac{4}{3}\pi\rho R^3 \tag{1.3}$$

where ρ is the density of the local ISM. The free-expansion phases lasts 100-1000 years.

b) Adiabatic or Sedov − Taylor Phase

The Sedov-Taylor phase begins when the mass of the swept-up material ($\mathrm{M_s}$) becomes comparable to the ejected mass ($\mathrm{M_{ej}}$). The density of the swept up material is higher than that of the ejected material creating a contact-discontinuity between the two materials. Then a reverse shock is created and propagates inwards heating up the interior of the SNR. The reverse shock moves slower than the first shock since the kinetic energy has been converted to thermal energy. The temperature of the interior of the SNR is so high that to first approximation all the atoms are ionized, no recombination takes place and hence the energy losses by the emitted radiation are very small. In order to describe this phase we use the self-similar solution of Sedov-Taylor (Sedov 1959; Taylor 1950). The motion equation is:

$$\frac{d}{dt}(M_{ej}\frac{dR_s}{dt}) = 4\pi R_s^2 p_i \tag{1.4}$$

where p_i the pressure of the material in the interior of the SNR.

In the adiabatic expansion the pressure can be written as a function of the explosion energy and the volume of the SNR as:

$$p_i = (\gamma - 1)\frac{E_0}{V} \tag{1.5}$$

So finally,

$$\frac{d}{dt}\Big(\frac{R_s^3}{3}\rho_0\frac{dR_s(t)}{dt}\Big) = \frac{E_0}{2\pi R_s} \tag{1.6}$$

We can consider the radius R_s as $R_s = Ct^n$. Inserting in 1.6 we obtain

$$n = \frac{2}{5} \ \ and \ \ C = \Big(\frac{25E_0}{4\pi\rho_0}\Big)^{1/5} \tag{1.7}$$

Thus:

$$R = \Big(\frac{25E_0}{4\pi\rho_0}\Big)^{1/5} t^{2/5} \tag{1.8}$$

and

$$v_s = \frac{2}{5}\Big(\frac{25E_0}{4\pi\rho_0}\Big)^{1/5} t^{-3/5} \tag{1.9}$$

In order to calculate the temperature of the shock we use the Rankine-Hugoniot conditions for the limit between the front and the post-shock and the ideal gas law. So finally,

$$\begin{gathered} R_s = 1.54 \times 10^{19}\, E_{51}^{1/5} n_0^{-1/5} t_3^{2/5}\, (cm) \\ u_s = 1950\, s^{-1} E_{51}^{1/5} n_0^{-1/5} t_3^{-3/5}\, (km) \\ T_s = 5.25 \times 10^{7} E_{51}^{2/5} n_0^{-2/5} t_3^{-6/5}\, (K) \end{gathered} \tag{1.10}$$

where n_0 is the hydrogen density in ISM in units of cm^{-3}, $E_{51} = E_0/10^{51}\,erg$, $t_3 = t/10^3$ years (Draine 2011).

c) Snowplow Phase

The shock wave keeps expanding sweeping up more and more material: that is why this phase is called the snowplow phase. The density just behind the shock increases and the temperature decreases. However, the interior of the SNR is still hot and the pressure forces the SNR to expand more. Thus the SNR consists of a cool dense shell that encloses hot material. We consider the interior as adiabatic. Hence the pressure $\mathrm{p_i}$ in the interior is:

$$\mathrm{p_i} = \rho_\mathrm{i}^\gamma \tag{1.11}$$

From mass conservation in the interior the density is:

$$\rho_\mathrm{i} = \frac{3\mathrm{M_{ej}}}{4\pi \mathrm{R_s^3}} \tag{1.12}$$

From 1.11 and 1.12 the pressure can be written as:

$$\mathrm{p_i} = (\frac{3\mathrm{M_{ej}}}{4\pi})^\gamma \mathrm{R_s^{-3\gamma}} \tag{1.13}$$

The pressure forces the SNR to expand more. The motion equation of the shock is:

$$\frac{\mathrm{d}}{\mathrm{dt}}(\mathrm{M_{ej}}\frac{\mathrm{dR_s}}{\mathrm{dt}}) = 4\pi \mathrm{R_s^2 p_i} \tag{1.14}$$

Replacing the $\mathrm{M_{ej}}$ from 1.12 and $\mathrm{p_i}$ from 1.11:

$$\frac{\mathrm{d}}{\mathrm{dt}}(\mathrm{R_s^3}\frac{\mathrm{dR_s}}{\mathrm{dt}}) = \frac{3}{\rho_0}(\frac{3\mathrm{M_{ej}}}{4\pi})^\gamma \mathrm{R_S^{2-3\gamma}} \tag{1.15}$$

Let us suppose that $\mathrm{R_s(t) = Ct^n}$. Replacing $\mathrm{R_s}$ in 1.15 we obtain:

$$\mathrm{c^4 n(n-1)t^{4n-2}} = \frac{3}{\rho}(\frac{3\mathrm{M_{ej}}}{4\pi})^\gamma \mathrm{C}^{2-3\gamma}\mathrm{t}^{(2-3\gamma)\mathrm{n}} \tag{1.16}$$

For $\gamma = 5/3$

$$\mathrm{n} = \frac{2}{7} \ \text{ and } \ \mathrm{C} = 7\Big[\frac{6}{\rho}(\frac{3\mathrm{M_{ej}}}{4\pi})^{5/3}\Big]^{1/7} \Rightarrow \mathrm{R_s(t)} = 7\Big[\frac{6}{\rho}(\frac{3\mathrm{M_{ej}}}{4\pi})^{5/3}\Big]^{1/7}\mathrm{t}^{2/7} \tag{1.17}$$

At this point, the shock velocity can be obtained by the derivative of $\mathrm{R_s(t)}$:

$$\mathrm{v_s} = 2\Big[\frac{6}{\rho}(\frac{3\mathrm{M_{ej}}}{4\pi})^{5/3}\Big]^{1/7}\mathrm{t}^{-5/7} \tag{1.18}$$

d) Dissipation Phase After the snowplow phase, the velocity of the shock wave is very low ($\sim 150\,\mathrm{km/s}$) and keeps decreasing until it becomes comparable with the velocity of the surrounding ISM. The SNR dissipates within the ISM. This is the last stage of its evolution.

1.3 Supernova Remnant Type

The morphology of SNRs is determined by the progenitor, the explosion mechanisms, and the local ISM properties. Thus, we have three main categories of SNRs, based on their morphology:

a) Shell − like SNRs

These are the SNRs, the radiation of which comes mainly from the outer edge of the expanding shell and they are viewed as rings. This is the result of a 3D shell-like structure projected in 2 dimensions. This is because we see more excited material along the line of sight at the edges, compared to more central regions. This effect is known as limb brightening. The shell-like structure is observed in X-rays and in optical wavelengths. However, the ejecta in the interior of the SNR cause also X-ray emission.

b) Plerion or Crab − like SNRs

In this type of SNRs, the radiation comes mostly from the central region of the SNR and not from the edges. Responsible for this radiation, is the pulsar wind from a pulsar at the center of the SNR, where relativistic electrons emit synchrotron radiation under the effect of the strong pulsar magnetic field. This radiation spans a broad energy range from X-ray or even γ-rays . For this reason, plerions SNRs are also known as planetary wind nebulae (PWN). A typical example of a such SNR, is the Crab nebula.

c) Composite SNRs

These SNRs are viewed either as shell-like or like plerions, depending on the wavelength that we observe them. The plerionic-composite SNRs appear like plerionic SNRs in non-thermal radio and X-ray radiation. The non-thermal radiation comes from the PWN. However, the shell emits thermal radiation and hence in optical and the thermal X-ray wavelengths they appear like shell-like.

Another sub-category is the mixed-morphology SNRs. These SNRs present non-thermal emission from their shell, and thermal emission from their center. This thermal emission indicates that it does not come from a pulsar wind, but from hot plasma in the interior of the SNR.

1.4 Radiation from Supernova Remnants

The emission of an SNR in different wavelengths, depends on its interaction with the ISM. This depends on the explosion energy, the properties of the medium in which the SNR evolves, and the evolutionary stage of the SNR.

Optical emission

Optical SNRs are dominated by Balmer and forbidden emission lines (of oxygen, nitrogen, sulfur etc.). Photons with energies > 13.6 keV ionize hydrogen atoms creating hydrogen ions and free electrons. These electrons are captured by ions (hydrogen nucleus) emitting photons and creating excited hydrogen atoms. These captured electrons go to lower and lower energy levels until they reach the ground state. Those that reach at the state $\mathrm{n} = 2$ cause the Balmer emission lines. The most intense Balmer lines are the Hα line, that is created by the electrons that go from the state $\mathrm{n} = 3$ to the state $\mathrm{n} = 2$ and Hβ line by electrons that go from the state $\mathrm{n} = 4$ to the state $\mathrm{n} = 2$.

Forbidden lines are the result of the collision of electrons with atoms like nitrogen, oxygen, and sulphur exciting them to metastable energy states. Since the density is very low, the de-excitation happens spontaneously, resulting in the emission of forbidden lines.

The aforementioned mechanisms that produce these emission lines are dominant in evolved SNRs where the shock velocity is low. However, there are young SNRs which also present optical emission. In such SNRs, there are high-density regions (clumps) which decelerate the forward or the reverse shock to velocities $200\,\mathrm{km\,s^{-1}}$. Such SNR is Cas A which presents optically emitting clumps bright in [S II]$\lambda\lambda6716, 6731$ (Vink 2020). Another type of young SNRs that present optical emission, is the Balmer dominated SNRs. In these SNRs there is a neutral hydrogen region which interacts with the surrounding shock-excited ions and electrons, creating atoms excited to higher energy levels. The de-excitation of these electrons results in Balmer-lines emission. Since, this process requires the presence of neutral hydrogen in the circumstellar region, these SNRs are usually Type Ia.

X − ray emission

X-ray emission in SNRs can be thermal or non-thermal (synchrotron). The thermal X-ray radiation consists of thermal continuum emission and line emission. The thermal continuum comes from collisions between electrons and ions. If the ion captures an electron (recombination) the emission is called free-bound emission, while if it is not captured but the two particles simple interact, the emission is called free-free or Bremsstrahlung. The line emission in X-rays is caused by collisional excitation (by the electrons that cause the continuum emission) and by recombination. The high temperatures in the shells, and thus the thermal X-ray emission, is caused by the SNR shock. For high shock velocities ($u_{shock} \geqslant 10\, c_{sound}$) the relation between temperature and shock velocity is:

$$k_B T = \frac{2(\gamma - 1)}{(\gamma + 1)^2} \mu m_p v_{shock}^2 = 29 (\frac{v_{shock}}{5000\, km\, s^{-1}})^2\, keV \tag{1.19}$$

where $\gamma = 5/3$ is the adiabatic index of the plasma, m_p the proton mass and μ the average mass of the particles in units of the proton mass (Vink 2017). However, sometimes the predicted and the observed values of the temperature can be quite different. This can happen for two reasons: i) X-ray spectra give the electron temperature, while eq. (1.19) the temperature of the whole plasma, which is not in thermal equilibrium yet; ii) Eq. 1.19 is based on conservation of thermodynamic quantities and does not account for the possible energy that is used to accelerate particles to very high energies (Vink 2017).

X-ray spectra of SNRs can be indicative of the type of the SN explosion (Type Ia or Type II) from which they come. Usually, spectra dominated by Fe lines, are indicative of Type Ia SNRs, while SNR with spectra dominated by O, Mg, and Ne emission lines, are associated with Type II SN (Vink 2017).

The non-thermal X-ray emission in SNRs results from synchrotron radiation. This emission is dominant in pulsar wind nebulae (PWNe). However, more rarely, non-thermal emission has been observed also in the shells of SNRs, from particles that are accelerated by the shock waves. More specifically, from the few SNRs in which non-thermal X-ray emission from shocks has been observed, only 5 can be characterized as synchrotron dominated SNRs (Williams et al. 2018).

X-ray emission is observed more often in young SNRs, where shock velocities are very high and heat the ISM to temperatures of $\sim 10^7$ K producing thermal X-ray emission. High shock velocities are also required for particle acceleration, which results in the production of non-thermal emission at the shock region. As the remnants evolve and pass to the radiative phase, the temperature of the plasma decreases, as the shock slows down, and the X-ray emission is softer until the shock velocity becomes very low ($\sim 200\, \mathrm{km\, s^{-1}}$, and the temperature is $< 10^6$ K) where no X-ray emission is observed. Hence, the X-ray emission of SNRs in that phase, comes from regions of the SNRs with shock velocities $> 200\,\mathrm{km\,s^{-1}}$ or from regions that are still hot from the shock that heated them in the past (Vink 2017). There is also a category of old SNRs, the mixed-morphology SNRs, that in the X-rays are observed as non-shell SNRs, as the emission comes only from the central region, while in radio are observed as shell-like SNRs. The explanation for this, is, that as discussed before, the shell is too cool to produce X-ray emission, while the interior is still hot from the effect of the shock in the past.

Radio emission

Radio study of SNRs is of high importance since it can reveal SNRs that cannot be detected in optical or X-ray wavelengths due to Galactic extinction. In our Galaxy 295 SNRs have been discovered (Green 2019) and only 5% of them have not been identified in radio or are very radio faint (Dubner & Giacani 2015). Radio emission is the result of synchrotron radiation from relativistic electrons.

The spectra of radio SNRs are characterized by a power-law, the spectral index of which depends on the index of the energy spectrum and consequently on the age of the SNR. According to Bell (1978a, b), old SNRs (i.e. low shock velocities) give steeper spectral indices (> 0.5) because the relativistic electrons have lost a fraction of their energy and particle acceleration is less efficient. However, observations show the opposite behaviour, i.e. young SNRs present steeper spectral indices (around 0.7). The explanation for this behavior was given by Bell, Schure, & Reville 2011 who showed that if the orientation of magnetic field is quasi-perpendicular to the shock wave, the spectral index will be steeper in young SNRs, while in the original model of Bell (1978a, b) the magnetic field was assumed to be parallel to the shock wave.

Infrared emission

Infrared observations can reveal SNRs obscured by dust. The infrared emission from SNRs can be thermal and less often non-thermal. The continuum component of the thermal emission comes from the emission of warm dust grains, while the emission lines from atomic or molecular gas. The non-thermal emission, is the result of synchrotron emission from relativistic electrons in the shock. The infrared emission-line mechanism is dominant in lower temperature shocks, resulting in recombination lines. This is the case for older SNRs or shocks that encounter dense regions. In young SNRs, the dominant mechanism for IR emission is the thermal continuum emission from dust grains that are heated by collisions with electrons and ions, responsible also for the X-ray emission of SNRs. This is the reason for the similarity of the SNR morphology in infrared and X-rays in this phase (Williams et al. 2006).

1.5 Feedback by Supernova Remnants

The explosion of a supernova releases large amounts of energy to ISM ($\sim 10^{51}$ergs) mainly in the form of kinetic energy from the ejected material which expands in the ISM at very high velocities. Among the feedback mechanisms, SNRs are the the most important dynamical ones, in terms of momentum and energy and in duration of feedback. According to numerical studies, the momentum by a single SN with explosion energy $\mathrm{E} = 10^{51}$ ergs is $1 - 5\,\mathrm{M}_{\odot}\,\mathrm{km\,s^{-1}}$ (Koo et al. 2020). The ejecta sweep up the surrounding material, creating a shock wave which expands super-sonically into the ISM heating it up to temperatures of $\sim 10^{7}$K. Therefore, SNRs (along with stellar winds from massive stars) are responsible for the hot component of the ISM (e.g. Cox & Smith 1974)

SNRs also enrich the ISM with heavy elements that have been created during the evolution of the progenitor star or during the explosion, and are delivered to the ISM during the explosion. The expelled material from the SN explosion can play an important role in the formation of dust, by the heavy elements of the expelled material that condense into dust grains (Edmunds 2017, Williams & Temim 2017).

The role of the SNRs in star-forming processes is more complex. Although in general it is considered that SNRs are fundamentally related to the star formation in a galaxy, studies have shown the most time of their lives act catastrophically, destroying molecular clouds in which stars can be formed. Only very old SNRs with velocities $< 45\,\mathrm{km\,s^{-1}}$ can compress the ISM such as to trigger star formation (e.g. Desai et al. 2010; Vanhala & Cameron 1998).

The effect of SNRs to the ISM depends mainly on their explosion energy, and the medium in which the SNR is expanding (metallicity, density, inhomogeneities, etc.) Although in most cases the explosion energy of the SNR is assumed to be 10^{51}, that is not always true and even a small difference in explosion energy (i.e. half order of magnitude), can affect significantly the output results (Cioffi, McKee, & Bertschinger 1988).

Density plays a very important role in the evolution of SNR, since the cooling rate is a function of the density. An SNR expanding in a low-density environment, has slower evolution, the cooling rates are lower and consequently, the SNR retain a larger fraction of the explosion energy. Similar is the impact of metallicity. For higher metallicities, the presence of more metals make the cooling more efficient. Thus the SNRs lose their energy faster. In other words, the available energy to be converted to thermal and kinetic energy is higher for lower density and metallicity. As the density and metallicity increase, the fraction of energy lost by radiation increases too (Cioffi, McKee, & Bertschinger 1988).

What can also affect the evolution of the SNR is possible turbulence in the surrounding ISM. These can affect the dynamical evolution of SNRs, and also the cooling rates, since they can cause the mixing of the shock with more metals (Cioffi, McKee, & Bertschinger 1988). Inhomogeneities in the ISM can also affect the SNR evolution. According to Martizzi, Faucher-Giguère, & Quataert 2015, although the evolution is qualitatively similar for uniform and non-uniform media, quantitatively there are differences that have to do with the cooling mechanisms affected by the density of the medium.

1.6 Motivation

Despite the significant number of SNR studies discovering new sources and providing detailed information on their physical properties, we still do not have a complete image of their physics, but also of their feedback to the ISM. In this thesis, we present an investigation of SNRs in nearby galaxies based on new methods, which will give us a more reliable picture of their population, which is important for addressing their properties and their feedback to the ISM.

The most commonly used diagnostic for optical identification of SNRs up to now, is the [S II]/Hα criterion. Sources with [S II]/H$\alpha > 0.4$ are considered as SNRs. This is an empirical diagnostic for SNRs in Small and Large Magellanic Clouds (MCs), suggested by Mathewson & Clarke (1973). However, this diagnostic is biased against low excitation SNRs, i.e. SNRs with low shock velocities or SNRs evolving in media too dense for efficient de-excitation. This means, that by using the [S II]/Hα criterion, we systematically miss the low excitation SNRs of a galaxy. This led us to examine new diagnostics, that account also for the low excitation SNRs. The results of this study are presented in Chapter 2. We suggest new diagnostics that combine emission-line ratios in 2 and 3 dimensions, but also a new 1D diagnostic, that can increase the number of the detected SNRs by $\sim 30\%$.

Although the [S II]/Hα criterion cannot be used as indicator of the total population of SNRs, it is useful for comparative studies between different galaxies, when the same selection criteria are considered. However, in order to do this kind of comparisons, the different samples must be free of selection effect. In Chapter 3, we present a systematic study of SNRs in 4 nearby galaxies. We follow an automated method for the identification of SNRs, which allows us to calculate incompleteness effects, and finally construct luminosity functions free of selection effects. Based on this method, we calculate the Hα and joint [S II]-Hα luminosity functions of the SNR populations in the sample of the galaxies.

The lack of theoretical predictions of physical parameters of SNR populations, motivated us to construct basic models which can be used for comparison with the observational data. In Chapter 4, we present a basic model for the calculation of theoretical luminosity functions for a wide range of physical parameters, and we compare them with the observed SNR populations.

2

A diagnostic tool for the identification of Supernova Remnants

2.1 Introduction

Study of SNR demographics and their physical properties (density, temperature, shock velocities) is very important in order to understand their role in galaxies. Their feedback to the Interstellar Medium (ISM), and consequently to the entire galaxy, is of high importance since they provide significant amounts of energy that heat the ISM and they enrich it with heavy elements. They are fundamentally related to the star-forming process in a galaxy, inasmuch as the compression of the ISM by the shock wave, under appropriate conditions, can lead to the formation of new stars. Having a complete census of SNR populations can also give us a picture of the on-going massive star formation rate (SFR) since they depict the end points of massive stars ($M > 8M\odot$).

Many photometric and spectroscopic studies of SNRs, have been carried out in our Galaxy (e.g. Milisavljevic & Fesen 2013; Boumis et al. 2009) but also in extragalactic environments (e.g. Vučetić et al. 2015; Leonidaki, Boumis, & Zezas 2013; Leonidaki, Zezas, & Boumis 2010 ; Blair & Long 1997). These studies increase the number of known SNRs, and also provide significant information about their physical and kinematic properties, as well as information on their interaction with their local

ISM. According to Green (2019; 2017) the known number of the optical Galactic SNRs is 295, while most of the studies on extragalactic environments present a few dozen SNRs per galaxy, except for a handfull of extreme cases: e.g. M83 with 225 photometric SNRs; (Blair et al. 2013; Blair et al. 2012), M33 with 220 (Long et al. 2018), M31 with 150 (Lee & Lee 2014a). The small number of observed extragalactic SNRs compared to those in our Galaxy, is the result of different sensitivity limits and also different selection criteria. The identification of SNRs in our Galaxy or the Magellanic clouds is generally based on the detection of extended non-thermal radio sources, or X-ray sources, while studies in other galaxies rely on photometric or spectroscopic measurements of diagnostic spectral lines.

The most common means of identifying SNRs in the optical regime, is the use of the flux ratio of the [S II] ($\lambda\lambda 6717, 6731$) to H$\alpha$ ($\lambda 6563$) emission lines, as first suggested by Mathewson & Clarke (1973) based on studies of SNR population in the Large Magellanic Cloud (LMC). Usually, nebulae with [S II]/Hα ratio higher than 0.4 are considered as SNRs. Indeed, we expect SNRs to give higher values of [S II] than HII regions since collisionally excited S^{+} behind the shock front gives strong [S II] emission, while in HII regions sulphur is mostly in the form of S^{++}. However, within the years, this low limit for the [S II]/Hα ratio has been slightly modified in order to take into account different interstellar densities for the [S II]/Hα ratio (Daltabuit et al. 1976), different galaxy metallicities (Leonidaki, Boumis, & Zezas 2013; D'Odorico et al. 1978), difficulties in distinguishing SNRs from HII regions on the borderline between them (Fesen, Blair, & Kirshner 1985) or strong emission from [N II] (Dopita et al. 2010). Consequently, a more robust diagnostic tool seems to be necessary. Fesen, Blair, & Kirshner 1985 recognizing this need, suggested the line ratios of [O I]/Hβ and [O II]/Hβ that seem to efficiently differentiate SNRs from HII regions.

Advanced observing techniques (multi-slit spectroscopy) give us the ability to obtain full spectral information for large numbers of sources. This, in combination with the development of advanced photoionization and shock models (Kewley et al. 2001; Allen et al. 2008) allows us to examine more accurately spectral features of nebulae and compare data with theory. Several studies have used diagnostic diagrams to separate objects based on their excitation mechanisms, like HII regions and active galactic nuclei (AGN) using 2D or multi-D diagnostics (e.g. Stampoulis et al. 2019; de Souza et al. 2017; Vogt et al. 2014; Kewley et al. 2001).

Our study focuses on diagnostic diagrams that separate SNRs from HII regions. We present a set of new diagnostic tools for the identification of optical SNRs. These models allow us to derive theory-driven diagnostics that overcome the limitation of the empirical diagnostics employed so far.

The outline of this paper is as follows. In Section 2, we describe the models we used, in Section 3, we talk about the emission line ratios that we examined, the classification method and the most accurate line ratio combination and in Section 4, we discuss our results.

2.2 Models

In order to generate an emission-line diagnostic tool that is able to separate SNRs from HII regions, we used the results from MAPPINGS III, a photoionization code (Groves et al. 2004; Dopita et al. 2002; Sutherland & Dopita 1993; Binette et al. 1985) that predicts emission-line spectra of a medium that is subject to photoionization or shock excitation (Allen et al. 2008). We obtained the line ratios from the compilation of photoionization and shock excitation model grids available in the ITERA (IDL Tool for Emission-line Ratio Analysis) tool (Groves & Allen 2010; Groves & Allen 2013).

Starburst models
ITERA includes two sets of starburst models, i.e. emission-line spectra emerging from gas photo-ionized by two different sets of stellar population models. These correspond to the spectra expected from HII regions or star-forming galaxies.

(i) Kewley2000: The first set of models are from Kewley et al. (2001). These are photoionizaton models based on stellar ionizing spectra created either by the PEGASE-2 (Fioc & Rocca-Volmerange 1997) or the Starburst99 (Leitherer et al. 1999) stellar population synthesis codes and under two star-formation scenarios: continuous and instantaneous. The ITERA library contains MAPPINGS III models for various values of the ionization parameter (ranging from 2×10^5 to $4 \times 10^8 \mathrm{cm\,s^{-1}}$) and metallicities (from 0.01 to $3\,\mathrm{Z}_\odot$ for PEGASE-2, and from 0.05 to $2\,\mathrm{Z}_\odot$ for Starburst99).

(ii) Levesque09: The second set of models is from Levesque et al. (2010). These are stellar photoionization models with an updated version of Starburst99 code (Vázquez & Leitherer 2005) with continuous star formation and instantaneous burst models, extending to a wider range of ages (0-10 Myr) and examining not only the case of standard but also of high mass-loss tracks, which better approximate the mass loss of massive stars (Levesque et al. 2010).

Shock models

Allen et al. (2008) provide a library of spectral line intensities for shock models of different velocities, magnetic parameters, abundances and densities, with and without a photoionizing precursor. From these models we used these that combine the emission from the pre and post-shocked regions which better represent the observation of unresolved sources. They cover velocity ranges from 100-1000 $\mathrm{km\,s^{-1}}$ and magnetic parameters ($\mathrm{B/n^{1/2}}$, where B is the transverse components of the preshock magnetic field and n is the preshock particle number density) from 10^{-4} to $10\mu\,\mathrm{G\,cm^{3/2}}$. They also consider different abundances (LMC, SMC, solar, twice solar and Dopita et al. 2005 solar abundance) and densities ($\mathrm{n} = 0.01, 0.1, 1.0, 10, 100, 1000\,\mathrm{cm^{-3}}$).

From these models, we have two sets of line ratios involving the most prominent optical lines for the different abundance and ISM conditions considered. One set applies to SNRs (resulting from the shock models) and another one refers to HII regions (resulting from the starburst models). In the case of shock models, each point of the set is characterized by a shock velocity, a magnetic parameter, a density and an abundance, while for starburst models it is described by the ionization parameter, age, abundance and density.

2.3 Optimal combination of lines

In order to find the optimal emission line ratios that best distinguish SNRs from HII regions, we examined two and three-dimensional diagnostics involving different lines for the full range of abundances and densities. The emission lines we opted to use are various forbidden lines, which tend to be stronger in shock-excited than in photoionized regions: [N II]($\lambda6583$), [S II]($\lambda\lambda6716, 6731$), [O I]($\lambda6300$), [O II]($\lambda\lambda3727, 3729$), [O III]($\lambda5008$).

For example Figure 2.1 presents a 3D diagram of the line ratios [S II]/Hα - [O I]/Hα - [O III]/Hβ for shock models (representing SNRs; green triangles) and starburst models (representing HII regions; red circles). As we can see shock models are quite well separated from starburst models, although there is some overlap.

2.3.1 Definition of the diagnostic

Aiming to quantify this separation, we construct a 2D-curve (using 2 line ratios) or a 3D-surface (using 3 line ratios) that optimally distinguishes SNRs from HII regions.

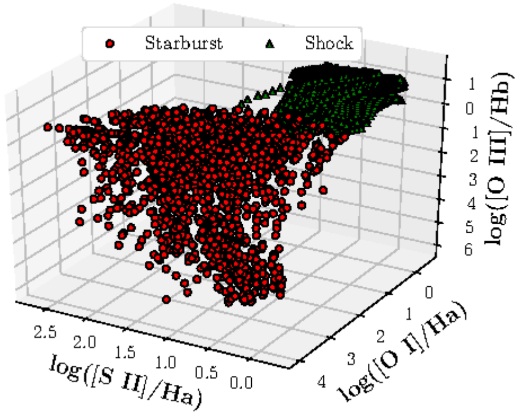

Figure 2.1: A 3D diagram for the [S II]/Hα - [O I]/Hα - [O III]/Hβ line ratios. The points show the expected line ratios for starburst models (red) and shock models (green) for different ISM parameters based on the ITERA library of MAPPINGS III model.

In order to find the most appropriate separating surface, we used the support vector machine (SVM) models. Specifically we used the python module scikit-learn [1], a set of supervised learning algorithms for classification, that separates a set of data in two or more classes. SVM can classify different classes of objects on the basis of separating surfaces in the multi-dimensional space defined by characteristic parameters of these objects (here the line ratios). This boundary can be described by a function of two or more variables, depending on the dimensionality of the input data (here, the number of line ratios which are used). The function of this boundary (decision function) has the following form (e.g. Ivezić et al. 2014):

$$\sum_{i=1}^{n} \alpha_i y_i K(x^T, x_i) + \rho$$

where n is the number of the support vectors, (i.e. the points nearest to the distance of the closest point from either class), y is the class, α is the lagrangian multiplier vector, ρ is the intercept term and $K(x^T, x_i)$ is the kernel function. The general form of the kernel function is $K(x^T, x_i) = (\gamma < x, x_i > +r)^d$, where γ is the kernel width parameter, x_i are the support vectors, r is a constant coefficient, which in our case equals to 1, and d is the degree of the polynomial. We explored various values of γ, from 0.2-1.0, and we selected the ones that better discriminate between different classes, as we explain next. We examined two cases of kernel functions, linear (d=1) and polynomial (d=3), the latter giving more flexibility in the case of complex separating lines/surfaces, for

---

[1] https://scikit-learn.org/stable/modules/svm.html

all combinations of two or three of the line ratios [N II]/Hα, [S II]/Hα, [O I]/Hα, [O II]/Hβ, [O III]/β.

Since we are interested in the definition of a diagnostic tool for SNRs we consider: (a) the completeness of shock models (i.e. SNRs) defined as the number of true positives over the sum of true positives and false negatives (i.e. the total number of shock models) and (b) their contamination by starburst models (i.e. HII regions) that is the number of false positives over the sum of true and false positives. The line ratios that maximize the completeness and minimize the contamination are those that we consider as the best diagnostics for distinguishing SNRs from HII regions. In Figure 2.2 (top) we see the completeness versus the contamination for each line combination and kernel of different functional form (linear or polynomial). The line combinations with the highest completeness and lowest contamination (i.e. the bottom right region of Figure 2.2) are shown in the bottom panel of Figure 2.2.

2.3.2 Optimal diagnostics

From these results it is clear that the polynomial kernel is more efficient than the linear kernel and hence all the diagnostics we present use a polynomial kernel in their decision function. As we see in Figure 2.2 (bottom panel), the most effective line combination is the ([O I]/Hα - [O II]/Hβ - [O III]/Hβ) with $\gamma = 0.8$ (diagnostic A). At the same time, the combination ([S II]/Hα - [O I]/Hα - [O III]/Hβ) with $\gamma = 1.0$ (diagnostic B) works very well and it can be used in cases where the wavelength range of the spectra (or narrow band imaging) is limited to redder wavelengths. We obtain similar results with the line ratios ([N II]/Hα - [O I]/Hα - [O III]/Hβ) with $\gamma = 1.0$ (diagnostic C).

In two dimensions the most effective diagnostic is the combination of line ratios ([O I]/Hα - [O III]/Hβ) with $\gamma = 0.4$ (diagnostic D). If we are restricted in the red and the blue parts of the spectrum, the most powerful diagnostics are ([N II]/Hα - [O I]/Hα) with $\gamma = 1.0$ (diagnostic E) and ([O II]/Hβ - [O III]/Hβ) with $\gamma = 0.2$ (diagnostic F) respectively.

Table 2.1 shows the completeness (CP) and the contamination (CT) for each one of these diagnostics. CPs and CTs show that in general 3D give more accurate results that 2D diagnostics. The rest of the diagnostics we examined are presented in the Appendix.

Figure 2.3 shows the separation surfaces for the cases of the ([O I]/Hα - [O II]/β - [O III]/Hβ; Diagnostic A), ([S II]/Hα - [O I]/Hα - [O III]/Hβ; Diagnostic B) and ([N II]/Hα - [O I]/Hα - [O III]/Hβ; Diagnostic C) diagnostics. The general form of these

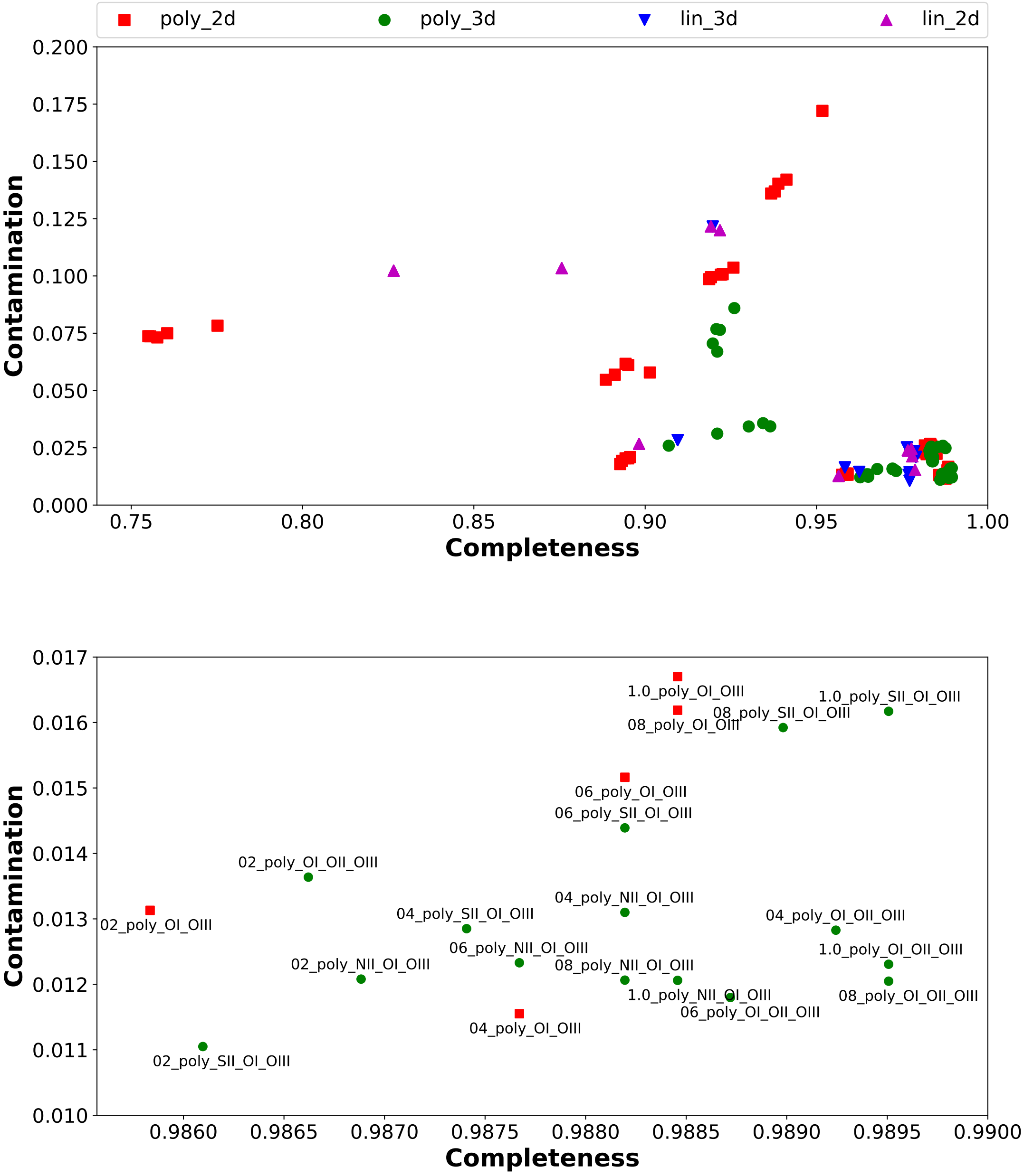

Figure 2.2: Completeness versus contamination for each diagnostic. Different colors and shapes correspond to different kernel of the decision function: the red squares refer to 2D diagnostics with polynomial kernel in the decision function (poly_2d), the green circles to 3D diagnostics with polynomial kernel (poly_3d), the blue triangles-down to 3D diagnostics with linear kernel (lin_3d) and the purple triangles-up to 2D diagnostics with linear kernel (lin_2d). The bottom panel shows more clearly the high completeness - low contamination region of the top panel. Each point is labeled as γ_kernel_lines, where γ is the kernel width parameter (e.g $\gamma = 0.2$ corresponds to 02 kernel), poly refers to polynomial kernel of the decision function and then follow the emission lines ratio used in each diagnostic indicated by the forbidden line involved, e.g. with SII we refer to [S II]/Hα etc.

Table 2.1: Completeness and contamination for the diagnostics described in §3.2.

Diagnostics:	A	B	C	D	E	F
Compl.	0.990	0.990	0.989	0.988	0.983	0.901
Cont.	0.012	0.016	0.012	0.012	0.023	0.058

A: [O I]/Hα - [O II]/Hβ - [O III]/Hβ
B: [S II]/Hα - [O I]/Hα - [O III]/Hβ
C: [N II]/Hα - [O I]/Hα - [O III]/Hβ
D: [O I]/Hα - [O III]/Hβ
E: [N II]/Hα - [O I]/Hα
F: [O II]/Hβ - [O III]/Hβ

surfaces is:

$$F(x, y, z) = \sum_{i=0}^{3} a_{ijk} x^i y^j z^k = 0$$

and the coefficients for each diagnostic are shown in Table 2.2. According to these criteria, sources with F(a, b, c) > 0, where a, b and c are the line ratios of the examined source, are shock-excited regions (SNRs). In Figure 2.4 we present the optimal 2D diagnostic tools for the line ratios ([O I]/Hα - [O III]/Hβ; Diagnostic D), ([N II]/Hα - [O I]/Hβ; Diagnostic E) and ([O II]/Hα - [O III]/Hβ; Diagnostic F). These lines are described by the function:

$$G(x, y) = \sum_{i=0}^{3} b_{ij} x^i y^j = 0$$

and the respective coefficients are shown in Table 2.3. Similarly to the 3D case, sources with G(a, b) > 0, where a and b are the line ratios of the examined source, are considered to be shock-excited regions (SNRs).

Table 2.2: Coefficients of the decision function (3rd-order polynomial kernel) for the 3D diagnostics.

ijk	A	B	C
000	3.070	0.303	0.567
010	-2.228	-1.357	-0.862
020	-0.554	0.815	0.386
030	0.452	0.696	0.590
001	0.824	1.197	1.400
011	2.248	-1.854	-2.307
021	0.185	1.356	0.477
002	-1.476	-1.495	-1.213
012	-0.771	2.312	1.837
003	0.964	1.874	1.842
100	-0.871	-1.227	-1.752
110	0.932	0.285	2.433
120	-1.075	1.766	1.281
101	-0.174	1.687	-0.428
111	-2.650	-3.664	-3.680
102	1.842	-1.329	2.230
200	-0.166	0.873	0.027
210	1.134	-0.896	1.873
201	-0.419	0.403	0.195
300	0.768	-0.598	-1.082

A: [O I]/Hα - [O II]/Hβ - [O III]/Hβ
B: [S II]/Hα - [O I]/Hα - [O III]/Hβ
C: [N II]/Hα - [O I]/Hα - [O III]/Hβ

Table 2.3: Coefficients of the decision function (3rd-order polynomial kernel) for the 2D diagnostics.

ij	D	E	F
00	2.710	1.285	-2.904
01	2.096	0.382	3.356
02	-1.610	1.263	1.344
03	0.049	1.162	0.347
10	-0.701	-0.0007	4.591
11	-0.887	4.330	-1.133
12	1.067	0.067	-0.616
20	-0.432	-0.874	1.952
21	-0.245	4.249	0.416
30	0.465	-2.159	-0.008

D: [O I]/Hα - [O III]/Hβ
E: [N II]/Hα - [O I]/Hα
F: [O II]/Hβ - [O III]/Hβ

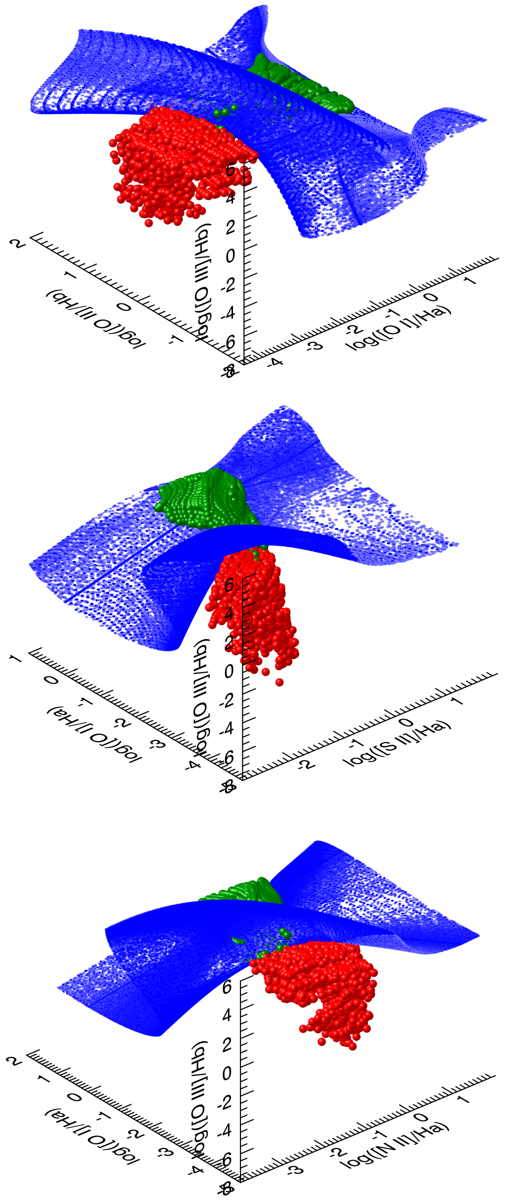

Figure 2.3: The surfaces separating shock models (SNRs, green) from starburst models (HII regions, red) for the diagnostics A ([O I]/Hα - [O II]/Hβ - [O III]/Hβ), B ([S II]/Hα - [O I]/Hα - [O III]/Hβ) and C ([N II]/Hα - [O I]/Hα - [O III]/Hβ), from top to bottom respectively. The data points are drawn from the ITERA compilation of MAPPINGS III models for representative densities and metallicities (§2).

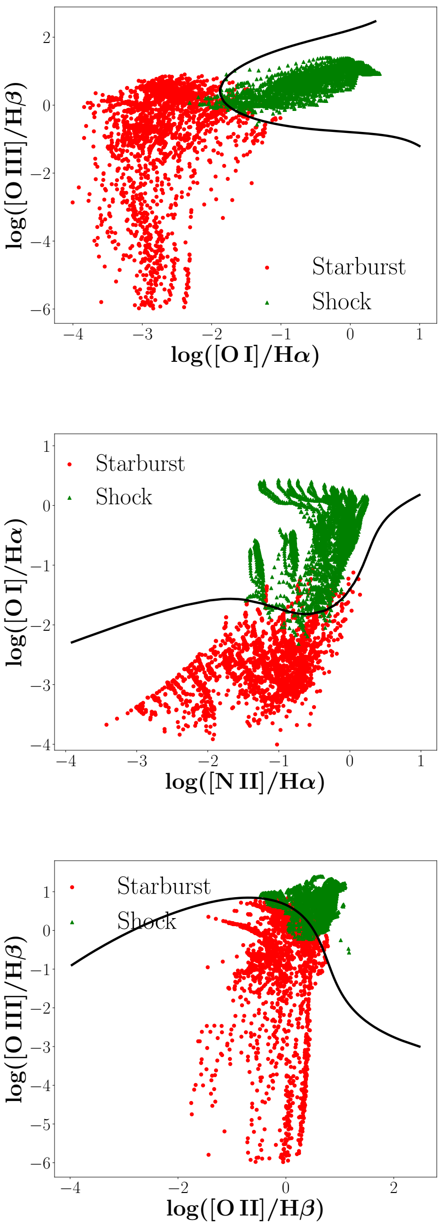

Figure 2.4: The lines that separate shock models (SNRs, green) from starburst models (HII regions, red) for the diagnostics D ([O I]/Hα - [O III]/Hβ), E ([N II]/Hα - [O I]/Hα) and F ([O II]/Hβ - [O III]/Hβ), from top to bottom respectively. The data points are drawn from the ITERA compilation of MAPPINGS III models for representative densities and metallicities (§2).

Table 2.4: Dependence of the completeness (CP) and contamination (CT) for the different diagnostics on the metallicity

Subsolar metallicities - $0.25 - 0.5\,\mathrm{Z}_\odot$ (LMC-SMC metallicities)

Diagnostics:	A	B	C	D	E	F
CP	0.995	0.996	0.987	0.998	0.974	0.835
CT	0.078	0.102	0.081	0.075	0.144	0.317

Solar metallicities

Diagnostics:	A	B	C	D	E	F
CP	0.995	0.994	0.955	0.992	0.991	0.911
CT	0.017	0.023	0.017	0.016	0.032	0.087

Supersolar metallicities - $2\,\mathrm{Z}_\odot$

Diagnostics:	A	B	C	D	E	F
CP	0.922	0.922	0.916	0.919	0.916	0.838
CT	0.155	0.185	0.158	0.139	0.247	0.460

2.4 Discussion

2.4.1 Effect of Metallicity

The diagnostics presented in section 3 are based on photo-ionization and shock models for a wide range of metallicities, from $0.25\,Z_\odot - 2\,Z_\odot$. Since metallicity is directly linked to the strength of the forbidden lines (Leonidaki, Boumis, & Zezas 2013; D'Odorico et al. 1978), we explore the efficiency of the diagnostics described in §3.2 in different metallicity regimes. Hence, we calculate completeness and contamination for the SNRs with subsolar, solar, and supersolar metallicities. These results are shown in Table 2.4. We see that for the cases of subsolar and solar metallicities the diagnostics work quite well while for supersolar metallicities less good. This happens because high-metallicity nebulae have strong temperature gradient (Stasińka 2005; Stasińka 1980; Stasińka 1978b) resulting in a wider range of intensities for the oxygen lines. Actually, for supersolar metallicities the intensities of the oxygen lines extend to lower values, compared to solar or subsolar metallicities, and thus shifting the lower-excitation shock excited sources in the HII region locus.

Table 2.5: Completeness - Contamination for the [S II]/Hα > 0.4 criterion

Metallicities:	Total	Subsolar	Solar	Supersolar
CP	0.658	0.317	0.682	0.764
CT	0.019	0.217	0.026	0.175

2.4.2 Comparison with [S II]/Hα > 0.4 criterion

The standard diagnostic for identifying SNRs is the [S II]/Hα > 0.4 criterion. Here we investigate the efficiency of this diagnostic in the light of the 2D and 3D diagnostics presented in §3.2. Figure 2.5 shows the [S II]/Hα = 0.4 line on the [S II]/Hα - [O I]/Hα diagram (top left panel) along with histograms of starburst and shock models for each of the two line ratios ([S II]/Hα bottom; [O I]/Hα right). In the case of the [S II]/Hα line ratio we also indicate the 0.4 line. As we can see, there is a significant fraction of shock models with [S II]/Hα lower than 0.4 (on the left of the 0.4 line) but also a small number of starburst models that have ratios higher than 0.4. This means that by using the [S II]/Hα > 0.4 criterion as selection criterion, we may miss many shock excited sources or identify as SNRs photoionized sources, like HII regions. In Table 2.5 we give a summary of the completeness and the contamination for the [S II]/Hα > 0.4 criterion for all the metallicities together and for the subsolar, solar and supersolar metallicities separately. The effect is more dramatic in the case of subsolar metallicities where we may miss even up to ∼70% of the SNR population. In higher metallicities the effect is weaker but it still may result up to 25% incompleteness and ∼15-20% contamination by HII-regions.

Therefore, the full 2D and 3D diagnostics, give us the possibility to detect up to ∼30% more SNRs than we did up to now.

Most importantly the application of the [S II]/Hα > 0.4 criterion, leads to a selection effect against slow-shock objects. Figure 2.6 shows a cumulative histogram of the shock velocities of all shock models (i.e any [S II]/Hα ratio) and those with [S II]/Hα < 0.4. As we can see, SNRs with lower velocities have predominantly [S II]/Hα < 0.4. This selection effect in turn results in a bias against older SNRs which have weaker shocks. In addition, there are SNRs with high velocities that are not detected with the 0.4 criterion. These SNRs are characterized by lower values of magnetic parameters (usually high preshock densities $100 - 1000\,\mathrm{cm}^{-3}$ or more rarely low magnetic field $\sim 1\mu\,\mathrm{G}$). In these cases, the density close to the photoionized zone of the shock becomes high and hence the spontaneous de-excitation of forbidden lines becomes less important (Allen et al. 2008), leading to a relatively lower [S II]/Hα ratio.

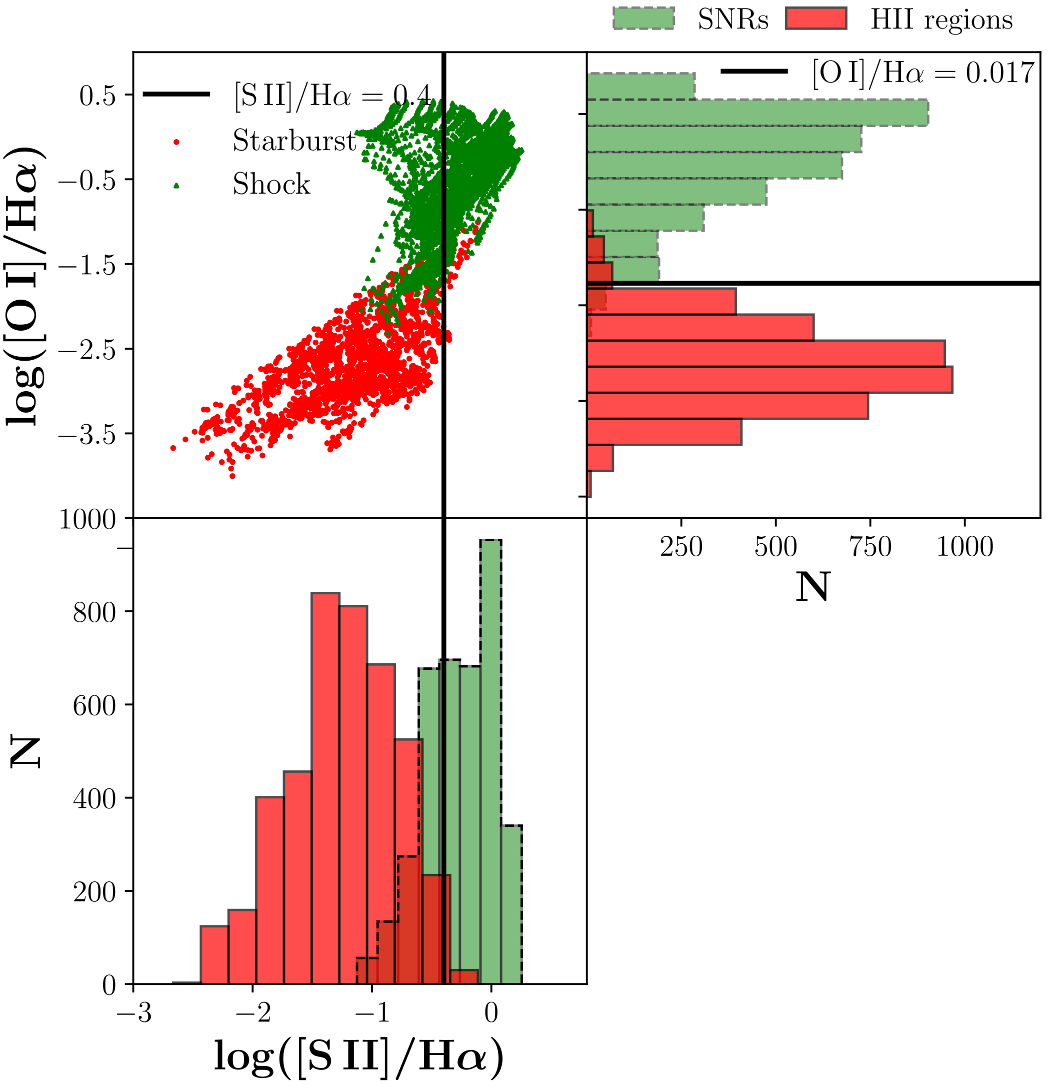

Figure 2.5: Behaviour of the [S II]/Hα and [O I]/Hα diagnostics in separating SNRs (green) from HII regions (red). Top left: 2D [S II]/Hα - [O I]/Hα diagnostic. The black line indicates the standard [S II]/Hα > 0.4 diagnostic. Top right panel: the histogram of the [O I]/Hα ratio for SNRs and HII regions along with the 0.017 line (see §4.4). This line ratio minimizes the overlap between SNRs and HII regions. Bottom left: histogram of the [S II]/Hα ratio for SNRs and HII-regions along with the 0.4 line. We see that there are many SNRs with [S II]/Hα < 0.4 that are not identified as such, and a few HII regions that have [S II]/Hα > 0.4 and thus are identified as SNRs using the [S II]/Hα > 0.4 criterion. In both histograms, N is the number of the points of the shock and starburst models.

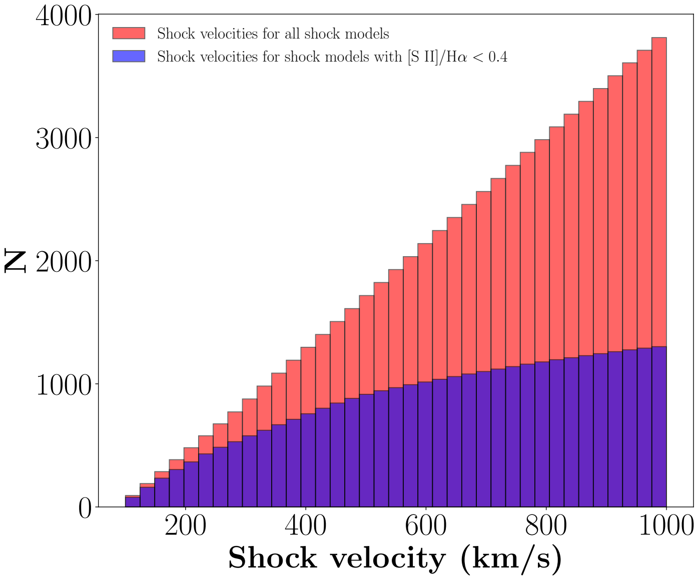

Figure 2.6: Shock velocity cumulative distribution for shock models of every [S II]/H$\alpha < 0.4$ ratio (red color) and for shock models with [S II]/H$\alpha < 0.4$ (blue color). N is the number of the points of the shock and starburst models.

In order to find a 1D diagnostic with which we can recover these slow-shock regions, we constructed histograms for photoionized and shock-excited regions for each line ratio we considered. The line ratio that minimizes the overlap between the two populations is the [O I]/Hα with 171 (out of 8080) overlapping models (Figure 2.5 top right panel) and recovers the vast majority of the SNRs that were Missed by the [S II]/Hα criterion ($\simeq$ 97% of the total number of the points of the shock models), while keeping the contamination by photoionized regions at a minimum. Of course, the 2D and 3D diagnostics have even higher completeness and lower contamination (c.f. Table 2.1).

2.4.3 Comparison with data

In order to test the accuracy of the diagnostic tools, we compare our models with observational data. We have divided our data sample into two categories. A sample which refers to Galactic SNRs and SNRs of nearby galaxies (LMC, SMC), the SNR nature of which is confirmed by their morphology and/or their radio properties and consequently we can consider it as a more secure sample. We also consider a second sample which consists of SNRs in more distant galaxies that are identified on the basis of the [S II]/Hα criterion. In the same way we use Galactic HII regions and HII regions from the LMC and SMC as a more secure sample and extragalactic HII regions in more distant galaxies as less secure. Table 2.6 lists individual Galactic sources and the host galaxies for the extragalactic sources, as well as the relevant publications. From these studies, we use objects for which [N II]($\lambda6583$), [S II]($\lambda\lambda6716, 6731$), [O I]($\lambda6300$), [O II]($\lambda\lambda3727, 3729$), [O III]($\lambda5008$), Hα and Hβ line fluxes are provided.

We begin with the more secure sample of SNRs which consists of 15 objects. For the diagnostics B ([S II]/Hα - [O I]/Hα - [O III]/Hβ) and C ([N II]/Hα - [O I]/Hα - [O III]/Hβ) all sources except for two fall in the region of SNRs (given their line ratio uncertainties). In the case of diagnostic D ([O I]/Hα - [O III]/Hβ) only one source does not agree (Figure 2.7) while we have full agreement in the case of diagnostic E ([N II]/Hα - [O III]/Hβ) (Figure 2.8). We note that the two sources that do not agree with the diagnostics are the same for all the diagnostics and have large uncertainties in the [O I]/Hα and [O III]/Hβ ratios.

We find between 88.5% and 99.2% agreement between the diagnostics and the prior classification of the less secure sample of SNRs. The best agreement is for diagnostic E, while the worse agreement is for diagnostic F. Figs 9, 10, 11 show these data for the diagnostics D, E and F respectively. Most of the sources that are not found in the expected loci in the diagrams, seem to have very low signal to noise in the [O I] and [O III] lines indicating large uncertainties for [O I]/Hα and [O III]/Hβ line ratios (Leonidaki, Boumis, & Zezas 2013; Matonick & Fesen 1997).

The more secure sample of HII regions consists of 18 sources. For the diagnostics B and C two out of the 18 sources are found outside of the HII-region locus. One and 2 additional sources are marginally consistent with their respective loci in diagnostics D and E, taking into account the uncertainties when they are available (Figure 2.7, Figure 2.8).

For the less secure sample of HII regions we have 100% agreement for diagnostics A and F (7 out of 7 sources). For the rest of diagnostics (B, C, D and E) $\sim$ 13% for the sources fall out of the HII-region locus.

Table 2.6: Samples of observational data for SNRs and HII regions

SNRs	
Fesen, Blair, & Kirshner 1985	Galaxy: S147_1*, S147_2*, S147_3*, S147_4*, S147_5*, ML1†, ML2†, G65.3+5.7_1, G65.3+5.7_2
Russel & Dopita 1990	SMC, LMC
Matonick & Fesen 1997	NGC 5204, NGC 5585, NGC 6946 M81, M101
Leonidaki, Boumis, & Zezas 2013	NGC 2403, NGC 3077, NGC 4214 NGC 4395, NGC 4449, NGC 5204
Lee et al. 2015	M81, M82
Long, Winkler, & Blair 2019	NGC 6946
HII regions	
Zurita & Bresolin 2012	M31
Esteban et al. 2009	M31, M33
Kwitter & Aller 1980	M33
Dufour 1975	LMC
Russel & Dopita 1990	LMC, SMC
Tsamis et al. 2003	LMC, SMC
Vílchez & Esteban 1996	Galaxy: S283, S266A, S266B
Bresolin 2007	M101
Castellanos, Díaz, & Terlevich 2002	NGC 628, NGC 925, NGC 1637, NGC 1232
Fich & Silkey 1991	Galaxy: S128, S212
Berg et al. 2015	NGC 628

*These are the positions 1-5 for the SNR S147. †These are the positions 1 and 2 of Monocerus Loop.

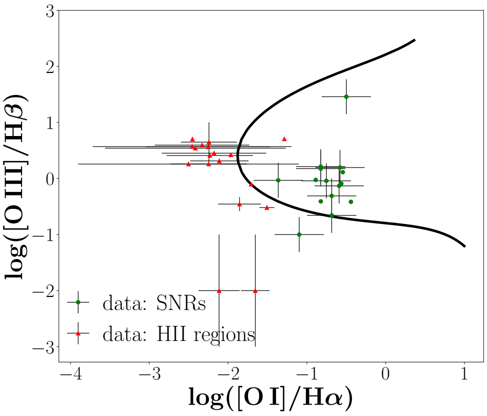

Figure 2.7: Diagnostic D ([O I]/Hα - [O III]/Hβ) for the more secure sample. As we see only 1 out of 15 SNRs is not located in the locus of SNRs and it has large uncertainties in the [O I]/Hα and [O III]/Hβ line ratios. For the HII regions only 1 out of the 18 sources is not found in the HII-region locus. This source, as well as the other sources without errorbars did not have available uncertainties in the respective publications.

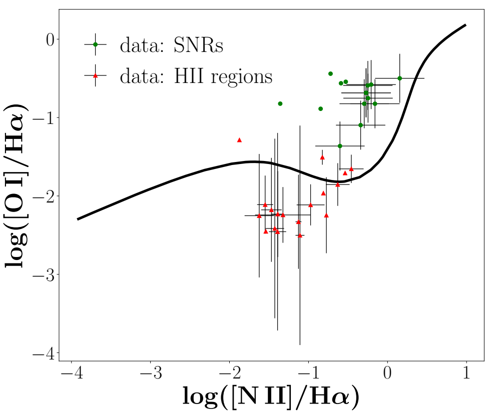

Figure 2.8: Diagnostic E ([N II]/Hα - [O I]/Hα) for the more secure sample. As we see all the SNRs are located in the locus defined by the shock regions. For the HII-regions 15 out of 18 are found in the photoionized-regions locus. The errorbars are presented when the line-intensity uncertainties are available in the respective works.

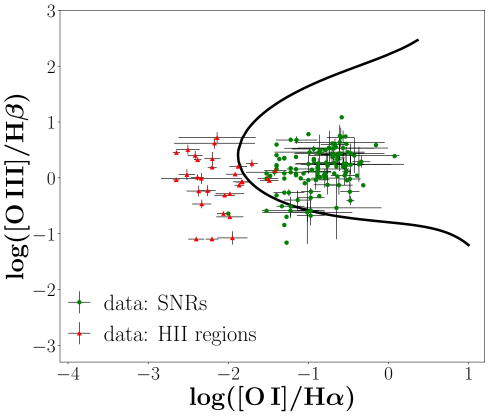

Figure 2.9: Diagnostic D ([O I]/Hα - [O III]/Hβ) for the less secure sample. As we see 6 out of 127 SNRs are not located in the locus defined by the shock regions. These sources have low signal to noise ratio in the [O I] and [O III] lines indicating large uncertainties in the respective line ratio. The errorbars are presented when the line-intensity uncertainties are available in the respective works.

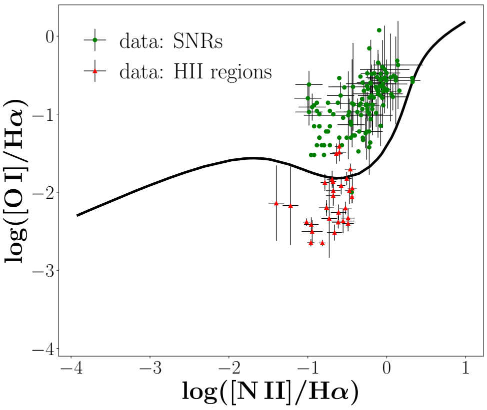

Figure 2.10: Diagnostic E ([N II]/Hα - [O I]/Hα) for the less secure sample. As we see only 1 out of 127 SNRs is not located in the locus defined by the shock regions. This source has low signal to noise ratio in the [O I] line indicating large uncertainties in the respective line ratio. The errorbars are presented when the line-intensity uncertainties are available in the respective works.

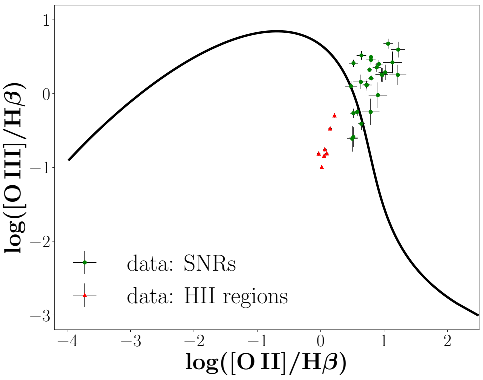

Figure 2.11: Diagnostic F ([O II]/Hβ - [O III]/Hβ) for the less secure sample. In this case 23 out of 26 SNRs fall in the SNR locus, while all the HII regions are located in the HII-region locus.

In summary, we find very good agreement between the diagnostics and the morphologically selected SNRs (Figure 2.7, Figure 2.8). In addition, even though we do not expect 100% agreement between our diagnostics and the less secure sample, since they have been selected based on the [S II]/Hα > 0.4 criterion, we find that they agree very well.

The same holds in the case of HII regions. Observed HII regions are clearly separated from the SNRs resulting in minimal or no contamination of the SNR population by HII regions.

Furthermore, when emission-line uncertainties are available, we can account for those and derive the probability of a source to belong to shock-excited or photoionized region locus (indicating SNR and HII regions respectively; e.g. by means of Monte Carlo sampling, e.g. Maragkoudakis et al. 2018).

One complication in the identification of SNRs on the basis of their line ratios is objects that are embedded in HII regions. In this case, the generally weaker higher excitation linesof the HII region would shift the location of the SNRs away from their locus on the diagnostic diagram. Determining a diagnostic that accounts for the contamination by the surrounding HII regions, is beyond the scope of this paper and will be presented in a forthcoming paper.

As we can see, in some cases there are contradicting classifications. Sources that have been classified as SNRs according to a specific diagnostic, are classified as HII regions using other diagnostic. For example, While almost all of the observed SNRs are classified as shock-excited regions using diagnostic E (Figs 8, 10) a few of them are classified as photoionized (HII) regions based on diagnostic D (Figs 7, 9). This is expected since these diagnostics are simply projections of the multidimensional manifold of the distribution of the shock-excited (SNR) and photoionized (HII regions) in the parameter space defined by the spectral line ratios (e.g. Stampoulis et al. 2019). Obviously higher dimensionality diagnostics (e.g. diagnostics A, B, and C) offer much better consistency since *all* available lines are used simultaneously. However, this comes at the cost of requiring measurements of multiple lines, some of which are rather weak.

2.4.4 Possible biases and comparison with other object classes

The diagnostics presented here are based on the comparison of the ratio between different forbidden lines and their corresponding (closest) Balmer lines. They are an extension of the commonly used [S II]/Hα diagnostic to include other diagnostically powerful line ratios combined with a quantitative definition of the diagnostic. Since they also employ forbidden lines they suffer from the same bias against Balmer dominated SNR inherent in the traditional [S II]/Hα diagnostic. This class of SNRs is characterized by weak or absent, forbidden lines and they are traditionally recognized on the basis of their strong and broad Balmer lines (e.g. Heng 2010). However, this is not a strong bias for studies of the overall population of SNRs, since Balmer dominated SNRs are only a small subset of the optically emitting SNR population.

Other types of objects that also produce high excitation lines are planetary nebulae and Herbig-Haro objects. However planetary nebulae are characterized by strong [O III] emission and weak [S II], [O I] or [N II] emission which would discriminate them from the locus of SNRs in our diagnostic diagrams and place them in the high-excitation end of the HII-region locus (e.g. Baldwin et al. 1981, Sabbadin et al. 1977).

On the other hand although Herbig-Haro objects are excited by the shock of the jets of young stellar objects, their total luminosity ($\sim 0.1 L_\odot$; e.g. Riaz et al. 2017) renders them unobservable in SNR surveys of nearby galaxies. In our Galaxy they can be easily discriminated from SNRs on the basis of their morphology.

2.4.5 Suggested tool for photometric selection of SNRs

The results presented in section §3.2 show that the ideal diagnostic combines the [O I], [O III], [O II], or [S II] forbidden lines along with their corresponding Balmer lines (Hα and Hβ). However this requires observations in five narrow-band filters which greatly increases the required telescope time.

In Figure 2.5, we compare the distributions of the [S II]/Hα and [O I]/Hα line ratios for the SNRs and HII regions. As is clearly seen, the [O I]/Hα line ratio separates more effectively the HII regions from SNRs (see also Lee et al. 2015, Fesen, Blair, & Kirshner 1985). This is because the [O I] line is produced in the interface between the photoionized HII region and the surrounding material. In HII region, this interface tends to be quite narrow, since almost all the oxygen is ionized (Evans & Dopita 1985), resulting in weaker [O I] emission. On the other hand, in SNRs because of the different excitation mechanism and the presence of the photoionizing precursor, the size of this region is wider resulting in stronger [O I] emission. Consequently, Hα and [O I](6300) narrow-band filters can be used for SNR selection. In this case SNR candidates are sources with [O I]/Hα ratio higher than 0.017 (or $\log([\mathrm{O\ I}]/\mathrm{H}\alpha) > -1.76$) (Figure 2.5 top right). The completeness for SNR selection using this diagnostic is 97.2% and the contamination only 2.4%.

Table 2.7: Completeness, contamination and γ parameter for 3D and 2D diagnostics

Diagnostics	Completeness	Contamination	γ
[N II]/Hα – [O I]/Hα – [O II]/Hβ	0.984	0.019	1.0
[N II]/Hα – [O II]/Hβ – [O III]/Hβ	0.937	0.034	1.0
[N II]/Hα – [S II]/Hα – [O I]/Hα	0.984	0.024	0.2
[N II]/Hα – [S II]/Hα – [O II]/Hβ	0.926	0.086	0.2
[N II]/Hα – [S II]/Hα – [O III]/Hβ	0.973	0.015	1.0
[S II]/Hα – [O I]/Hα – [O II]/Hβ	0.988	0.025	1.0
[S II]/Hα – [O II]/Hβ – [O III]/Hβ	0.965	0.012	1.0
[N II]/Hα – [O II]/Hβ	0.827	0.102	all (0.2 - 1.0)
[N II]/Hα – [O III]/Hβ	0.898	0.027	all (0.2 - 1.0)
[O I]/Hα – [O II]/Hβ	0.985	0.022	1.0
[S II]/Hα – [O I]/Hα	0.983	0.026	1.0
[S II]/Hα – [O III]/Hβ	0.959	0.013	0.4
[S II]/Hα – [O II]/Hβ	0.941	0.142	0.4
[S II]/Hα – [N II]/Hα	0.926	0.104	0.2

2.5 Other Diagnostics

Here we present the rest of the diagnostics we examined and are not included in §3. In Table 2.7 we show the completeness, the contamination and the γ perameters of the decision function of the 3D and 2D diagnostics. Figures 2.12 - 2.25 show the separating surfaces and lines for these 3D (2.12-2.18) and 2D (2.19-2.25) diagnostics. Animations that show the rotation of the surfaces are available in the on-line version. As discussed in §3.2 the surfaces are described by the function $F(x, y, z) = \sum_{i=0}^{3} a_{ijk} x^i y^j z^k = 0$ and the 2D lines by $G(x, y) = \sum_{i=0}^{3} b_{ij} x^i y^j = 0$. The coefficients of these functions are given in Table 2.8 and Table 2.9 respectively. For both cases, sources with F $>$ 0 or G $>$ 0 are SNRs.

In all cases, polynomial kernels seem to work better, except for the line-ratio combinations [N II]/Hα – [O II]/Hβ and [N II]/Hα – [O III]/Hβ for which linear kernel gives better results.

Table 2.8: Coefficients of the decision function for the 3D diagnostics.

ijk	NII-OI-OII	NII-OII-OIII	NII-SII-OI	NII-SII-OII	NII-SII-OIII	SII-OI-OII	SII-OII-OIII
000	3.734	3.478	2.382	1.520	2.413	4.108	4.974
010	1.578	-1.199	-1.822	2.202	1.267	1.213	-3.676
020	-2.053	2.729	0.151	-0.038	0.770	-1.274	1.467
030	0.326	0.576	-0.002	-0.055	-1.585	0.826	2.269
001	-1.437	5.176	0.214	1.626	4.377	-1.758	4.722
011	1.608	-1.968	0.658	-1.050	-2.697	2.587	1.088
021	4.849	1.264	-0.021	0.098	1.823	5.000	1.078
002	-0.768	-2.798	-0.804	0.283	-2.732	-0.747	-3.318
012	-0.459	-2.641	0.014	0.141	-1.325	-0.094	-0.354
003	0.139	3.011	0.223	0.361	1.463	0.266	2.156
100	-3.186	7.034	-1.821	-0.610	0.001	-2.305	3.761
110	6.108	3.313	-0.795	-2.699	-6.913	2.439	2.946
120	0.609	-0.372	0.127	0.283	1.753	-0.096	-1.869
101	3.889	0.788	0.149	2.639	1.508	1.342	-0.421
111	-2.792	-0.877	0.379	-0.460	-2.264	-2.236	1.194
102	4.071	-3.772	0.196	0.067	-0.866	0.762	-0.304
200	0.863	-1.549	-0.350	1.460	0.407	-0.172	-3.181
210	3.986	8.080	0.250	0.231	1.568	0.359	0.713
201	-0.268	-0.879	0.253	-0.388	-0.638	-1.707	-0.501
300	-1.085	-1.704	0.025	-0.140	-2.913	0.042	-0.151

The line-ratio combinations are presented without the respective Hydrogen lines. In every case:
SII = [S II]/Hα, NII = [N II]/Hα, OI = [O I]/Hα, OII = [O II]/Hβ and OIII = [O III]/Hβ .

Table 2.9: Coefficients of the decision function for the 2D diagnostics.

ij	NII-OII	NII-OIII	OI-OII	SII-OI	SII-OIII	SII-OII	SII-NII
00	0.581	0.469	5.017	1.218	3.403	2.777	2.763
01	1.000	1.000	-2.274	0.145	4.433	-0.283	1.116
02	0	0	-1.170	1.371	-0.479	0.981	1.388
03	0	0	0.432	1.446	0.255	1.185	-0.217
10	1.262	0.939	0.719	-0.449	4.660	4.283	2.244
11	0	0	3.095	1.932	-0.781	-0.332	-2.452
12	0	0	0.124	-1.036	-0.318	-0.225	0.029
20	0	0	-0.842	-0.089	-1.821	-0.575	-0.257
21	0	0	4.291	2.197	0.148	-0.511	0.175
30	0	0	0.701	0.461	0.079	-0.403	-0.043

The line-ratio combinations are presented without the respective Hydrogen lines. In every case:
SII = [S II]/Hα, NII = [N II]/Hα, OI = [O I]/Hα, OII = [O II]/Hβ and OIII = [O III]/Hβ .

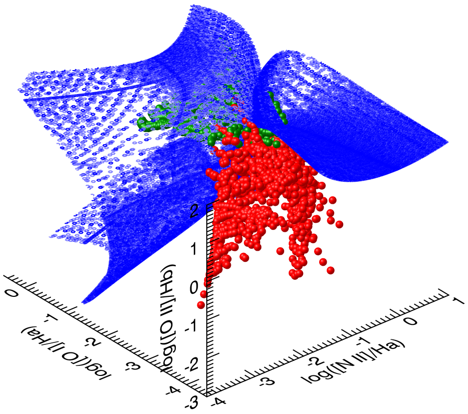

Figure 2.12: The surface separating shock models (SNRs, green) from starburst models (HII regions, red) for the diagnostic [N II]/Hα – [O I]/Hα – [O II]/Hβ.

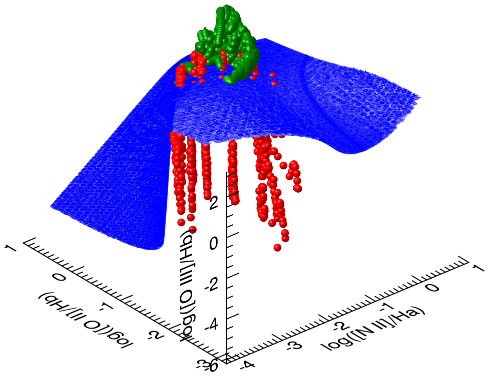

Figure 2.13: The surface separating shock models (SNRs, green) from starburst models (HII regions, red) for the diagnostic [N II]/Hα – [O II]/Hβ – [O III]/Hβ.

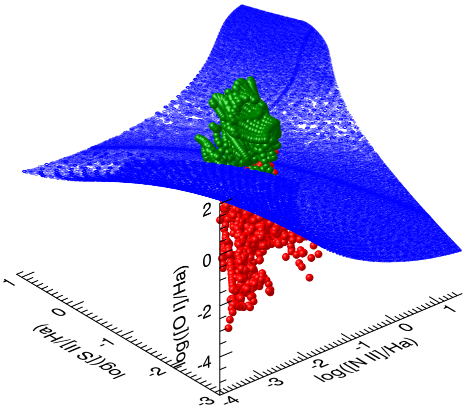

Figure 2.14: The surface separating shock models (SNRs, green) from starburst models (HII regions, red) for the diagnostic [N II]/Hα – [S II]/Hα – [O I]/Hα.

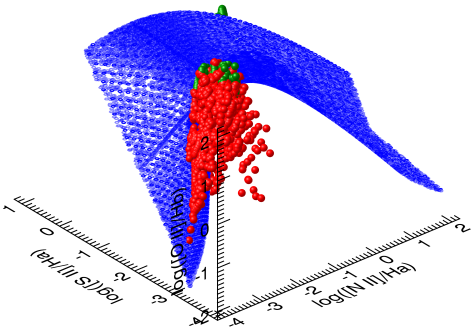

Figure 2.15: The surface separating shock models (SNRs, green) from starburst models (HII regions, red) for the diagnostic[N II]/Hα – [S II]/Hα – [O II]/Hβ.

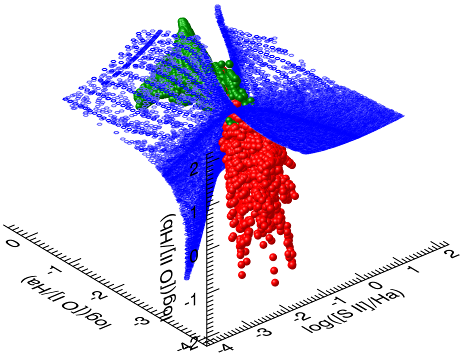

Figure 2.16: The surface separating shock models (SNRs, green) from starburst models (HII regions, red) for the diagnostic [S II]/Hα – [O I]/Hα – [O II]/Hβ.

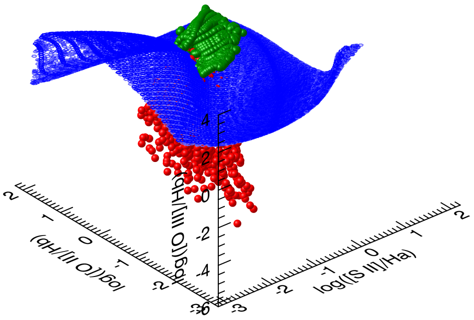

Figure 2.17: The surface separating shock models (SNRs, green) from starburst models (HII regions, red) for the diagnostic [S II]/Hα – [O II]/Hβ – [O III]/Hβ.

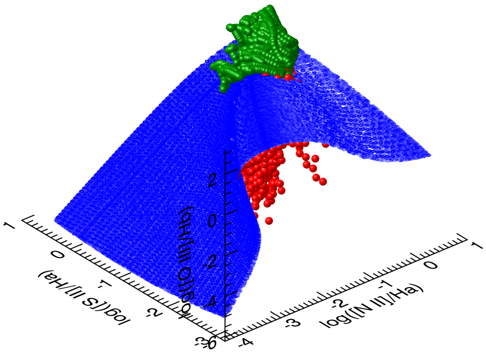

Figure 2.18: The surface separating shock models (SNRs, green) from starburst models (HII regions, red) for the diagnostic [N II]/Hα – [S II]/Hα – [O III]/Hβ.

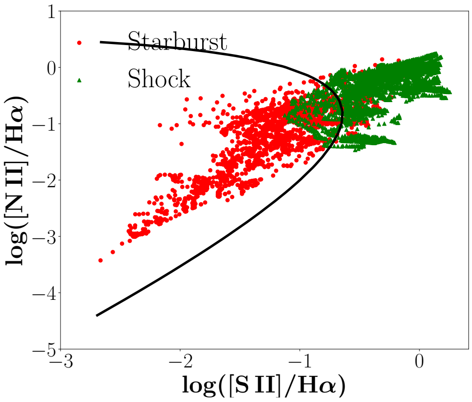

Figure 2.19: The line that separates shock models (SNRs, green) from starburst models (HII regions, red) for the diagnostic [S II]/Hα – [N II]/Hα.

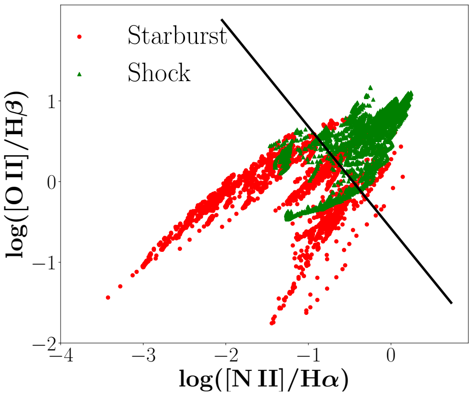

Figure 2.20: The line that separates shock models (SNRs, green) from starburst models (HII regions, red) for the diagnostic [N II]/Hα – [O II]/Hβ.

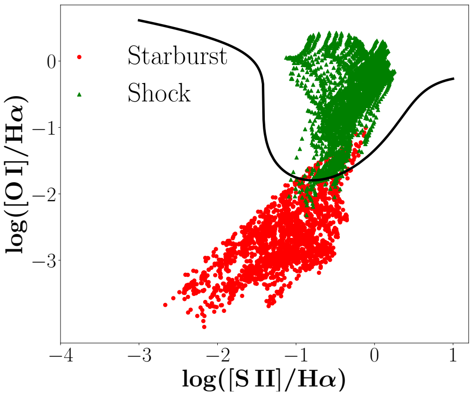

Figure 2.21: The line that separates shock models (SNRs, green) from starburst models (HII regions, red) for the diagnostic [S II]/Hα – [O I]/Hα.

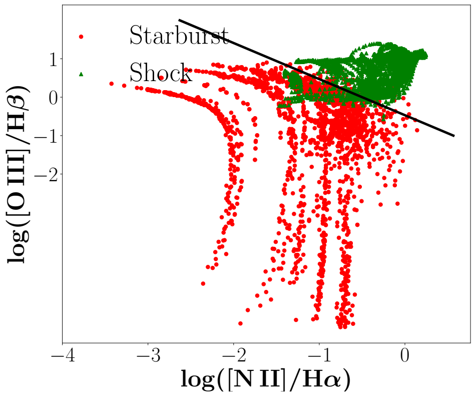

Figure 2.22: The line that separates shock models (SNRs, green) from starburst models (HII regions, red) for the diagnostic [N II]/Hα – [O III]/Hβ.

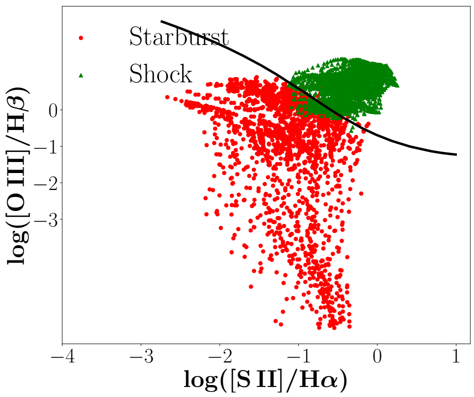

Figure 2.23: The line that separates shock models (SNRs, green) from starburst models (HII regions, red) for the diagnostic [S II]/Hα – [O III]/Hβ.

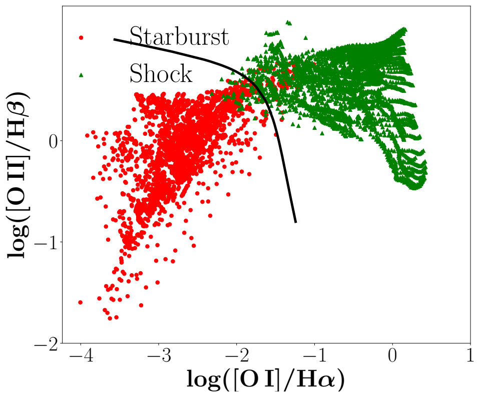

Figure 2.24: The line that separates shock models (SNRs, green) from starburst models (HII regions, red) for the diagnostic [O I]/Hα – [O II]/Hβ.

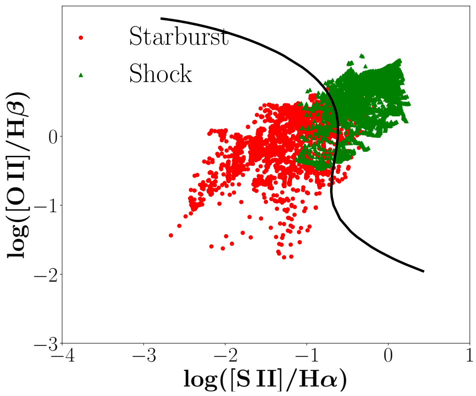

Figure 2.25: The line that separates shock models (SNRs, green) from starburst models (HII regions, red) for the diagnostic [S II]/Hα – [O II]/Hβ.

2.6 Conclusions

In this paper we presented theory-driven line-ratio diagnostics for the identification of SNRs. These diagnostics are very promising in reducing the bias against lower excitation SNRs in comparison to the traditional [S II]/Hα diagnostic and they can increase the number of identified SNRs by $\sim 30\%$ at least. We explore six line-ratios combined in 3D or 2D diagnostics involving [O I], [O II], [O III], [S II] and [N II] lines and their corresponding Hα and Hβ lines. We find that the best 3D and 2D diagnostics in terms of their completeness and low contamination by HII regions are [O I]/Hα - [O II]/Hβ - [O III]/Hβ and [O I]/Hα -[O III]/Hβ respectively. We also find that the [O I]/Hα diagnostic is very efficient for selecting SNRs, in agreement with previous reports. Here we define the selection criterion ([O I]/Hα > 0.017) and we quantify its completeness (97.2%) and contamination (2.4%). This efficiency is significantly higher than the one of 65.8% for the [S II]/Hα > 0.4 diagnostic that has been used up to now.

This work has been based on MAPPINGS III shock and starburst models. The use of other shock and starburst models would give probably different diagnostics (different separating lines and surfaces), however, the capabilities of the different line-ratio combinations in distinguishing SNRs from HII regions should be the same or at least very similar.

Acknowledgements

We thank the anonymous referee for the helpful comments that helped to improve the clarity of the paper. We acknowledge funding from the European Research Council under the European Union's Seventh Framework Programme (FP/2007-2013)/ERC Grant Agreement n. 617001. This project has received funding from the European Union's Horizon 2020 research and innovation programme under the Marie Sklodowska-Curie RISE action, grant agreement No 691164 (ASTROSTAT). We also thank Jeff Andrews for organizing the SMAC (Statistical methods for Astrophysics in Crete) seminar and for helpful discussions about SVM, and Paul Sell for his important help on the construction of 3D animations.

3

The Supernova Remnant Populations of the galaxies NGC 45, NGC 55, NGC 1313, NGC 7793: Luminosity and Excitation Functions

3.1 Introduction

Supernova Remnants (SNRs) are an integral component of the interstellar medium (ISM), since they provide large amounts of mechanical energy, while they enrich it with heavy elements. They are related to the star-forming process within a galaxy, since under appropriate conditions, their shock waves compress the ISM, triggering new-star formation. In addition, core-collapse SNRs, are tracers of the on-going massive star formation since they are the last stage in the life of massive stars ($M > 8\,M_\odot$; Condon & Yin 1990).

In our Galaxy, 294 SNRs have been identified so far, based on the systematic study in radio bands (Green 2019). Many of them have been studied in various wavelengths (e.g. Milisavljevic & Fesen 2013; Boumis et al. 2009; Slane et al. 2002) yielding detailed information on their physical and morphological properties, as well as, their interaction with their local ISM. Studying SNRs in different wavelengths gives us the opportunity to examine different gas phases of SNRs, from million to thousands degree gas and different evolution stages. However, the study of Galactic SNRs has some disadvantages: optical and X-ray bands are suffering from significant extinction, leading sometimes to incomplete samples. In addition, the study of Galactic SNRs does not allow us to examine SNR populations that evolve in a wide range of ISM parameters (e.g. different density distributions, metallicities). Another important limitation of studies in Galactic SNRs is that it is very difficult to estimate their distances. The study of extragalactic SNRs remedies these limitations. They give us the opportunity to explore larger and more diverse samples that can be correlated to different ISM and galaxy properties. In addition, extragalactic sources overcome the problems of Galactic absorption and distance uncertainties, since they are considered to be at the distance of their host galaxy. Taking advantage of these benefits, many studies of SNRs in nearby galaxies have been carried out (e.g. Long, Winkler, & Blair 2019; Lee et al. 2015; Leonidaki, Boumis, & Zezas 2013; Leonidaki, Zezas, & Boumis 2010; Blair & Long 1997). These studies increase the number of known SNRs and thus provide significant information on their nature not only on individual objects, but also on their overall population and their effect on their host galaxy.

A significant limitation of these surveys is that they do not account for the effect of incompleteness. During the detection process, there is a fraction of SNRs that we do not detect because of their faintness, the detection process, and the method we have followed for the selection and identification of SNRs. These effects make our samples incomplete. Incompleteness is a fundamental problem that can affect significantly our results. For example, we can see features in luminosity functions which are not real and they are simply artefacts of the detection and selection process. This problem is exacerbate by the commonly used practice of SNR identification based on visual inspection of Hα, [S II], and [S II]/Hα maps. Visual inspection, being a subjective method, does not allow the reliable quantification of the selection effects. The effect of incompleteness does not allow us to exploit the full extent of the available data. This is particularly important for studying the low luminosity end of the SNR population and hence obtaining a more complete picture of their population and their feedback to ISM.

In this work, we present a systematic study of SNRs in 4 nearby galaxies: NGC 45, NGC 55, NGC 1313, and NGC 7793. We present a new way for the detection and characterization of the SNR population that bypasses the commonly used practice of visual inspection. This has the advantage of allowing the calculation of incompleteness, which in turn, enables the derivation of luminosity functions and more reliable statistics on the SNR populations. We do not restrict this analysis only to Hα luminosity but we also construct the joint incompleteness-corrected luminosity functions (LFs) for Hα and [S II], the two parameters that we use for the detection. This has the additional benefit of allowing the simultaneous calculation of the SNR excitation (i.e. the [S II]/Hα ratio) as a function of the Hα luminosity.

In Section 3.2, we describe the sample of the galaxies and their characteristics. In Section 3.3 and Section 3.4 we present the observations, the data reduction, the detection of SNRs and the photometric analysis. We also describe how we calculate the incompleteness corrections. The luminosity function and the excitation as a function of the Hα luminosity are presented in Section 4.3 and in Section 4.4 we discuss our results in the context of extragalactic SNR populations. In Section 3.8 we summarize our results.

3.2 Sample

Our sample consists of four southern galaxies: NGC 45, NGC 55, NGC 1313, and NGC 7793. Their basic properties are given in Table 3.1. These galaxies were selected on the basis of the following criteria: (1) They are nearby galaxies, (D<7 Mpc) in order to allow identification of individual objects; (2) There are publicly available X-ray data allowing the multi-wavelength comparison of the optical SNR population and the identification of young, X-ray emitting SNRs; (3) They are face on in order to minimize the effects of internal extinction (only NGC 55 is edge-on but it is characterized by very low extinction); (4) They are all spiral galaxies. They also have similar metallicities, limiting metallicity effects in the characterization of SNRs. The [O/H] metallicities given in Table 3.1, are calculated using the [N II]$\lambda\lambda6548, 6583$/Hα line ratios from the work of Kennicutt et al. (2008), which were converted to metallicities using the $(12 + \log(\mathrm{O/H}) = 8.9 + 0.59\log([\mathrm{N\,II}]/\mathrm{H}\alpha))$ calibration of Pettini & Pagel (2004).

This work supplements our previous multi-wavelength study of SNRs in nearby galaxies, which showed evidence for differences in SNRs between spiral and irregular galaxies. More specifically, it is seen that more luminous X-ray emitting SNRs tend to be preferentially associated with irregular galaxies (see Fig.12 of Leonidaki, Zezas, & Boumis 2010) which is attributed to different ISM density between the two types of galaxies.

All four galaxies are known to host SNRs identified in optical, radio, or X-ray wavelengths. However, the available studies are not systematic, not allowing the in-

Table 3.1: Galaxies Properties.

Galaxy	Distance* (Mpc)	Size** (arcmin)	RA (J2000) hh:mm:ss	Dec (J2000) dd:mm:ss	[O/H]
NGC 45	6.79	8.5, 5.9	00:14:03.99	-23:10:55.5	8.51
NGC 55	1.99	32.4, 5.6	00:14:53.60	-39:11:47.9	8.54
NGC 1313	4.15	9.1, 6.9	03:18:16.05	-66:29:53.7	8.62
NGC 7793	3.70	9.3, 6.3	23:57:49.83	-32:35:27.7	8.54

Col (1): The name of the galaxies; col (2) the distance of the galaxies; col (3) the size of the galaxies; col (4) and col (5): the RA and Dec of the galaxies; col (6): the metallicity of the galaxies.

*The median distance and the size characteristics are taken from NED (NASA/IPAC Extragalactic Database; http://ned.ipac.caltech.edu/).

**Major and minor axis.

vestigation of their populations in detail. From our sample, only NGC 7793 has been studied in optical wavelengths. Blair & Long (1997) detected and spectroscopically confirmed 27 SNRs, with Hα fluxes ranging from 6.7×10^{-16} to $3.6 \times 10^{-14}\,\mathrm{erg\,cm^{-2}\,s^{-1}}$. In the radio, Pannuti et al. (2002) added to those, 5 new radio SNRs and identified 2 optically known SNRs in radio and 2 in X-rays. Pannuti et al. (2011) identified X-ray counterparts for two previously detected SNRs and Della Bruna et al. (2020) confirmed in optical wavelengths two previously detected SNRs.

NGC 45 hosts a candidate SNR in radio with no X-ray counterpart and a candidate one in X-rays (Pannuti et al. 2015). NGC 55 has given 6 radio candidate SNRs that are reported to have also X-ray emission (O'Brien et al. 2013). Five SNRs have been detected in the X-ray band (Stobbart, Roberts, & Warwick 2006) and 2 of them have also emission in radio (Hummel et al. 1986). In addition, 13 more X-ray SNRs have been reported in the study of Binder et al. (2015). In NGC 1313, a probable young SNR around the supernova SN 1978K has been identified in the X-rays (Smith et al. 2007, Colbert et al. 1995; Schlegel, Petre, & Colbert 1996; Petre et al. 1994) and in radio (Achterberg & Ball 1994). Colbert et al. (1995) presents also 4 probable SNRs in X-rays.

Table 3.2: Observation details

Filters	RA (J2000)	Dec (J2000)	Exposure Time (sec)	Exposures	PSF (arcsec*)	Date
			NGC 45			
Hα + [N II]	00:14:03.48	-23:10:56.20	3600	5 × 720s	0.95	17 Nov 2011
[S II]	00:14:04.11	-23:10:37.80	7200	5 × 1440s	1.30	17 Nov 2011
R	00:14:05.10	-23:10:07.70	600	5 × 120s	1.30	17 Nov 2011
			NGC 55			
Hα + [N II]	00:14:53.95	-39:11:46.39	3600	5 × 720s	1.03	16 Nov 2011
[S II]	00:14:53.53	-39:11:47.60	7200	5 × 1440s	1.22	16 Nov 2011
R	00:14:53.67	-39:11:48.50	600	5 × 120s	1.32	16 Nov 2011
			NGC 1313			
Hα + [N II]	03:18:16.75	-66:29:52.00	3600	5 × 720s	0.95	15 Nov 2011
[S II]	03:18:17.60	-66:29:54.49	5760	4 × 1440s	1.30	16 Nov 2011
R	03:18:16.01	-66:29:53.99	600	5 × 120s	0.92	15 Nov 2011
			NGC 7793			
Hα + [N II]	23:57:49.82	-32:35:28.10	3600	5 × 720s	0.95	15 Nov 2011
[S II]	23:57:49.83	-32:35:28.20	7200	5 × 1440s	0.97	15 Nov 2011
R	23:57:49.78	-32:35:28.20	600	5 × 120s	1.05	15 Nov 2011

Col (1): The filters that were used; col (2) and col (3): the RA and Dec of each exposure; col (4) the exposure time: col (5): the number of the exposures; col (6): the PSF of the obtained images; col (7): the date of each observation.

* It is the FWHM of the PSF.

3.3 Observations and Data reduction

The data used in this work were obtained with the 4-m Blanco telescope at CTIO (Chile) on November 15-17, 2011. We used the 36” × 36” Mosaic II CCD imager which consists of 8 CCDs (2048 × 2048 SITe each) with a pixel scale of 0.27”/pixel. We used the narrow band Hα + [N II] and [S II] filters and a broadband continuum R filter. For the Hα + [N II] filter, the central wavelength is 6563Å with a FWHM of 80 Å, for the [S II] filter the central wavelength is 6725 Å with a FWHM of 80 Å, and for the R continuum, the central wavelength is 6440 Å with a FWHM of 1510 Å.

The total exposure time for each galaxy was 3600 sec for the Hα + [N II], 7200 for the [S II], and 600 sec for the R-continuum filters. The integration time for each observation was split into 5 shorter exposures. For the larger galaxies, the pointing for each of the 5 observations was shifted slightly in order to cover the chip gaps. This dither procedure ensures uniform coverage of the galaxy and efficient removal of cosmic rays. Detailed information on the observations for each galaxy is given on Table 3.2.

For the reduction of the mosaic images, we used the `mscred` package of IRAF[1] (Image Reduction and Analysis Facility; Tody 1993, 1986). Bias and flat-field corrections were performed on all images; astrometric calibrations were applied on the reduced CCD images using the 2MASS catalog and a fourth order polynomial to account for distortions at the edges of the images. The individual exposures for each object and each filter were registered and median combined with SWarp[2]

3.4 Detection and Photometry

The first step in our analysis was the detection of discrete sources in each galaxy. In order to do this, we used the program SExtractor[3] (Bertin & Arnouts 1996). SExraction was selected because in comparison to similar tools, it is more effective in the detection of fainter objects and in dense, stellar fields, and spatially varying backgrounds, with significant structure (Annunziatella et al. 2013). We ran SExtractor setting the following parameters: a) detection threshold at 2.5σ above the background, b) the minimum number of source pixels equal to 5, and c) the background mesh size at 5 pixels in order to account for small-scale background variations. From the detected sources in each

---

[1] http://ast.noao.edu/data/software

[2] https://www.astromatic.net/software/swarp

[3] https://www.astromatic.net/software/sextractor

image, we kept only those within the optical outline of the galaxy in Hα. This region is defined as the region for which the intensity in Hα is 3σ above the background.

The next step was the photometric analysis of the sources which was performed using the package `phot` of IRAF. The intensity of the detected sources was measured by means of a curve of growth analysis (i.e. we measure the source intensity in apertures of increasing radius and adopting the one maximising the signal to noise ratio). The optimal aperture radius for the majority of sources is 4.0 pixels.

In order to subtract the star-light continuum from the detected sources, for each galaxy we selected stars of moderate intensity and for each of them we calculated the intensity ratios (Hα + [NII])/R and [SII]/R where Hα, [S II], and R are the measured intensities in the Hα, [S II] and R-continuum images respectively. The mode of these ratios was used as a scaling factor for the R-continuum intensity before subtracting it from the measured Hα + [NII] and [S II] intensities. In the case of the Hα + [NII] intensities, since we need the net Hα flux, we also must remove the contamination of the [N II]$\lambda\lambda$6548,6584Å emission lines. We adopted a ([NII]$\lambda\lambda 6548, 6584$)/H$\alpha$ flux ratio of 0.3, based on emission-line measurements of spectroscopically identified SNRs of galaxies with similar metallicities of our sample (Long et al. 2018, Leonidaki, Boumis, & Zezas 2013, Blair & Long 1997).

Aiming to examine possible contamination by H II regions resulting from over-subtraction of the [N II] contamination, we considered the spectroscopic [N II]/Hα ratio of H II regions in NGC 628, NGC 925, NGC 1232, NGC 1637 (Castellanos, Díaz, & Terlevich 2002), NGC 1232 (Lima-Costa et al. 2020), NGC 300 and NGC 7793 (Blair & Long 1997), NGC 7793 (Bibby & Crowther 2010), M31 (Zurita & Bresolin 2012) and M33 (Lin et al. 2017). From the average values of the ratios reported in each of those works, the lowest is 0.19. If we had adopted the minimum ratio [N II]/Hα = 0.19, we would have a 12% contamination by H II regions in our reliable sample (candidate SNRs). However, all sources with [N II]/Hα between 0.19 and 0.3, would be included in the less reliable sample, i.e. the possible candidate SNRs, as we define at the end of this section.

In order to flux calibrate the detected sources, we used observations of standard stars from the catalogue of Massey et al (1988). We obtained photometry for these stars at different airmasses and we performed a linear fit of their instrumental magnitude against the airmass χ: $\mathrm{m} = \mathrm{m_{inst}} - \mathrm{k}\chi + \mathrm{b}$ where m is the calibrated magnitude, and k and b the slope and the intercept that are to be calculated. Hence we have:

$$\mathrm{m_v} = -2.5\log(\mathrm{f}_\nu) - 48.9 = -2.5\log(\mathrm{count\,rate}) - \mathrm{kx} + \mathrm{b}$$

where ν is the central frequency of the filter that we use. Finally, in order to convert flux density to flux, we also multiply with the FWHM (Full Width at Half Maximum) of the filter.

At this point, we have the continuum subtracted Hα and [S II] flux of every detected source. In order to find which of them are SNRs, we followed a totally automated method. From the full sample of sources, we first consider those with Hα flux above the 3σ level with respect to the local background. Then, the SNRs are identified by applying the standard [S II]/Hα > 0.4 criterion (Mathewson & Clarke 1973), considering sources with [S II]/Hα > 0.4 at the 3σ level (candidate SNRs) and at the 2σ (possible candidate SNRs). These sources were visually inspected, and some of them found to be parts of larger structures, for example rings, large bubbles and filaments. These extended sources are not considered for further analysis. All other candidate SNRs are reliable identifications, based on their appearance on the [S II] and Hα images, ensuring the reliability of the automated method.

3.4.1 Calculation of Incompleteness

During the detection process, a fraction of the sources is not detected due to their faintness in combination to their environment and stochastic effects. For this reason, our sample (as any observational sample) is characterized by incompleteness which depends on the Hα local background, the detection method, and sample selection effects. In order to evaluate this incompleteness, we followed the standard approach of placing artificial objects on our images (with the IRAF task `addstar`) using their measured PSF (determined with the IRAF package `PSF`) and in a wide range of magnitudes, covering the full brightness range of the observed objects in each filter.

Then we perform the detection exactly as we did for the actual data. The process of adding and recovering artificial sources is repeated multiple times in order to improve our statistics. In every iteration we took special care to include at most as many artificial sources as objects observed in the actual data, in order to avoid increasing the source confusion. Then, we performed aperture photometry on the artificial objects, the same way as in the actual data, keeping only the sources that are 3σ above the background in Hα, then the sources with [S II]/Hα > 0.4, and finally the sources for which the ratio is 3σ above 0.4. This results in three samples: an Hα sample, a [S II]/Hα selected sample, and a "secure" [S II]/Hα sample ([S II]/Hα > 0.4 at 3σ significance).

In order to create a 2D incompleteness map, we divide the input artificial star magnitude range of the (Hα, S II) plane, in 2 dimensional bins, and we calculate the fraction of input and detected objects (after applying all relevant selection criteria) for each ($L_{H\alpha}, L_{[S\,II]}$) bin. This comparison is performed on the continuum-subtracted fluxes: the continuum subtraction is achieved by subtracting the R-band continuum flux using the same scaling factor as for the real data, since the artificial objects are placed on the same background as the actual data. So now, we have the fraction of detected/input objects (incompleteness) as a function of their Hα and [S II] intensities.

Because of the varying diffuse emission surface brightness, the incompleteness varies within each galaxy. In order to account for this variation, we calculate the incompleteness for four different background regimes for each galaxy. These are selected to trace the full range of backgrounds in which sources are detected in each galaxy. Indicatively, in Figure 3.4 we show the different regions with contours for NGC 7793.

In order to estimate the false positives (the sources that have been measured to have [S II]/Hα > 0.4 at the 3σ level while in reality they do not), from the initial artificial objects we created two sub-samples, one for sources with input [S II]/Hα ratio between 0.2 and 0.3, and one for input ratio between 0.3 and 0.4. Then, we examined what fraction of sources detected with ratio > 0.4 belongs to these two sub-samples.

3.5 Results

3.5.1 Candidate SNRs

In total, we detected 43 candidate SNRs (with [S II]/Hα ratio 3σ above the 0.4 threshold, 30 of which are new identifications) and 54 new possible candidate SNRs (with [S II]/Hα ratio 2σ above the 0.4 threshold). In addition, some of the knots that present high excitation ([S II]/Hα > 0.4), in both 3σ and 2σ samples, are part of larger structures (i.e shells, bubbles etc, with sizes from ~ 40 pc $- \sim 320$ pc). In total, we identify 21 such structures, with those with small radii (i.e. < 100 pc) probably being SNRs. These objects are not considered in our candidate SNR samples, but they are reported for completeness and follow-up observations.

In Table 3.3, we present the candidate SNRs ($> 3\sigma$). The first column gives the ID of the source, the second and the third columns give the RA and Dec coordinates (in J2000), the fourth and fifth columns give the Hα and [S II] fluxes with their uncertainties, and the sixth column gives the [S II]/Hα ratio with its uncertainty. Figures 3.1 - 3.4 show the location of the candidate SNRs (yellow circles) overlaid on the Hα images for each galaxy.

We see that SNRs are generally located in star-forming regions as demonstrated by their strong Hα emission. In the case of NGC 45, NGC 1313 and NGC 7793 we see a deficit of sources in their central region. This is the result of high background in these regions, resulting in significant incompleteness. The possible candidate SNRs ($> 2\sigma$) are presented in the Section 3.7.

The white circles in figures 3.1 - 3.4 are the larger structures, with their size indicating their physical size. These structures along with the respective detected knots are presented in Table 3.4, where we also give their size. We show some of them in Figure 3.5.

Table 3.3: Candidate SNRs

ID	RA (J2000) hh:mm:ss	Dec (J2000) dd:mm:ss	$\mathrm{F_{H\alpha}} \pm \delta\mathrm{F_{H\alpha}}$ $(10^{-16}\,\mathrm{erg\,s^{-1}\,cm^{-2}})$	$\mathrm{F_{[SII]}} \pm \delta\mathrm{F_{[SII]}}$ $(10^{-16}\,\mathrm{erg\,s^{-1}\,cm^{-2}})$	$\frac{\mathrm{F_{[SII]}}}{\mathrm{F_{H\alpha}}} \pm (\delta\frac{\mathrm{F_{[SII]}}}{\mathrm{F_{H\alpha}}})$
NGC 45 (3σ)					
1	00:14:06.2	-23:11:17.0	5.91 ± 0.34	4.23 ± 0.41	0.72 ± 0.08
2	00:14:00.4	-23:11:21.6	19.20 ± 0.55	12.70 ± 0.54	0.66 ± 0.03
3	00:14:07.3	-23:10:54.8	3.84 ± 0.24	3.04 ± 0.26	0.79 ± 0.08
4	00:14:03.8	-23:10:01.0	53.70 ± 0.60	27.00 ± 0.52	0.50 ± 0.01
5	00:14:03.3	-23:08:22.1	11.90 ± 0.59	8.14 ± 0.52	0.68 ± 0.06
6	00:14:11.8	-23:12:57.4	4.29 ± 0.28	2.85 ± 0.26	0.66 ± 0.07
7	00:14:05.1	-23:11:50.0	5.50 ± 0.32	2.99 ± 0.29	0.54 ± 0.06
8	00:13:58.9	-23:08:29.7	4.66 ± 0.28	2.77 ± 0.28	0.59 ± 0.07
NGC 55 (3σ)					
1	00:15:43.2	-39:16:03.0	7.59 ± 0.48	6.65 ± 0.54	0.88 ± 0.09
2	00:15:01.7	-39:13:03.1	10.9 ± 0.62	6.94 ± 0.65	0.63 ± 0.07
3	00:14:48.2	-39:11:26.1	60.4 ± 1.9	42.6 ± 2.0	0.71 ± 0.04
4	00:14:37.3	-39:11:09.8	19.1 ± 0.83	12.2 ± 0.8	0.64 ± 0.05
NGC 1313 (3σ)					
1	03:17:37.1	-66:31:13.9	9.51 ± 0.37	5.30 ± 0.30	0.56 ± 0.04
2	03:18:01.5	-66:29:13.6	12.2 ± 0.91	8.64 ± 0.75	0.71 ± 0.08
3	03:18:40.3	-66:29:14.3	59.9 ± 0.57	32.3 ± 0.56	0.54 ± 0.01
4	03:18:20.3	-66:29:00.9	6.82 ± 0.64	5.06 ± 0.54	0.74 ± 0.10
5	03:18:21.0	-66:29:00.3	15.1 ± 0.89	10.1 ± 0.64	0.67 ± 0.06
6	03:18:26.1	-66:27:41.8	15.8 ± 0.42	11.3 ± 0.44	0.71 ± 0.03
NGC 7793 (3σ)					
1	23:57:45.0	-32:37:40.2	16.0 ± 0.63	16.0 ± 0.51	0.98 ± 0.05
2	23:57:37.0	-32:36:14.9	8.8 ± 0.54	7.1 ± 0.55	0.81 ± 0.08
3	23:58:06.5	-32:35:37.0	11.0 ± 0.33	9.9 ± 0.41	0.88 ± 0.05
4	23:57:38.7	-32:34:38.5	6.4 ± 0.48	8.1 ± 0.6	1.30 ± 0.10
5	23:57:52.2	-32:34:13.4	10.0 ± 0.32	6.6 ± 0.43	0.66 ± 0.05
6	23:57:52.6	-32:33:54.4	5.0 ± 0.4	5.7 ± 0.39	1.10 ± 0.10
7	23:57:48.6	-32:33:45.4	3.4 ± 0.38	3.1 ± 0.39	0.90 ± 0.10
8	23:57:48.2	-32:33:37.7	5.4 ± 0.49	5.4 ± 0.47	0.99 ± 0.10
9	23:57:41.1	-32:37:02.1	24.0 ± 1.2	21.0 ± 0.93	0.88 ± 0.06

10	23:57:44.3	-32:35:32.1	6.2 ± 0.44	7.3 ± 0.47	1.20 ± 0.10
11	23:57:44.0	-32:35:31.7	6.6 ± 0.48	6.1 ± 0.5	0.94 ± 0.10
12	23:57:43.8	-32:35:27.8	24.0 ± 0.89	23.0 ± 1.3	0.95 ± 0.06
13	23:57:54.5	-32:35:12.2	16.0 ± 1.0	18.0 ± 1.4	1.20 ± 0.10
14	23:57:57.2	-32:34:55.9	4.9 ± 0.45	5.9 ± 0.56	1.20 ± 0.20
15	23:57:46.0	-32:34:30.1	6.9 ± 0.92	6.7 ± 0.72	0.97 ± 0.20
16	23:57:57.5	-32:34:21.9	27.0 ± 1.6	22.0 ± 1.2	0.82 ± 0.07
17	23:58:00.3	-32:34:12.2	100.0 ± 2.5	53.0 ± 2.5	0.51 ± 0.03
18	23:57:56.1	-32:37:18.5	56.0 ± 1.9	36.0 ± 2.2	0.64 ± 0.05
19	23:57:48.3	-32:36:55.2	73.0 ± 2.3	52.0 ± 1.7	0.70 ± 0.03
20	23:57:51.2	-32:36:31.7	38.0 ± 1.9	48.0 ± 2.2	1.30 ± 0.09
21	23:57:59.2	-32:36:06.0	140.0 ± 2.4	83.0 ± 2.5	0.61 ± 0.02
22	23:57:47.3	-32:35:23.9	110.0 ± 3.0	88.0 ± 3.0	0.82 ± 0.04
23	23:57:45.8	-32:35:01.7	33.0 ± 0.77	33.0 ± 0.84	1.00 ± 0.03
24	23:57:44.0	-32:34:41.3	50.0 ± 1.8	27.0 ± 1.8	0.54 ± 0.04

(The entire sample is available in the on-line version; see Table 3.7.)

Table 3.4: Candidate SNRs - Large structures

ID	RA (J2000) hh:mm:ss	Dec (J2000) dd:mm:ss	$F_{H\alpha} \pm \delta F_{H\alpha}$ ($10^{-16}\,\mathrm{erg\,s^{-1}\,cm^{-2}}$)	$F_{[SII]} \pm \delta F_{[SII]}$ ($10^{-16}\,\mathrm{erg\,s^{-1}\,cm^{-2}}$)	$\frac{F_{[SII]}}{F_{H\alpha}} \pm (\delta \frac{F_{[SII]}}{F_{H\alpha}})$	Size (pc)
NGC 7793						
0	**23:57:44.1**	**-32:36:39.1**	**131.5 ± 4.1**	**93.5 ± 4.5**	**0.71 ± 0.02**	**101**
0a	23:57:44.0	-32:36:38.5	7.1 ± 0.56	5.2 ± 0.69	0.74 ± 0.1	
1	**23:57:45.4**	**-32:36:03.4**	**374.9 ± 13.5**	**119.7 ± 17.5**	**0.32 ± 0.01**	**218**
1a	23:57:45.4	-32:35:58.3	5.7 ± 0.5	4.7 ± 0.75	0.82 ± 0.1	
2	**23:57:55.3**	**-32:34:34.4**	**214.0 ± 4.7**	**125.3 ± 4.7**	**0.59 ± 0.01**	**93**
2a	23:57:55.4	-32:34:32.9	12 ± 1.7	12 ± 1.7	0.97 ± 0.2	
2b	23:57:55.4	-32:34:36.2	31 ± 1.3	26 ± 2	0.83 ± 0.07	
3	**23:57:47.5**	**-32:34:08.2**	**68.3 ± 3.5**	**23.8 ± 3.0**	**0.35 ± 0.02**	**89**
3a	23:57:47.4	-32:34:08.4	6.8 ± 1.6	7.8 ± 1.3	1.1 ± 0.3	
4	**23:57:38.8**	**-32:33:20.8**	**99.8 ± 1.8**	**42.7 ± 2.0**	**0.43 ± 0.01**	**101**
4a	23:57:38.8	-32:33:18.5	12 ± 1.3	8.4 ± 0.76	0.73 ± 0.1	
5	**23:57:39.2**	**-32:35:38.1**	**58.6 ± 1.1**	**52.4 ± 1.1**	**0.89 ± 0.02**	**71**
5a	23:57:39.2	-32:35:36.7	16 ± 1.1	9.1 ± 1.1	0.59 ± 0.08	
5b	23:57:39.2	-32:35:39.2	9.8 ± 0.69	11 ± 0.54	1.1 ± 0.09	
6	**23:57:59.8**	**-32:33:20.5**	**1199.0 ± 8.7**	**786.9 ± 9.9**	**0.66 ± 0.00**	**322**
6a	23:57:59.8	-32:33:15.4	338.4 ± 7.8	213.3 ± 6.0	0.63 ± 0.01	151
6a_i	23:57:59.7	-32:33:17.1	16.0 ± 1.0	11 ± 0.75	0.73 ± 0.07	
6a_ii	23:58:00.0	-32:33:17.9	31.0 ± 2.3	24 ± 1.8	0.8 ± 0.08	
6a_iii	23:58:00.0	-32:33:15.2	32.0 ± 1.8	22 ± 1.4	0.7 ± 0.06	
6a_iv	23:57:59.8	-32:33:12.3	10.0 ± 0.8	6.2 ± 0.39	0.6 ± 0.06	
6a_v	23:57:59.6	-32:33:13.6	14.0 ± 1.1	11 ± 1.1	0.81 ± 0.1	
6b	23:58:00.1	-32:33:23.0	690.3 ± 4.3	485.0 ± 4.1	0.70 ± 0.00	135
6b_i	23:58:00.2	-32:33:22.1	100 ± 3.7	66 ± 3.2	0.65 ± 0.04	
6b_ii	23:58:00.1	-32:33:25.2	130 ± 5.6	120 ± 4.3	0.9 ± 0.05	
6b_iii	23:57:59.7	-32:33:23.2	4.8 ± 0.68	4 ± 0.62	0.83 ± 0.2	
7	**23:58:01.1**	**-32:34:03.8**	**242.6 ± 13.8**	**36.5 ± 9.6**	**0.15 ± 0.01**	**169**
7a	23:58:01.3	-32:34:05.6	9.3 ± 1.3	7.2 ± 0.72	0.78 ± 0.1	
8	**23:57:59.5**	**-32:33:52.2**	**171.4 ± 11.6**	**52.1 ± 11.2**	**0.30 ± 0.02**	**222**
8a	23:57:59.7	-32:33:49.3	5.4 ± 0.78	5.8 ± 0.85	1.1 ± 0.2	
8b	23:57:59.8	-32:33:54.5	5.6 ± 0.46	5.1 ± 0.41	0.92 ± 0.1	
8c	23:57:59.4	-32:33:56.7	5.2 ± 0.59	5.4 ± 0.59	1 ± 0.2	
8d	23:57:59.0	-32:33:52.9	2.6 ± 0.43	2.8 ± 0.41	1.1 ± 0.2	
NGC 55						
0	**00:15:47.3**	**-39:16:28.1**	**987.1 ± 40.4**	**507.0 ± 49.3**	**0.51 ± 0.02**	**124**
0a	00:15:54.6	-39:15:10.2	6.19 ± 0.67	4.21 ± 0.57	0.68 ± 0.1	
0b	00:15:54.0	-39:15:19.7	19.3 ± 1.1	13.7 ± 0.96	0.71 ± 0.06	
0c	00:15:54.5	-39:15:29.8	4.18 ± 0.59	3.49 ± 0.49	0.83 ± 0.2	
1	**00:15:54.9**	**-39:15:21.6**	**368.5 ± 11.6**	**147.9 ± 13.0**	**0.40 ± 0.01**	**257**
1a	00:15:46.8	-39:16:28.6	5.39 ± 0.83	5.87 ± 0.72	1.1 ± 0.2	

2	**00:15:42.3**	**-39:16:19.5**	**5.1 ± 1.2**	**4.7 ± 1.4**	**0.91 ± 0.21**	**41**
2a	00:15:42.5	-39:16:19.2	2.1 ± 0.33	2.48 ± 0.41	1.2 ± 0.3	
2b	00:15:42.3	-39:16:18.9	1.88 ± 0.29	1.95 ± 0.39	1 ± 0.2	
3	**00:15:39.8**	**-39:15:21.4**	**269.5 ± 7.3**	**65.2 ± 6.3**	**0.24 ± 0.01**	**97**
3a	00:15:41.0	-39:15:38.8	10.1 ± 1.5	7.97 ± 0.85	0.79 ± 0.1	
4	**00:15:01.9**	**-39:13:17.7**	**22.3 ± 11.9**	**26.2 ± 13.0**	**1.18 ± 0.74**	**89**
4a	00:15:39.6	-39:15:18.6	3.63 ± 0.47	2.79 ± 0.51	0.77 ± 0.2	
5	**00:14:53.9**	**-39:10:56.6**	**145.0 ± 14.7**	**63.5 ± 17.2**	**0.44 ± 0.04**	**126**
5a	00:15:01.9	-39:13:13.3	2.87 ± 0.54	2.46 ± 0.47	0.86 ± 0.2	
6	**00:14:35.7**	**-39:10:02.2**	**179.7 ± 25.8**	**134.8 ± 34.1**	**0.75 ± 0.11**	**81**
6a	00:14:53.3	-39:10:55.7	1.91 ± 0.59	2.97 ± 0.48	1.6 ± 0.5	
7	**00:14:24.4**	**-39:10:28.3**	**112.1 ± 10.1**	**86.3 ± 12.8**	**0.77 ± 0.07**	**52**
7a	00:14:35.6	-39:09:59.5	5.23 ± 0.48	3.31 ± 0.49	0.63 ± 0.1	
8	**00:15:41.0**	**-39:15:38.5**	**26.2 ± 1.4**	**15.0 ± 1.6**	**0.57 ± 0.03**	**79**
8a	00:14:24.2	-39:10:28.6	3.86 ± 0.35	2.50 ± 0.38	0.65 ± 0.1	
			NGC 1313			
0	**03:18:16.8**	**-66:34:38.4**	**153.0 ± 2.8**	**117.3 ± 2.8**	**0.77 ± 0.01**	**157**
0a	03:18:17.1	-66:34:35.2	5.49 ± 0.82	4.80 ± 0.62	0.88 ± 0.2	

The larger structures (indicated in bold), along with the respective knots that we detected. The last column gives the physical size of the structures.

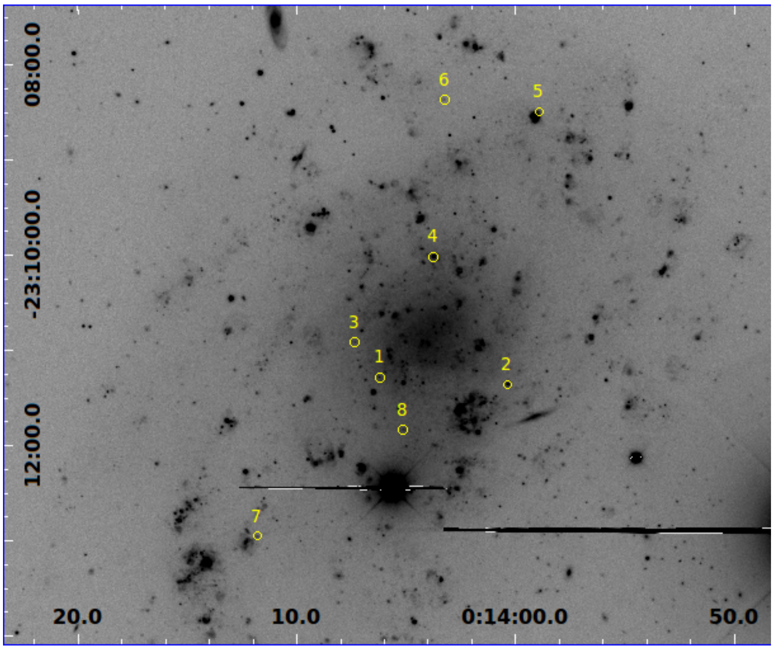

Figure 3.1: **NGC 45**: The candidate SNRs (yellow circles) and the larger structures (white circles) overlaid on the Hα + [N II] image. In this galaxy we identified 8 candidate SNRs with [S II]/Hα ratio 3σ above 0.4. The flux of the faintest source in Hα is 3.8$\times 10^{-16}$erg cm^{-2} s^{-1}.

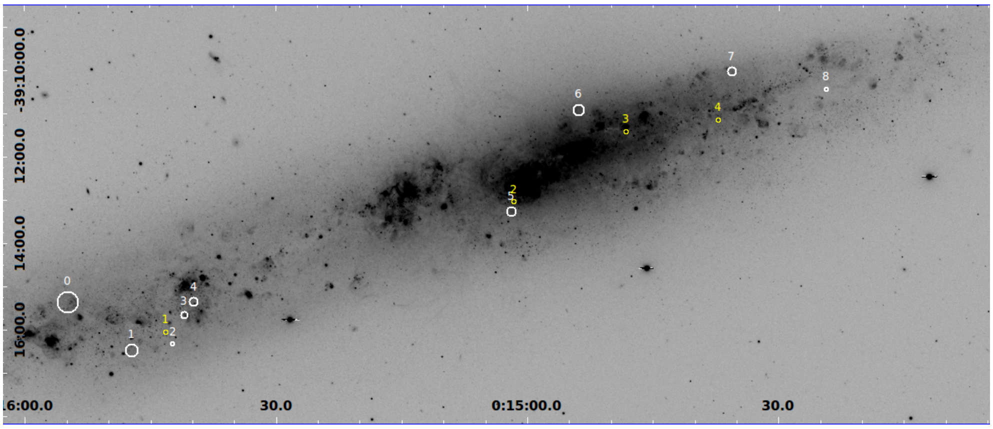

Figure 3.2: **NGC 55**: The candidate SNRs (yellow circles) and the larger structures (white circles) overlaid on the Hα + [N II] image. In this galaxy we identified 4 candidate SNRs with [S II]/Hα ratio 3σ above 0.4. The flux of the faintest source in Hα is 7.59$\times 10^{-16}$erg cm^{-2} s^{-1}.

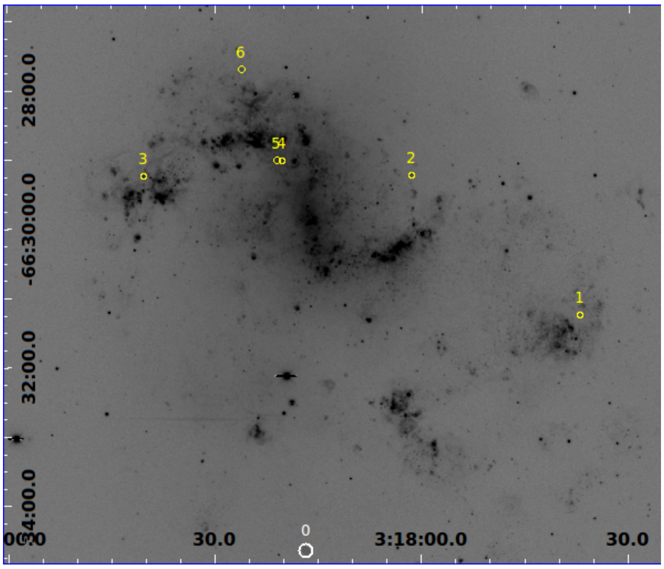

Figure 3.3: NGC 1313: The candidate SNRs (yellow circles) and the larger structures (white circles) overlaid on the Hα + [N II] image. In this galaxy we identified 6 candidate SNRs with [S II]/Hα ratio 3σ above 0.4. The flux of the faintest source in Hα is $6.8{\times}10^{-16}$erg cm^{-2} s^{-1}

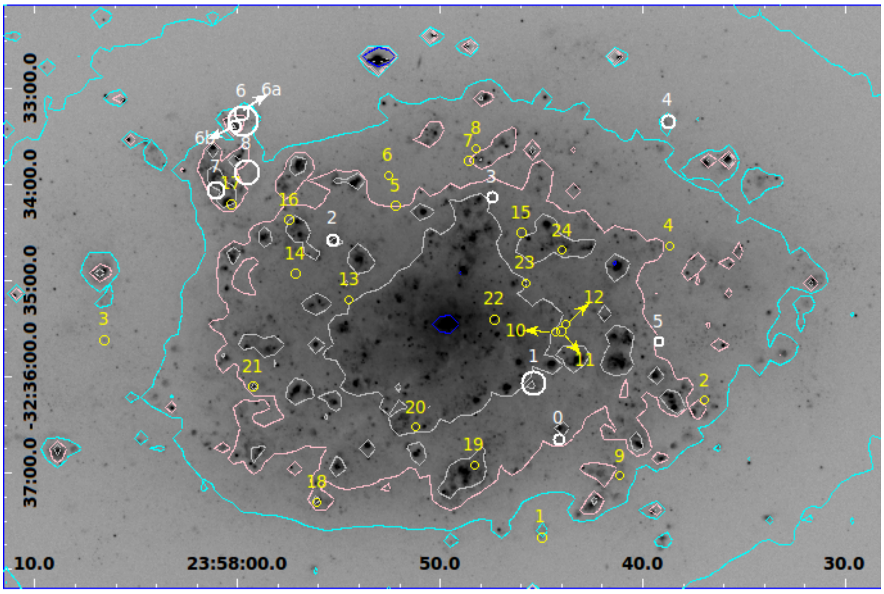

Figure 3.4: NGC 7793: The candidate SNRs (yellow circles) and the larger structures (white circles) overlaid on the Hα + [N II] image. In this galaxy we identified 24 candidate SNRs with [S II]/Hα ratio 3σ above 0.4. The flux of the faintest source in Hα is $3.4{\times}10^{-16}$erg cm^{-2} s^{-1}. The contours show the different background regions for which we calculated the incompleteness. Cyan color is for regions with background 500-600 counts, pink color is for background 600-800 counts, grey color is for background 800-1100 counts, and blue color is for background 1100-3000 counts.

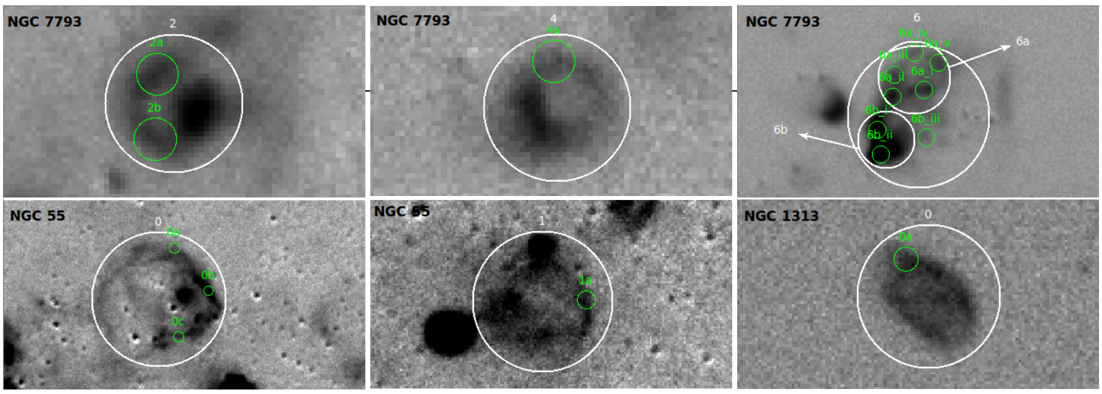

Figure 3.5: Indicative postage-stamp continuum subtracted Hα + [N II] images of some of the larger structures presented in Table 3.4. The white circles indicate the outline of the structures, while the green circles show the location of the detected knots.

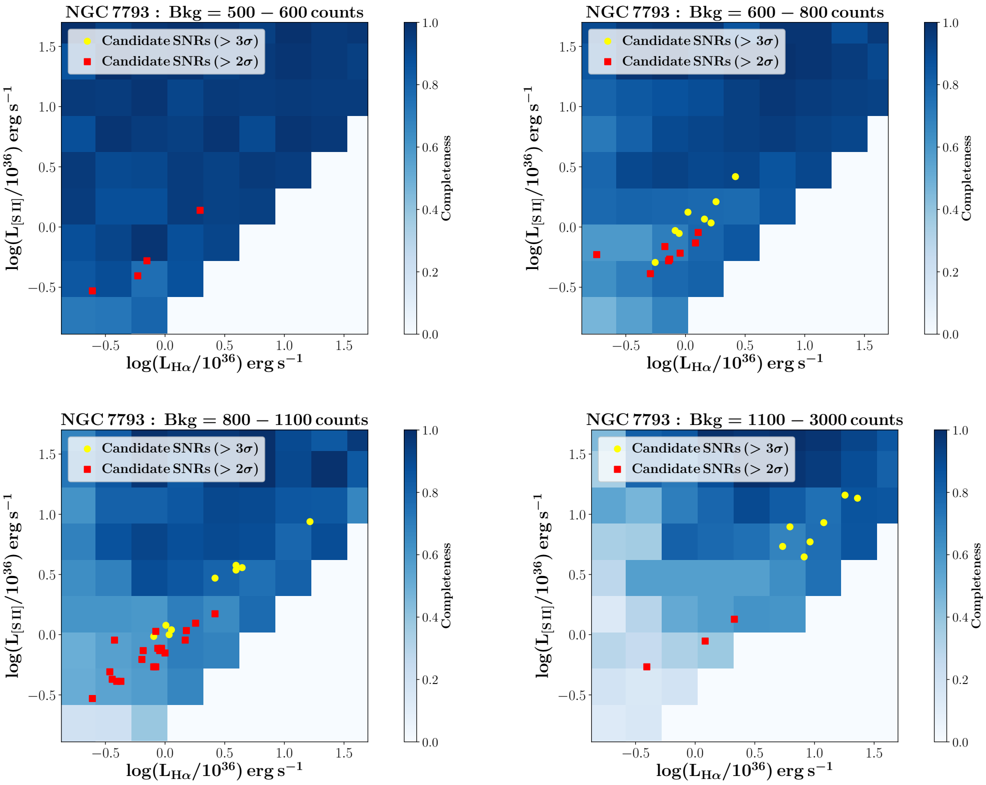

Figure 3.6: Two dimensional Hα - [S II] incompleteness maps for the candidate SNRs (with [S II]/Hα ratio 3σ and 2σ above 0.4 respectively) in NGC 7793, for 4 different backgrounds. Darker colors indicate lower incompleteness (more complete samples). The points show the location of the candidate SNRs (yellow circles) and possible candidate SNRs (red squares) on the (Hα, [S II]) plane.

3.5.2 Luminosity functions (LFs)

3.5.2.1 Hα luminosity function

In order to measure the Hα luminosity function (Hα − LF) free of selection effects, we need to apply the incompleteness function. The incompleteness-corrected number of sources is calculated by defining the quantity $1/\mathrm{I_i}$ where $\mathrm{I_i}$ is the completeness corresponding to each source, given their [S II], Hα luminosity (see § 3.4.1). The completeness of each source depends on its local background. As described in § 3.4.1, we derive completeness maps for four different background regimes.

Indicatively, in Figure 3.6 we present the incompleteness maps for NGC 7793 for the different backgrounds. The x and y axis correspond to the logarithm of the Hα and [S II] luminosities respectively, and the degradation of the blue scale indicates the completeness for each combination of [S II] and Hα luminosity. On these maps, we also show the detected candidate SNRs ($> 3\sigma$; yellow circles) and the possible candidate SNRs ($> 2\sigma$; red squares). As we see, the highest completeness is close to 100%.

For the calculation of Hα LF we consider only the candidate SNRs (and not the possible candidate SNRs), and we also exclude any sources associated with larger structures (Table 3.4) since they could be knots in larger filaments or super-bubbles. The incompleteness maps that we use in order to correct these sources, have been constructed using artificial objects that satisfy exactly the same criteria used to select the candidate SNRs (i.e. [S II]/Hα ratio, 3σ above 0.4). The larger structures are not included in this analysis, since our detection method is not optimized for extended objects and we cannot apply the incompleteness correction, which is based on point-like sources (§3.4.1).

Figure 3.7 shows the binned differential incompleteness-corrected Hα luminosity functions for the candidate SNRs in all galaxies (gray histogram). The incompleteness corrected number of sources for each luminosity bin is given by the sum $\sum_{\mathrm{i}}(1/\mathrm{I_i})$ for all sources within each Hα bin. For reference, the solid-line histogram shows the observed (uncorrected) binned Hα luminosity distribution. We see, that as expected, in general, the effect of incompleteness is more significant for the lower luminosity sources. However, even in the bright end the completeness is never 100% because of the selection in the [S II] emission lines and the high background in which we find the more luminous SNRs.

We fit the $\mathrm{LF_{H\alpha}}$ by performing a maximum likelihood fit on the un-binned data. We fit a model described by a skewed Gaussian function (in the log(L)) in order to account for the asymmetric shape of the LFs (Figure 3.7). The skewed-Gaussian distribution is given by the function:

$$\mathrm{f(logL)} = \frac{\mathrm{A}}{\sigma\sqrt{(2\pi)}}\mathrm{e}^{\frac{-(\mathrm{logL}-\mu)^2}{2\sigma^2}}\{1+\mathrm{erf}[\frac{\alpha(\mathrm{logL}-\mu)}{\sigma\sqrt{2}}]\} \tag{3.1}$$

where μ is the mean of the distribution, σ the standard deviation, and α the skewness parameter which describes the asymmetry of the LF and potential selection effects. The incompleteness is included as a weight term in the likelihood function.

The amplitude (A), of the function reflects the total number of SNRs ($\mathrm{N_{Total}}$). The number of incompleteness corrected objects down to our faintest limit is calculated by $\mathrm{K} = \sum_{\mathrm{i=0}}^{\mathrm{N}}(1/\mathrm{I_i})$, where N is the total number of observed sources in each galaxy. Since the function used to model the luminosity function is normalized, the total number of incompleteness corrected objects (even beyond the faintest limit) and hence the amplitude factor A in eq. (4.8) is given by $\mathrm{A} = \mathrm{N_{Total}} = \mathrm{K}/\int_{\mathrm{log(L_{min})}}^{\mathrm{log(L_{max})}} \mathrm{f(log(L))d(log(L))}$, where $\mathrm{L_{min}}$ and $\mathrm{L_{max}}$ are the minimum and maximum luminosity (in this case Hα luminosity) of our sample.

For the determination of the best fit model parameters we used a Markov Chain Monte Carlo method implemented in the python package `pymc`[1]. We assume flat priors for all the parameters of interest (μ, σ, and α) and we perform 40000 iterations (excluding 500 burn-in iterations). The best-fit parameters and their uncertainties (at the 68% percentile) as derived by the posterior distribution of the model parameters are given in Table 3.5. The best-fit model to the un-binned data is shown as the solid line in Figure 3.7.

In Table 3.5 we also give the number of the detected SNRs (N) and the total number of SNRs (A; i.e. after accounting for incompleteness) of the overall sample of the 4 galaxies, and we calculate the detection fraction, which is the ratio of the number of the detected sources over the total number of SNRs (N/A). As we see, the detected SNRs can be $\sim$ 30% less than the total number of SNRs in a galaxy.

If we take into account also the possible candidate SNRs ([S II]/Hα ratio 2σ above the 0.4 threshold) we find for the Hα LF $\mu = -0.37^{+0.79}_{-0.01}$, $\sigma = 0.61^{+0.17}_{-0.03}$ and $\alpha = 1.09^{+0.20}_{-0.50}$.

3.5.2.2 The joint [S II] - Hα luminosity function

Since we have measurements of both the Hα and [S II] luminosities of the SNRs in our sample, we can also calculate their joint luminosity function (LF) which yields

---

[1] https://pymc-devs.github.io/pymc/modelfitting.html

Table 3.5: Hα Luminosity Function parameters for candidate SNRs (>3σ)

N	μ (log(L*))	σ (log(L*))	α	N_{max}	A	Detection Fraction
43	$0.07^{+0.63}_{-0.05}$	$0.58^{+0.11}_{-0.09}$	1.70(> 0.48)	8.62 ± 1.32	59.83 ± 9.17	0.72 ± 0.11

Col (1): the number of candidate SNRs (> 3σ) of all galaxies; col (2) and col (3): the mean and sigma of the Hα luminosity function respectively; col (4): the skewness parameter of the Hα luminosity function; col (5): the model-based number of sources at the bin corresponding to the peak of the distribution; col (6): the total number of SNRs; col (7): the ratio of the number of the detected sources over the total number of SNRs (N/A).

*Luminosity in units of 10^{36} erg s^{-1}

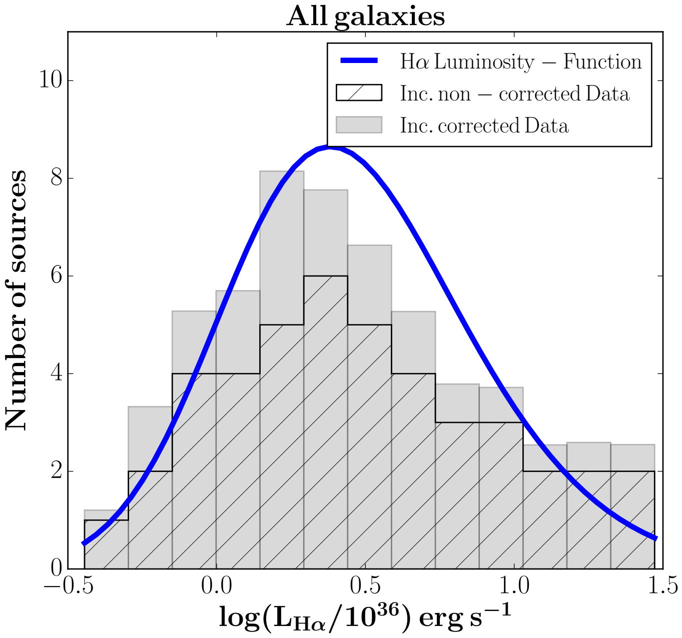

Figure 3.7: The incompleteness-corrected Hα luminosity function of the candidate SNRs (with ([S II]/Hα - 0.4) > 3σ; gray histogram), plotted along with the observed luminosity function without any incompleteness correction (black-line histogram). The blue curve shows the best-fit LF$_{H\alpha}$ fitted to the incompleteness-corrected data.

information on the luminosity and excitation of the SNR populations. The location of the sources on the Hα - [S II] luminosity plane is shown in Figure 3.8.

To quantify the shape of the [S II]-Hα joint distribution for the candidate SNRs (and not the possible candidate SNRs), we adopt the following approach. We first calculate the relation between the log($L_{[\mathrm{S\,II}]}$) and log($L_{\mathrm{H}\alpha}$) luminosity for the detected sources. The best-fit relation is log([S II]) = 0.88log(Hα) - 0.06. This is the "spine" of the distribution of the candidate SNRs on the [S II]-Hα plane, shown by the blue line in Figure 3.8.

Then, we project all the points on the best-fit line (i.e. for each Hα we calculate the log([S II]) - y = log([S II]) - (0.88log(Hα) - 0.06)). We then fit a skewed Gaussian to the distribution of these points along the best-fit line, applying the incompleteness correction for each source (considering each source i as 1/Ii; § 3.5.2.1). As for the Hα LF, we use a Markov Chain Monte Carlo method, assuming flat priors for all the parameters of interest (μ, σ, and α) and performing 40000 iterations (excluding 500 burn-in iterations). The best-fit parameters of the 2D LF, are presented in Table 3.6. If we take into account also the possible candidate SNRs ([S II]/Hα ratio 2σ above the 0.4 threshold) the the parameters μ, σ and α parameters of the 2D [S II] - Hα LF are $-0.34^{+0.66}_{-0.04}$, $0.53^{+0.14}_{-0.03}$ and $0.57^{+0.67}_{-0.07}$ respectively.

In order to obtain a full picture of the 2D Hα - [S II], we also need to measure the scatter of the candidate SNRs around the "spine" of the [S II] - Hα distribution (the best-fit line derived above). In order to do so, we calculate the distance of each source from the best-fit [S II] - Hα line, on the [S II] axis. The distribution of these distances is described by a truncated Gaussian the fit parameters of which have been calculated using the same approach as above. The μ and σ values of the truncated Gaussian are $0.024^{+0.025}_{-0.024}$ and $0.14^{+0.018}_{-0.029}$ respectively. The sigma is considered as the width of the 2D LF. The joint [S II]-Hα LF is presented in Figure 3.9.

The total number of SNRs may be affected by the number of false positives: i.e. sources which satisfy the [S II]/Hα > 0.4 criterion even at the 3σ level, while in reality they have lower [S II]/Hα ratios. Such sources could be H II regions, with [N II]/Hα ratio different than the one that we have adopted for our analysis. However, based on the analysis presented in §3.4.1 we calculate that the fraction of sources with intrinsic [S II]/Hα ratios between 0.2-0.3 and 0.3-0.4, that are found to satisfy our [S II]/Hα > 0.4 criterion at the 3σ level, is only 0.3% - 1.0% for the different galaxies in our sample and for the different backgrounds in each galaxy. Therefore, we consider the contamination by lower excitation sources negligible.

Table 3.6: [S II] - Hα Luminosity Function parameters for candidate SNRs (>3σ)

Axis	N	μ (log(L*))	σ (log(L*))	α	N$_{\rm max}$	A	Detection fraction
$L = 0.88\log(L_{H\alpha}) - 0.06$	43	$-0.03^{+0.56}_{-0.03}$	$0.48^{+0.13}_{-0.05}$	1.73(>1.69)	7.62 ± 1.17	59.38 ± 9.10	0.72 ± 0.01
$\log(L_{[S\,II]}/10^{36})$	-	$0.024^{+0.025}_{-0.024}$	$0.14^{+0.02}_{-0.03}$	-	-	-	-

Col (1): the number of candidate SNRs (>3σ) of all galaxies; col (2) and col (3): the mean and sigma values of the joint [S II] - Hα luminosity function respectively (for the skewed Gaussian along the line $y = 0.88x - 0.06$ which shows the shape of the LF; first row, and for the truncated Gaussian on the [S II] axes, i.e the distance of the [S II] from the line $y = 0.88x - 0.06$, which shows the width of the LF; second row); col (4): the skewness parameter of the joint [S II] - Hα luminosity function; col (5): the model-number of the sources at the bin that corresponds to the peak of the distribution; col (6): the total number of candidate SNRs (even beyond the lower limit); col (7): the ratio of the number of the detected sources over the total number of candidate SNRs (N/A).

* $L = 0.88\log(L_{H\alpha}) - 0.06$ (first row), and $L = L_{[S\,II]}$ (second row), in units of 10^{36} erg s^{-1}

3.5.3 Excitation Function

An alternative way to view the 2D luminosity function, is in terms of the excitation of the SNRs, which is described by their [S II]/ Hα ratio. For this reason, we calculate the number density of SNRs, as function of their distance from the limiting [S II]/ Hα = 0.4 line, which is the threshold for SNR classification.

In Figure 3.8, this distance corresponds to different [S II]/Hα ratios (i.e. different excitation). As we can see, there is a trend for SNRs with higher Hα luminosity, to present increasingly lower excitation. In order to quantify this trend, we fit a linear relation to the orthogonal distances from the 0.4 line, as function of the Hα luminosity: $D = \alpha\log(H\alpha) + \beta$ (Figure 3.10). We find $\alpha = -0.09$ and $\beta = 0.26$, indicating a sub-linear relation, i.e. more luminous objects tend to have lower excitation.

We introduce the excitation function as the vertical distribution of the candidate SNRs with respect to $D = -0.09\log(H\alpha) + 0.26$ (Figure 3.10). Then, we calculate the distance of each source from this line, in order to quantify the spread around the excitation function. The difference between the excitation function and the 2D [S II] - Hα LF, is that in the latter, the y-dimension corresponds to the [S II] luminosity. While one can derive the excitation function from the 2D [S II] - Hα LF, for simplicity and more direct assessment of the excitation of SNRs, we also introduce the excitation function. The distribution of these distances are presented in Figure 3.11 (blue histogram).

This distribution is described by a truncated Gaussian, the best parameters of which are: $\mu = -0.014^{+0.011}_{-0.051}$ and $\sigma = 0.11^{+0.04}_{-0.21}$. The fitted truncated Gaussian has been calculated for the incompleteness-corrected candidate SNRs and it is presented in Figure 3.11 (black line). If we take into account also the possible candidate SNRs ([S II]/Hα ratio 2σ above the 0.4 threshold) the parameters μ, and σ of the excitation function are $-0.004^{+0.009}_{-0.014}$, and $0.10^{+0.01}_{-0.19}$ respectively. In this case the sub-linearity is characterized by a slope -0.10.

3.6 Discussion

3.6.1 Comparison with other surveys

In our survey we have detected in total 43 candidate SNRs (30 of which are new identifications) and 54 new possible candidate SNRs. This is a significant contribution to the number of known optical extragalactic SNRs. In addition, we find 21 sources with [S II]/H$\alpha > 0.4$ at both 3σ and 2σ levels, which are associated with larger structures. The size of these structures ranges from ~ 40 to ~ 320 pc. Those with size < 100 pc could be evolved SNRs (Franchetti et al. 2012). If the size of an SNR is 100 pc, its surrounding ISM has density 10 cm^{-3} and the explosion energy was 10^{51} erg, then, according to Sedov-Taylor solution (Draine 2011), its age is ~ 100000 years, i.e. an old SNR.

In this study we present for the first time optical SNR candidates in NGC 45, NGC 55, and NGC 1313. NGC 7793 has been studied before by Blair & Long (1997) who presented 27 SNRs. Almost all these SNRs have been also identified in our deeper survey which yields 24 candidate SNRs (13 of which coincide with those of Blair & Long (1997)) and 31 possible candidate SNRs. Five of the SNRs that are reported in the work of Blair & Long (1997) (s2, s3, s7, s18, s2, s26ext) coincide with 5 (out of 8) larger structures that we detected in this galaxy. Some SNRs of the study of Blair & Long 1997 have [S II]/Hα ratio less than 2σ above the 0.4 limit in our study so they are not discussed in this paper (s9, s17, s21, s22, s27). We do not identify as SNRs sources s4, s19, s23, s15 in the catalogue of Blair & Long (1997). Sources s4, s19 and s15 have [S II]/Hα ratio 0.31, 0.36, and 0.17 respectively, i.e. below our 0.4 limit. Source s23 instead, is resolved into multiple sources in our images none of which gives high [S II]/Hα ratio.

Large samples of extragalactic SNRs have been presented in many surveys. In M31 (Lee & Lee 2014a) and M33 (Lee & Lee 2014b) have been detected 156 and 199 photometric SNRs respectively. Matonick & Fesen (1997) identified 93 SNRs in M101 and 41 SNRs in M81. Surveys led by Blair et al. (2014), Dopita et al. (2010) and

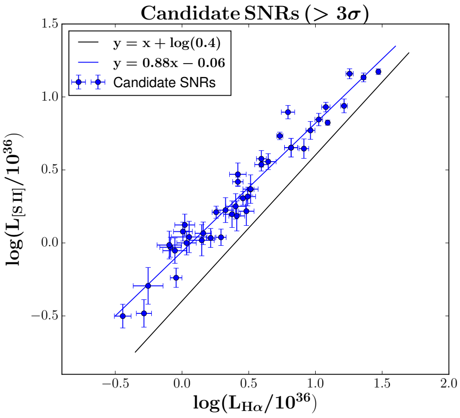

Figure 3.8: A scatter plot of the [S II] and Hα luminosity of the candidate SNRs. The black line shows the [S II]/Hα = 0.4 threshold. The blue line shows the best-fit log($L_{\mathrm{[S\,II]}}$) - log($L_{\mathrm{[H\alpha]}}$) relation for the sample of candidate SNRs.

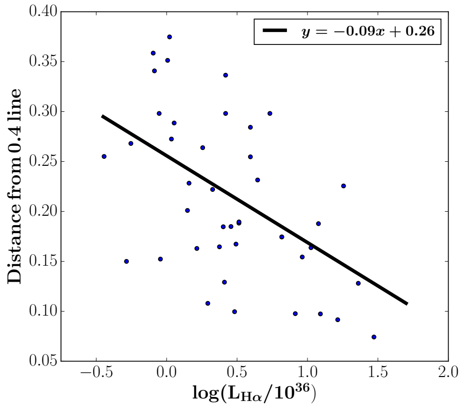

Figure 3.10: The points show the distance of each source from the [S II]/Hα = 0.4 line. The black line is the best fit line that describes the distance of the candidate SNRs from the [S II]/Hα = 0.4 line as function of their Hα luminosity.

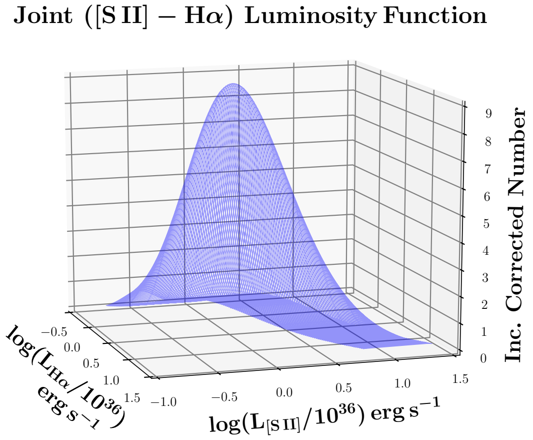

Figure 3.9: The joint [S II] - Hα luminosity function along the best-fit line: $\log(L_{\mathrm{[S\,II]}}/10^{36}) = 0.88\log(L_{\mathrm{[H\alpha]}}/10^{36}) - 0.06$. The parameters of the joint LF are presented in Table 3.6. In order to obtain the 3D interpretation, we multiply the skewed Gaussian that describes the shape of the joint LF along the best-fit line, with the truncated Gaussian that describes the width of the joint LF on the [S II] dimension.

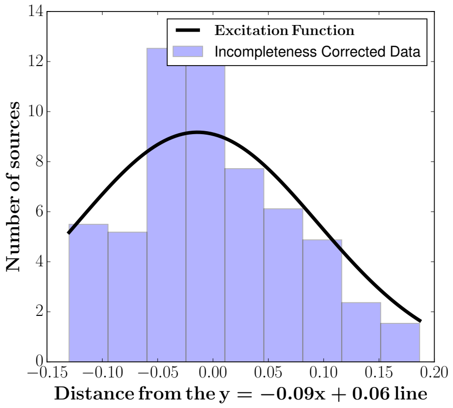

Figure 3.11: The histogram is the incompleteness-corrected source distance from the best-fit line of Figure 3.10 distribution (§ 3.5.3), and the black line is the fitted excitation function, described by a truncated Gaussian with $\mu(\log(L_{\mathrm{[S\,II]}}/10^{36})) = 0.024$ and $\sigma(\log(L_{\mathrm{[S\,II]}}/10^{36})) = 0.14$.

Blair & Long (2004) have given 296 SNRs in M83. Leonidaki, Boumis, & Zezas (2013), in a survey of 6 galaxies presented 149 photometric SNRs in NGC 2403, 92 in NGC 4214, 70 in NGC 4449, 47 in NGC 4395, 36 in NGC 5204 and 24 in NGC 3077. The most recent work on NGC 6946, gave 147 photometric SNRs (Long, Winkler, & Blair 2019). The number of detected SNRs depends on various characteristics of a galaxy (e.g. star formation rate; SFR etc.) but also on the sensitivity of the observations and the distance of the galaxy.

3.6.2 Multi - wavelength comparison

In NGC 45, we find that none of the optically detected SNRs has any counterpart in radio or X-ray wavelengths (Pannuti et al. 2015). In NGC 55, only source 1 from the possible candidate SNRs has also emission in X-rays (source 131 in Binder et al. 2015, or source 85 in Stobbart, Roberts, & Warwick 2006). The fact that in the optical band we detect only 1 source out of the 18 X-ray SNRs, is probably an age effect. The blast waves of very young SNRs heat the material behind the shock front to very high temperatures ($\sim 10^7$ K) producing thermal X-rays (e.g. Leonidaki, Zezas, & Boumis 2010; Maggi et al. 2016; Ramakrishnan & Dwarkadas 2020). Most SNRs that produce X-ray emission are in the phase of free expansion or in the early adiabatic phase (e.g. Vink 2012) where we do not expect strong optical emission. Moreover, the SNR J001514-391246 in O'Brien et al. (2013), which emits in radio and X-rays, presents a shell-like structure (~ 44 pc) in our Hα image. Such SNRs would not be detected efficiently in our survey, which focuses on point-like sources. However, we find that this specific SNR does not show strong [S II] emission indicating that it could be embedded in H II region.

In NGC 1313, we do not detect any of the young X-ray emitting SNRs reported in Colbert et al. (1995). We see strong Hα emission at the position of SN 1978K which emits in the X-rays (Colbert et al. 1995; Petre et al. 1994; Schlegel, Petre, & Colbert 1996; Smith et al. 2007) and in radio (Achterberg & Ball 1994), but its low [S II] emission indicates that the shock may have not excited enough material to make it visible as an optical SNR.

In NGC 7793, the larger structure 6 and the candidate SNR 22 coincide with radio SNRs (Pannuti et al. 2002), and the structure 6 coincides also with X-ray SNR (Pannuti et al. 2011). Since in the latter case, the X-ray emission is associated with a larger region, the X-ray emission may come from super-bubbles with several shock-excited regions. This is supported by the size of this region ($\sim$ 320 pc; source 6 in Table 3.4 and Figure 3.5), which places it in the regime of super-bubbles.

3.6.3 The Hα Luminosity Function of SNRs

In Figure 3.12, we compare the Hα luminosity distribution of our candidate SNRs (black solid line) and the possible candidate SNRs (black dashed line), with the spectroscopic SNR population in the study of Leonidaki, Boumis, & Zezas (2013; NGC 2403, NGC 4212, NGC 3077, NGC 4395, NGC 4449, NGC 5204), and photometric SNRs in the studies of Matonick & Fesen (1997; NGC 5585, NGC 6946, M81, M101), Lee & Lee (2014a; M31) and Lee & Lee (2014b; M33).

Our candidate SNRs, which is the more secure sample of the two, seem to more closely follow the distribution of the spectroscopic SNRs of Leonidaki, Boumis, & Zezas while the distribution of the possible candidate SNRs agree with the distribution of the photometric SNRs of the other studies. This is expected since our sample of candidate SNRs consists of brighter objects (since they have higher signal to noise ratio in the [S II]/Hα ratio), and by necessity, spectroscopic surveys also target brighter objects.

In general, the distribution of the Hα luminosity of our candidate SNRs appear to be flatter compared to the other studies. This is the result of the strict selection criterion, [S II]/Hα ratio to be 3σ above the 0.4 threshold. Indeed, we see that the less accurate sample ([S II]/Hα ratio 2σ above the 0.4 threshold; black dashed line), agrees more with the other studies.

What distinguishes our work from the previous efforts is that: (a) we account for the effects of incompleteness, which allows us to study more accurately the faint end of their distribution and (b) we provide a quantitative description of the LFs, which can be used for comparison between different samples and theoretical models for the population of SNRs in different environments.

In Figure 3.7, we see the incompleteness-corrected luminosity distribution (gray histogram) and the best fit function (blue line) along with the initial, uncorrected data (black-line histogram). We see that apart from the different amplitudes, the mean value of a function that would describe the incompleteness uncorrected data would be shifted to the higher luminosities (since the incompleteness correction affects less the brighter sources) and the skewness would be different.

The skewness at the faint end of the LFs is due to incompleteness. In principle, the limited sensitivity of our survey and the selection of SNRs based on the [S II]/Hα criterion may prevent us from observing the peak of the Hα LF of the overall SNR population, even for the nearest galaxies. In order to compare our results with the published photometric SNR samples, which do not impose any threshold on the significance of the [S II]/Hα ratio, we use our less secure sample ($> 2\sigma$), and we compare it

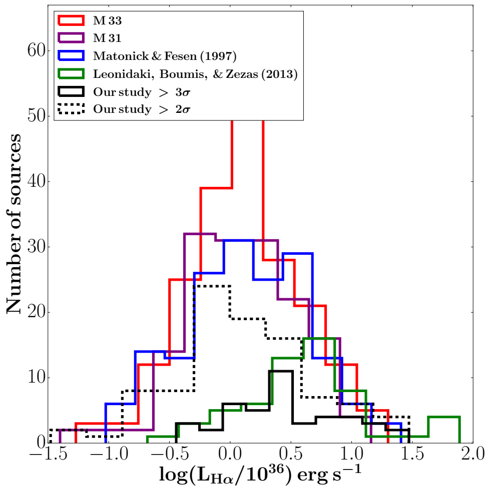

Figure 3.12: Comparison of the Hα luminosity distribution of our candidate SNRs (black solid line), our possible candidate SNRs (black dashed line) and the studies of spectroscopic SNRs from Leonidaki, Boumis, & Zezas 2013 (green line), and photometric SNRs from Matonick & Fesen 1997 (blue line), M31 (Lee & Lee 2014a; purple line), and M33 (Lee & Lee 2014b; red line).

with the luminosity distribution of SNRs in the Local Group M31 and M33 galaxies. We see (Figure 3.12) that both show a peak at $L_{H\alpha} \sim 10^{36}\,\mathrm{erg\,s^{-1}}$.

Taking into account the fact that the two surveys have similar flux sensitivity limits, while our objects lie at much larger distances, this strongly suggests that the peak in the Hα LF of SNRs, selected on the basis of the [S II]/Hα criterion (at signal to noise ratio > 2 sigma resulting in small contamination by H II regions), is $\sim 10^{36}\,\mathrm{erg\,s^{-1}}$ as measured from our quantitative analysis (Table 3.5). Focus on results, e.g. by integrating the LF, we find that we are missing ∼ 30% of the SNR population down to our detection limit.

Vučetić et al. (2015) following a similar approach for calculating the overall population of SNRs, by integrating a Gaussian distribution fitted to the bright-end of the Hα luminosity distribution of the photometric SNR populations in nearby galaxies. However this approach does not account for the effects of incompleteness which may impact even the higher luminosity objects.

Since SNRs depict the end-point of massive-stars life, they can be used as star formation rate (SFR) indicators. However, because of selection effects and incompleteness biases it cannot be used directly to derive the relation between SNRs and SFR, unless we correct for the incompleteness. The approach we have used in this work, can be used also to calculate a more reliable relation between the number of SNRs and SFR.

3.6.4 The bivariate LF and the degree of excitation

Observationally, because of the weakness of the [S II]$\lambda\lambda 6717, 6731$Å lines, the [S II]/H$\alpha$ criterion generally poses a higher threshold in the SNR luminosity than the sensitivity of the Hα data. In fact, the [S II]/Hα selection could be the main source of the skewness observed in the Hα LF (Figure 3.7). Similarly, this selection also results in the skewness observed in the ([S II]-Hα) bivariate LF along the main axis ([S II]/Hα; Figure 3.9). The truncation observed along the perpendicular (excitation) axis (Figure 3.11) is the result of the sharp [S II]/H$\alpha > 0.4$ threshold.

Regarding the excitation function, as we see in Figure 3.8, there is a trend for sources with higher Hα luminosities to have increasingly lower [S II]/Hα ratios (i.e. lower excitation) as is indicated by the sub-linear ($\alpha = -0.09$) slope of the $\log(L_{[\mathrm{S\,II}]}) - \log(L_{\mathrm{H}\alpha})$ relation in Figure 3.10. This effect would indicate that more luminous objects have lower excitation, which is counter-intuitive since these are expected to be the younger SNRs, and hence the ones with faster shocks and higher excitation. On the other hand, it is more likely that this is an observational effect: luminous SNRs are more likely to be in regions with high ISM density and possibly embedded in H II regions (e.g. Arbutina & Urošević 2005). Indeed, this is a trend that we see in Figure 3.6, where more luminous SNRs are located in regions with higher backgrounds. We note that this cannot be a selection bias, since brighter objects should be detectable in lower backgrounds as well. This is also one of the reasons (along with the incompleteness due to the [S II] and the strict selection criterion for the [S II]/Hα at 3σ), that the completeness is not 100% even for the brighter sources, while is low at the faint end of the Hα LF (Figure 3.7), where the sources are found in lower background regions. The contamination by the underlying emission from the H II regions would result in higher Hα luminosities but disproportionally lower [S II] luminosities due to the lower [S II]/Hα ratios of the H II regions.

At first glance this may sound at odds with our expectations that more luminous SNRs are expected to energise more efficiently their surrounding medium. However, this could also be a result of the [S II]/Hα selection criterion which biases against lower excitation objects. Only including a more complete population of objects (e.g. based also on the [O I]/Hα criterion e.g. Kopsacheili, Zezas, & Leonidaki 2020; Fesen, Blair, & Kirshner 1985) we may draw more robust conclusions on the excitation function and the degree of energization of the local ISM.

In Figure 3.13, we compare the distribution of the [S II]/Hα ratios of the candidate SNRs (black solid line) and the possible candidate SNRs (black dashed line) detected

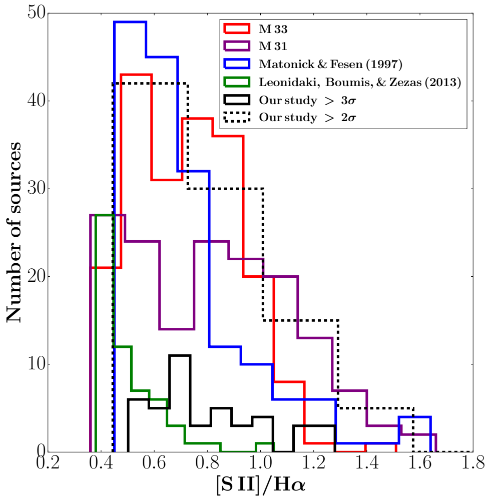

Figure 3.13: Histograms of the distribution of the [S II]/Hα ratios for the SNRs in our sample (black solid line for the candidate SNRs; black dashed line for the total sample, i.e. the candidate and the possible candidate SNRs), Leonidaki, Boumis, & Zezas (2013; green line), Matonick & Fesen (1997; blue line), M31 (Lee & Lee 2014a; purple line), and M33 (Lee & Lee 2014b; red line).

in our survey and those reported in the surveys of Leonidaki, Boumis, & Zezas (2013), Matonick & Fesen (1997), and Lee & Lee (2014a,b), aiming to examine the SNR excitation between different galaxies. The range of the [S II]/Hα values of our possible candidate SNRs is more similar to the values of the SNRs of the other surveys, although the distributions are not the same, while the [S II]/Hα ratios of our candidate SNRs is quite different.

The difference, between our sample and the other studies in the faint, end has to do with the different adopted [S II]/Hα ratio to identify SNRs (for our possible candidate SNRs), and with the fact that our selection criterion in the [S II]/Hα ratio (3σ above 0.4) is satisfied only for sources with high [S II]/Hα ratios (for our candidate SNRs). The general difference in the [S II]/Hα ratio distributions, between our possible candidate SNRs and the other surveys (that do not impose any threshold at the significance level of the [S II]/Hα ratio), may have to do with the different ISM conditions of the galaxies, but also with the different sensitivity between the studies. This emphasises the need for incompleteness corrections also in the [S II]/Hα ratio distributions.

3.6.5 The effect of [S II]/H$\alpha > 0.4$ criterion

Correcting our data for incompleteness, gives us the possibility to recover a number of SNRs that we did not detect (due to their faintness, their galactic environment etc.) down to our faintest detection limit. However, there is a number of SNRs that we do not detect due to selection criteria: for example, the [S II]/H$\alpha > 0.4$ criterion which is biased against low velocity SNRs.

If the SNRs with [S II]/H$\alpha < 0.4$ follow the extension of the distribution that we derived from those with [S II]/H$\alpha > 0.4$, we can have an estimation of the fraction of SNRs that we miss because of the [S II]/Hα selection criterion. Then, the missing population is given by the extrapolation of the best-fit truncated Gaussian (Figure 3.11) to lower [S II]/Hα ratios, after removing the truncation term. Applying this method on the best fit truncated Gaussian to the excitation function of SNRs, we find that almost 47% of the overall SNR population is not accounted for, under the assumption that the distribution of [S II]/H$\alpha > 0.4$ extends to lower [S II]/Hα flux ratios.

However, the [S II]/H$\alpha > 0.4$ criterion is an empirical diagnostic that comes from studies of SNRs in the SMC and the LMC (Mathewson & Clarke 1973). As discussed in Kopsacheili, Zezas, & Leonidaki (2020), such a criterion may miss legitimate SNRs with relatively low shock velocities which result in lower [S II]/Hα ratios (Allen et al. 2008). Such low velocities are characteristic of older SNRs (e.g. Draine 2011) or they may reflect their local ISM conditions (e.g. SNRs expanding in dense environments lose quickly their momentum and they slow down faster; e.g. Jiménez, Tenorio-Tagle, & Silich 2019; Cioffi, McKee, & Bertschinger 1988). Therefore, in order to have a more reliable picture of the overall SNR population one would need to combine fast-shock sensitive (such as [S II]/Hα) with a slow-shock indicator (such as the [O I]/Hα; Kopsacheili, Zezas, & Leonidaki 2020; Fesen, Blair, & Kirshner 1985).

3.7 Appendix: Possible candidate SNRs

Table 3.7: Candidate SNRs

ID	RA (J2000) hh:mm:ss	Dec (J2000) dd:mm:ss	$F_{H\alpha} \pm \delta F_{H\alpha}$ ($10^{-16}\,\mathrm{erg\,s^{-1}\,cm^{-2}}$)	$F_{[SII]} \pm \delta F_{[SII]}$ ($10^{-16}\,\mathrm{erg\,s^{-1}\,cm^{-2}}$)	$\frac{F_{[SII]}}{F_{H\alpha}} \pm (\delta \frac{F_{[SII]}}{F_{H\alpha}})$
NGC 45 (2σ)					
1	00:14:02.3	-23:10:27.5	6.3 ± 0.54	4.21 ± 0.64	0.67 ± 0.10
2	00:14:12.4	-23:10:27.1	16.5 ± 0.4	7.31 ± 0.30	0.44 ± 0.02
3	00:14:09.8	-23:09:52.4	2.79 ± 0.22	1.85 ± 0.24	0.66 ± 0.10
NGC 55 (2σ)					
1	00:15:43.5	-39:16:41.3	7.48 ± 0.46	4.01 ± 0.4	0.54 ± 0.06
2	00:15:56.9	-39:15:45.3	1.84 ± 0.6	2.76 ± 0.45	1.5 ± 0.5
3	00:15:29.9	-39:14:15.0	2.8 ± 0.61	3.54 ± 0.7	1.3 ± 0.4
4	00:15:06.9	-39:12:24.4	3.45 ± 0.63	3.47 ± 0.64	1 ± 0.3
5	00:14:54.0	-39:11:51.5	11.4 ± 3.3	16.1 ± 2.3	1.4 ± 0.5
6	00:14:20.2	-39:10:09.0	1.3 ± 0.19	1.15 ± 0.22	0.88 ± 0.2
7	00:14:01.5	-39:10:21.0	3.15 ± 0.24	2.05 ± 0.29	0.65 ± 0.1
8	00:14:40.5	-39:08:53.6	3.13 ± 0.27	2.13 ± 0.34	0.68 ± 0.1
9	00:13:51.4	-39:08:46.7	0.702 ± 0.18	0.975 ± 0.2	1.4 ± 0.5
NGC 1313 (2σ)					
1	03:18:01.6	-66:31:30.5	0.87 ± 0.24	1.77 ± 0.3	2 ± 0.7
2	03:18:09.3	-66:31:12.4	3.19 ± 0.46	2.42 ± 0.35	0.76 ± 0.2
3	03:18:17.5	-66:30:20.4	5.53 ± 0.98	5.58 ± 1.1	1 ± 0.3
4	03:17:38.0	-66:30:01.5	6.81 ± 0.33	3.66 ± 0.32	0.54 ± 0.05
5	03:17:47.5	-66:29:48.5	12.9 ± 0.4	6.56 ± 0.43	0.51 ± 0.04
6	03:18:39.5	-66:29:12.1	13.6 ± 1.2	8.47 ± 0.95	0.62 ± 0.09
7	03:18:33.1	-66:28:50.0	7.22 ± 0.81	5.35 ± 0.66	0.74 ± 0.1
8	03:18:36.3	-66:27:58.6	4.03 ± 0.43	2.97 ± 0.38	0.74 ± 0.1
NGC 7793 (2σ)					
1	23:58:08.2	-32:36:41.2	4.3 ± 0.5	3.2 ± 0.34	0.74 ± 0.1
2	23:57:37.2	-32:36:32.1	3.6 ± 0.33	2.4 ± 0.36	0.67 ± 0.1
3	23:57:31.3	-32:34:50.9	1.5 ± 0.25	1.8 ± 0.32	1.2 ± 0.3
4	23:57:54.2	-32:37:17.3	4.1 ± 0.61	4.2 ± 0.83	1.0 ± 0.2

5	23:57:44.6	-32:37:03.4	7.4 ± 0.6	4.5 ± 0.62	0.61 ± 0.1
6	23:57:41.0	-32:36:54.9	5.5 ± 0.52	3.7 ± 0.54	0.66 ± 0.1
7	23:57:38.6	-32:34:49.1	1.1 ± 0.33	3.6 ± 0.45	3.3 ± 1.0
8	23:57:59.3	-32:34:37.3	4.4 ± 0.54	3.2 ± 0.59	0.74 ± 0.2
9	23:57:59.8	-32:34:26.4	7.8 ± 0.87	5.5 ± 0.59	0.71 ± 0.1
10	23:57:37.9	-32:33:53.2	3.1 ± 0.32	2.5 ± 0.48	0.79 ± 0.2
11	23:57:50.6	-32:33:13.8	4.5 ± 0.58	3.3 ± 0.52	0.73 ± 0.1
12	23:57:48.4	-32:36:42.8	3.9 ± 0.79	3.8 ± 0.76	0.96 ± 0.3
13	23:57:58.0	-32:36:37.7	6.1 ± 0.55	4.3 ± 0.66	0.7 ± 0.1
14	23:57:52.2	-32:36:15.5	11.0 ± 0.7	7.6 ± 1.1	0.69 ± 0.1
15	23:57:58.3	-32:36:08.3	9.0 ± 0.7	5.5 ± 0.73	0.61 ± 0.09
16	23:57:46.0	-32:36:06.1	5.1 ± 0.73	6.5 ± 1.2	1.3 ± 0.3
17	23:57:58.2	-32:36:02.1	2.4 ± 0.42	2.5 ± 0.57	1.0 ± 0.3
18	23:57:58.7	-32:35:56.4	2.2 ± 0.41	2.6 ± 0.44	1.2 ± 0.3
19	23:57:55.0	-32:35:51.3	2.1 ± 0.53	3.0 ± 0.61	1.5 ± 0.5
20	23:57:43.9	-32:35:33.1	2.3 ± 0.65	5.5 ± 0.71	2.4 ± 0.7
21	23:57:44.2	-32:35:19.4	5.5 ± 0.81	4.5 ± 0.75	0.81 ± 0.2
22	23:58:00.4	-32:35:14.3	4.9 ± 0.44	3.3 ± 0.45	0.67 ± 0.1
23	23:57:44.1	-32:34:55.4	5.3 ± 0.86	4.7 ± 0.99	0.89 ± 0.2
24	23:57:50.1	-32:34:44.4	4.0 ± 0.57	4.5 ± 0.75	1.1 ± 0.2
25	23:57:58.4	-32:34:41.3	5.1 ± 0.42	3.3 ± 0.5	0.64 ± 0.1
26	23:57:41.0	-32:34:35.7	2.6 ± 0.38	2.5 ± 0.5	0.95 ± 0.2
27	23:57:51.0	-32:34:28.9	9.2 ± 0.63	6.6 ± 0.91	0.72 ± 0.1
28	23:57:54.2	-32:34:16.4	1.5 ± 0.31	1.8 ± 0.39	1.2 ± 0.4
29	23:57:54.7	-32:35:35.5	2.4 ± 0.66	3.3 ± 0.61	1.4 ± 0.4
30	23:57:58.9	-32:35:32.2	7.4 ± 0.71	5.4 ± 0.94	0.73 ± 0.1
31	23:57:47.2	-32:34:28.3	13.0 ± 1.6	8.2 ± 0.97	0.62 ± 0.1

3.8 Conclusions

In this work, we present the systematic study of optical SNR populations in 4 nearby spiral galaxies: NGC 45, NGC 55, NGC 1313, and NGC 7793. We identify 43 candidate and 54 possible candidate SNRs (84 of which are new identifications) detected at the 3σ level in deep Hα images and selected on the basis of their [S II]/Hα flux ratios (higher than 0.4 at the 3σ and 2σ level respectively) following a fully automated procedure.

Based on this sample, we calculate the Hα luminosity function and the joint Hα-[S II] luminosity function after accounting for incompleteness effects. The latter presents a new way to encode the luminosity and excitation of the SNR populations. We model the luminosity function with a skewed Gaussian distribution. We find that the Hα luminosity at the peak (mean) of the distribution of the overall sample (candidate and possible candidate SNRs) is $\sim 10^{36}\,\mathrm{erg\,s^{-1}}$. This is consistent with the peak of the Hα luminosity distribution in SNRs detected in the M31 and M33 spiral galaxies for the same quality of data (also less accurate sample).

We also find that SNRs with higher Hα luminosity, tend to have lower excitation (i.e. lower [S II]/Hα ratio), although this could be an environmental effect. This is something that can be seen directly by our data, where brighter sources are located in regions with higher backgrounds. The excitation function of the overall SNR population is modeled by a truncated Gaussian with the truncation accounting for the [S II]/Hα selection effect. We find that the width of the Gaussian is 0.11 in terms of distance (from the line $\mathrm{y} = -0.09\mathrm{x} + 0.26$).

3.9 Acknowledgements

We acknowledge funding from the European Research Council under the European Union's Seventh Framework Programme (FP/2007-2013)/ERC Grant Agreement n. 617001. This project has received funding from the European Union's Horizon 2020 research and innovation programme under the Marie Sklodowska-Curie RISE action, grant agreement No 691164 (ASTROSTAT). We also acknowledge support from the European Research Council under the European Union's Horizon 2020 research and innovation program, under grant agreement No 771282. The observations made at Cerro Tololo Inter-American Observatory at NSF's NOIRLab (NOIRLab Prop. ID: 2011B-0550; PI: A. Zezas), which is managed by the Association of Universities for Research in Astronomy (AURA) under a cooperative agreement with the National Science Foundation. IL acknowledges support by Greece and the European Union (European Social Fund - ESF) through the Operational Programme "Human Resources Development, Education and Lifelong Learning" in the context of the project "Reinforcement of Postodoctoral Researchers-2nd Cycle" (MIS-5033021), implemented by the State Scholarships Foundation (IKY).

Data availability

The data underlying this article are available in the article and in its online supplementary material. The raw data are available from the NOAO data archives.

4

Models for populations of Supernova Remnants

4.1 Introduction

Supernova Remnants (SNRs) play significant role in shaping the interstellar medium (ISM). They enrich the ISM with heavy elements and they provide large amounts of mechanical energy to the ISM which in turn, can play significant role in the evolution of the host galaxy. The propagating shock wave, compresses the ISM and under appropriate conditions it can trigger star formation. Moreover, since core-collapse SNRs trace the last stage of a massive stars' life, they trace the on-going massive star formation rate.

Study of SNR populations and their physical properties is very important in order to understand their feedback to the ISM and their role in the host galaxy. Systematic studies of Galactic SNRs provide more detailed information about the physical parameters of SNRs and their interaction with their surrounding ISM (Williams et al. 2020; Milisavljevic & Fesen 2013; Boumis et al. 2009; Fesen, Blair, & Kirshner 1985). On the other hand, the study of extra-galactic SNRs, give us the opportunity to examine larger samples of SNRs, in different environments (i.e. different metallicities; (Long, Winkler, & Blair 2019; Leonidaki, Boumis, & Zezas 2013; Matonick et al. 1997; Blair & Long 1997)). This is the only way to understand their evolution and their feedback to the ISM in conditions representing typical galactic environments.

Despite the increasing number of SNRs and SNR populations, we still lack a framework that can describe the SNR populations in terms of their observational characteristics but also in the context of expectations from theoretical models for their evolution. A first step in this direction was made in Kopsacheili et al. 2021, who developed a method for the calculation of luminosity functions of SNRs, free of selection effects, and introduced the joint Hα - [S II] luminosity function (LF), as well as, their excitation function. While the Hα LF provides information on their overall population and energetics, the joint Hα - [S II] LF and the excitation function, reflect their interaction with the ISM. The latter in particular, bears the imprint of the shock velocity distribution of the SNRs, in their optical emitting phase. However, what is missing, is a theoretical framework that can predict the different metrics of SNR populations based on models for their evolution.

In this work, we present a basic population synthesis model for SNRs. We develop a toy model, based on the shock models of Allen et al. 2008, in order to construct the Hα and Hα - [S II] luminosity functions (LFs) and examine their dependence on different parameters, such as pre-shock density, shock velocity, and magnetic field. This work is the first step for construction of population synthesis models of optical SNRs.

In § 4.2 we describe the models that we used and the analysis that we followed for the calculation of luminosity functions. In § 4.3 we present the theoretical Hα and the joint [S II] - Hα derived from this analysis and in § 4.4 we discuss our results. In § 4.5 we summarize our results.

4.2 Population models

Our goal is to calculate the Hα and the joint Hα - [S II] luminosity functions for a theoretical population of SNRs. We assume that SNRs are in the adiabatic (Sedov-Taylor) phase, for which we have an analytic expression for the time evolution of their radius and shock velocity, as a function of their age, pre-shock density, and initial energy. These are given by the Sedov-Taylor relations (Draine 2011):

$$R(n,t) = 1.54 \times 10^{19}\, cm\, E_{51}^{1/5} n_0^{-1/5} (t/10^3)^{2/5} \tag{4.1}$$

$$v(n,t) = 1950\, km\, s^{-1} E_{51}^{1/5} n_0^{-1/5} (t/10^3)^{-3/5} \Rightarrow \tag{4.2}$$

$$t(v,n) = 10^3\, s\, (\frac{v \cdot n^{1/5}}{1950})^{-5/3} \tag{4.3}$$

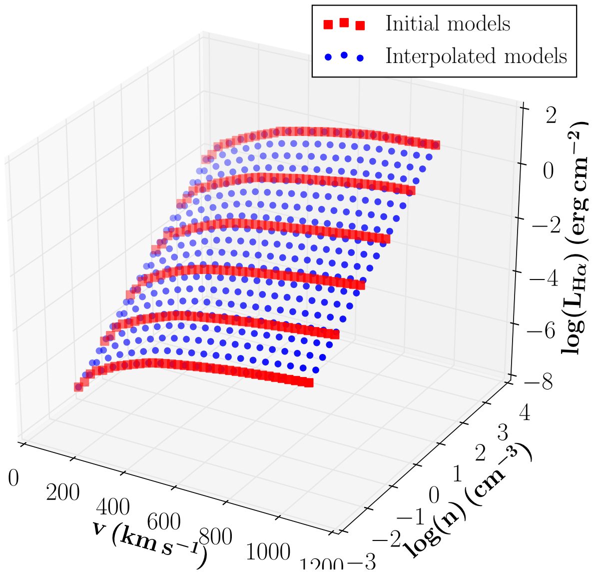

Figure 4.1: Here we present the initial models of Allen et al. 2008 (indicatively we present the $u - n - L_{H\alpha}$ space; blue squares), and the interpolated models (red circles).

where n is the ambient ISM density (cm^{-3}), v the shock velocity in ($\mathrm{km\,s}^{-1}$), E_{51} the kinetic energy of the mass ejected by the SN explosion in units of 10^{51} erg. The age t is calculated by solving the equation of the velocity.

The luminosity of an SNR is given by the luminosity per unit area calculated from the shock models and their surface:

$$L = 4\pi R^2 L_s(v, B, n) \tag{4.4}$$

where $L_s(v, B, n)$ is the luminosity per unit area, provided by the shock models for a given magnetic field B, ambient density n and shock velocity v. In order to calculate the radius R, we use the eq. (4.1)

In order to construct theoretical luminosity functions, we used the shock models of Allen et al. 2008. These models predict the luminosity of different emission lines for shocks with velocities v = 100 to 1000 $\mathrm{km\,s}^{-1}$, expanding in media with densities n = 0.01 to 1000 cm^{-3}, and magnetic parameters $\mu = 10^{-4}$ to $10\mu\,\mathrm{G\,cm}^{3/2}$. Although there are available models for sub-solar, solar, and super-solar abundances, in this work we focus on solar abundance models, which are calculated for the widest range of pre-shock densities ($\mathrm{n} = 0.01 - 1000\,\mathrm{cm}^{-3}$).

4.2.1 Calculation of luminosity functions

Our first goal is to calculate the theoretical Hα luminosity function (LF$_{\mathrm{H}\alpha}$). The LF can be considered as a probability distribution. In this case, the LF has the form:

$$P(L) = \int\int P(L|n,v)\,P(v|n,t)\,P(n)\,P(t)\,dndt \tag{4.5}$$

where $P(L|n,v)$ is the probability to obtain a specific luminosity L from a given density n and shock velocity v, $P(v|n,t)$ is the probability to obtain a specific shock velocity, which under the Sedov-Taylor model, depends on the ISM density and the SNR age (eq. 4.2), and $P(n)$ and $P(t)$ are the probability distributions of density and age respectively.

In order to work on a denser parameter grid than the one provided in Allen et al. 2008, for each category of models (based on B), we use linear interpolation between the densities and velocities of the original set, to calculate the Hα and [S II] luminosities. In Figure 4.1 we present the interpolated models (blue circles), in a finer grid of shock velocity and density. In order to calculate the Hα and [S II] luminosities, we use the eq. (4.4).

The calculation of the probabilities of each model is presented below:

- $P(L|n,v)$
  The luminosity of a shock as a function of their velocity and ISM density is adopted from the models of Allen et al. (2008; Figure 4.1). The dependence of the shock velocity on ISM density and age is given by eq. (4.2)

- $P(v|n,t)$
  The probability distribution of the shock velocity, as a function of the density n and age t (eq. 4.2).

- $P(n)$
  We consider a log-normal ISM distribution with $\mu = log(n/cm^3) = 1\,cm^{-3}$ and $\sigma = 10^{1.5}\,cm^{-3}$:

$$P(log(n)) = \frac{1}{\sigma\sqrt{2\pi}} e^{-(log(n)-\mu)^2/(2\sigma^2)} \tag{4.6}$$

- $\underline{P(t)}$
  For the age of the SNRs we consider a uniform distribution, between $t = 1000$ and $t = 30000\,$years
$$P(t) = constant \tag{4.7}$$

Magnetic fields also play an important role in the emerging luminosity from a shock front (Allen et al. 2008). Since we do not have any information on the distribution of the magnetic fields in SNRs, we perform our analysis for eight different magnetic-field ranges: i) $10^{-6} - 10^{-3}$; ii) $10^{-3} - 10^{-2}$; iii) $10^{-2} - 0.1$; iv) $0.1 - 1$; v) $1 - 10$; vi) $10 - 100$; vii) $100 - 1000\,\mu\,$G; viii) $1000 - 10^4\,\mu\,$G. This way we can assess the effect of the magnetic field on the resulting luminosity function.

In order to compare these models with observational samples of SNRs, we have to apply the same selection criteria, as the ones that were used in the observational studies. The most typical criterion for the identification of SNRs is their [S II] /H$\alpha > 0.4$ ratio (Mathewson & Clarke 1973). Although this can bias the SNR samples against slower velocity or older SNRs (Kopsacheili, Zezas, & Leonidaki 2020), most SNR samples have been selected on this basis, so in the following analysis we only consider systems with [S II] /Hα luminosity ratios greater than 0.4.

4.3 Results

4.3.1 Hα luminosity function

In Figure 4.2 we show indicatively the Hα LFs, for magnetic fields from 0.1 to 1000 μG . As we see, they can be described by a skewed Gaussian the form of which is:

$$f(log(L)) = \frac{A}{\sigma\sqrt{(2\pi)}} e^{\frac{-(log(L)-\mu)^2}{2\sigma^2}} \{1 + erf[\frac{\alpha(log(L)-\mu)}{\sigma\sqrt{2}}]\} \tag{4.8}$$

where μ, σ, and α, are the mean values, the sigma value and the skewness respectively.

However, the peak of the LF is for luminosities up to 2 order of magnitudes higher than the expected ones. This happens because in the calculation of the luminosities, we assumed a filling factor $f = 1$ for the SNRs. Although it is difficult to measure directly the filling factor, especially for the extragalactic SNRs, simulations give values from 3% to 23% (e.g. Slavin et al. 2017). Indeed we find that we can match the observed and model LFs by shifting the latter to lower luminosities by 0.65 to 2.06 dex depending on the model (Table 4.1). These correspond to filling factors of 22.3% and 9% respectively, in excellent agreement with the aforementioned simulations. We note that since we are

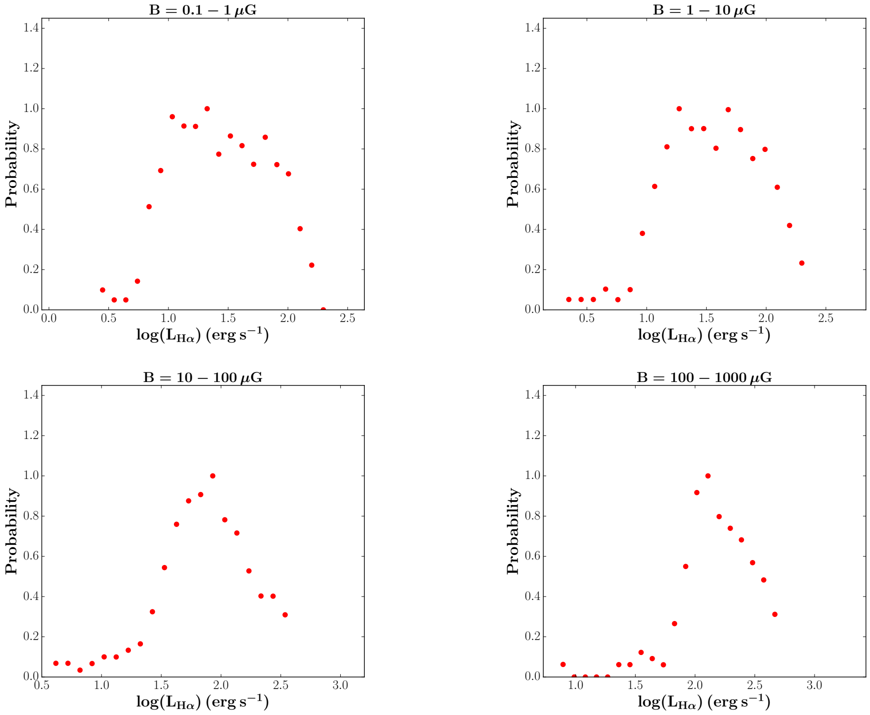

Figure 4.2: The model Hα luminosity function for magnetic fields between 0.1 and 1000 μG. The luminosity is in units 10^{36} erg s^{-1}

interested in a qualitative comparison of the model and observed LFs, the exact value of the shift is not important.

The results of the shifted Hα LF are presented in Figure 4.3 (red points). The different panels give the resulting Hα luminosity functions for the different regimes of magnetic fields.

In order to obtain the best fit parameters of the skewed Gaussian, we apply a least squares method. In Table 4.1 we present these parameters for the different magnetic fields. At first glance, we see no specific correlation between the intensity of magnetic field and the shape of the Hα LF. The best fit model is shown by the red line Figure 4.3.

4.3.2 Joint [S II] - Hα Luminosity Function

The joint [S II] - Hα luminosity function, is presented as probability distribution on the Hα - [S II] plane, in figures 4.4 and 4.5. The grayscale corresponds to the probability for each model to have a particular combination of Hα and [S II] luminosity, given the physical parameters of the shock. Darker gray colors mean higher probabilities. Again, different panels correspond to different regimes of magnetic fields. The circles in figures 4.4 and 4.5, show the models on the [S II] - Hα plane. The color of these circles indicate

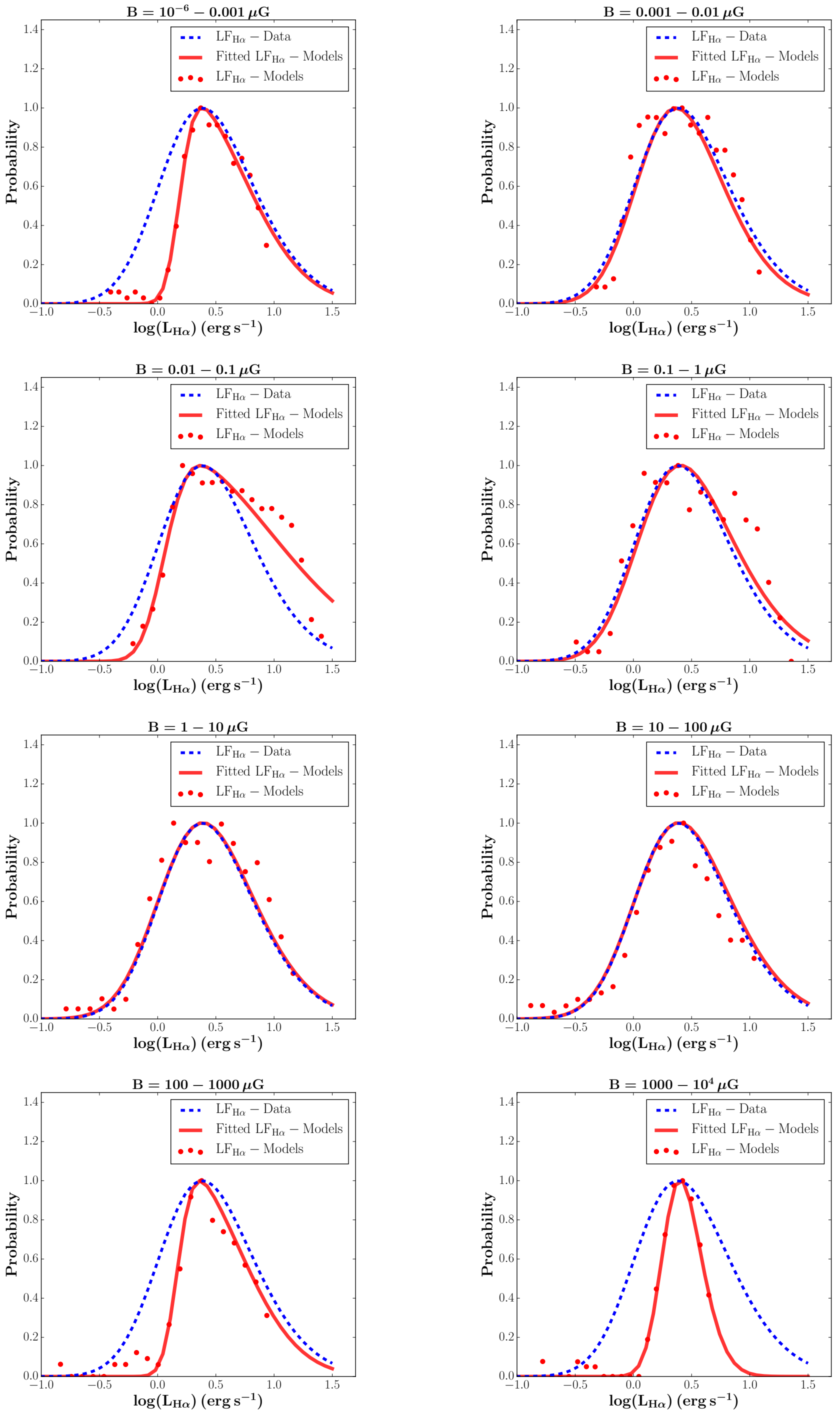

Figure 4.3: The model Hα luminosity function (red points) for different magnetic field ranges. The red line shows the best-fit skewed Gaussian to the model points, and the blue dashed line shows the Hα luminosity function of SNRs of nearby galaxies from the work of Kopsacheili et al. 2021. The luminosity is in units 10^{36} erg s^{-1}

.

Table 4.1: Hα Luminosity functions

B*(μG)	Shift	μ	σ	α
$10^{-6} - 10^{-3}$	-0.65	0.19	0.54	5.38
$10^{-3} - 0.01$	-0.94	0.07	0.55	5.66
$0.01 - 0.1$	-0.84	0.06	0.91	5.75
$0.1 - 1$	-0.94	0.07	0.64	2.08
$1 - 10$	-1.14	0.07	0.59	1.65
$10 - 100$	-1.50	0.07	0.60	1.72
$100 - 1000$	-1.73	0.17	0.52	5.07
$1000 - 10^4$	-2.06	0.27	0.24	1.68

Col (1): The magnetic-field range; col (2): The shift of the theoretical Hα LF in units of log(L/10^{36}) erg s^{-1}; col (3): The mean of the skewed Gaussian after the shift in units of log(L/10^{36}) erg s^{-1}; col (4): The sigma of the skewed Gaussian in units of log(L/10^{36}) erg s^{-1}; col (5): The skeweness of the skewed Gaussian.

the pre-shock density (in logarithmic scale), while the size, the pre-shock velocity. The distribution of these points on the [S II] - Hα plane provide information on the contribution of SNRs of different physical conditions in different regions of the [S II] - Hα plane.

4.4 Discussion

In this work, we presented a first attempt in building a population synthesis models for the luminosity distribution of SNRs. Based on these models and assumptions on the density, magnetic field, and age distribution of SNR populations, we can predict the luminosity distribution of SNRs in different spectral lines. Next we discuss the qualitative comparison of these models, with the observed Hα and (Hα, [S II]) luminosity distribution of SNRs.

4.4.1 Luminosity Functions - Comparison with data

In Figure 4.3, we present the theoretical Hα LF, derived for the shock models (red color) for the different magnetic fields. The blue dashed line is the Hα luminosity function derived from SNRs of nearby galaxies (Kopsacheili et al. 2021) where we have corrected

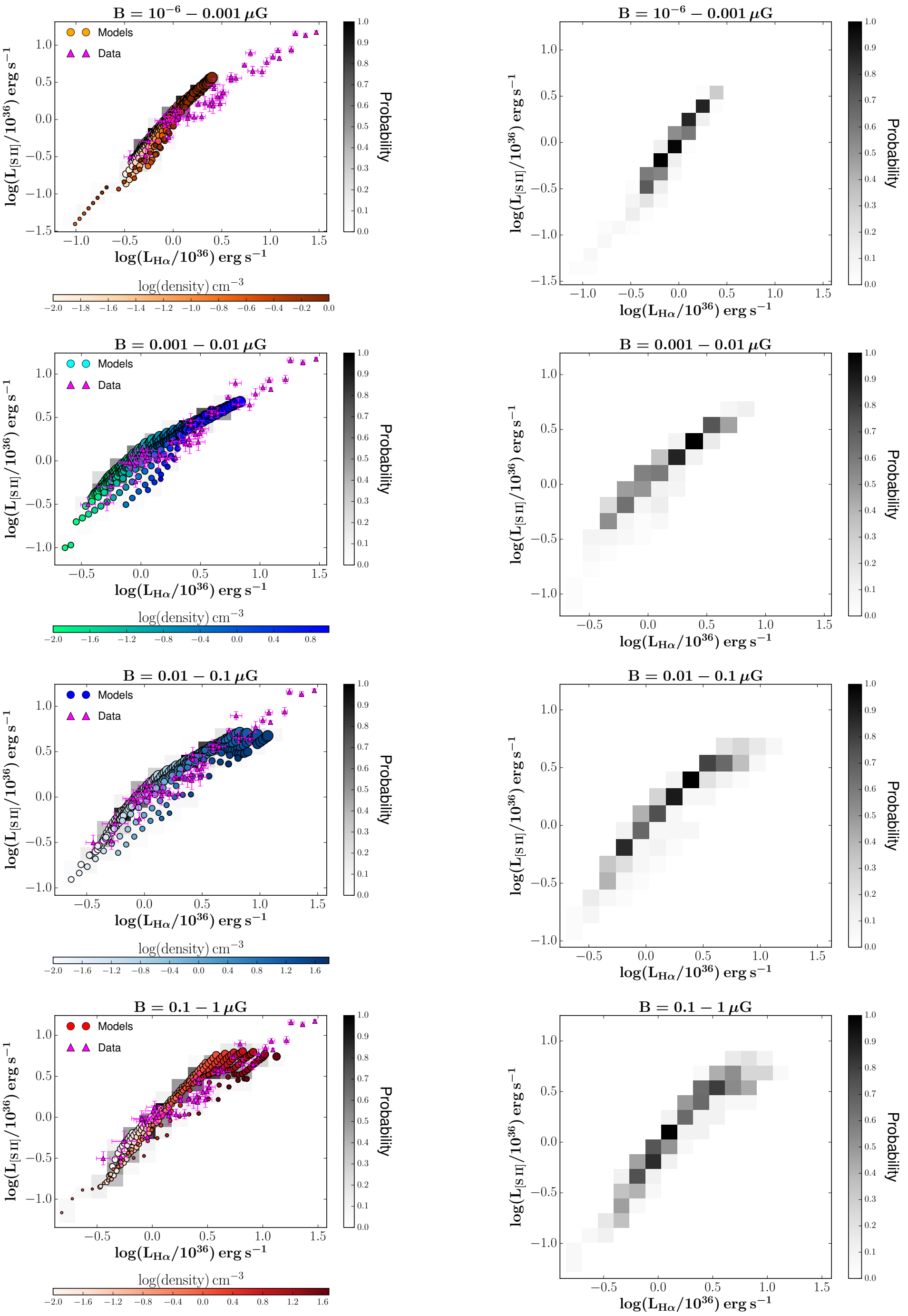

Figure 4.4: The joint [S II] - Hα luminosity function shown as probability distribution (gray colorbar; right column) for the magnetic fields between 10^{-6} and $1\,\mu G$. Darker colour indicates higher probability. Different rows of panels correspond to different magnetic field ranges. The circles show the distribution of the models on the Hα -[S II] plane (left column). Their colorbars indicate their density and their size the velocity. The magenta triangles are the candidate SNRs in nearby galaxies from the work of Kopsacheili et al. 2021

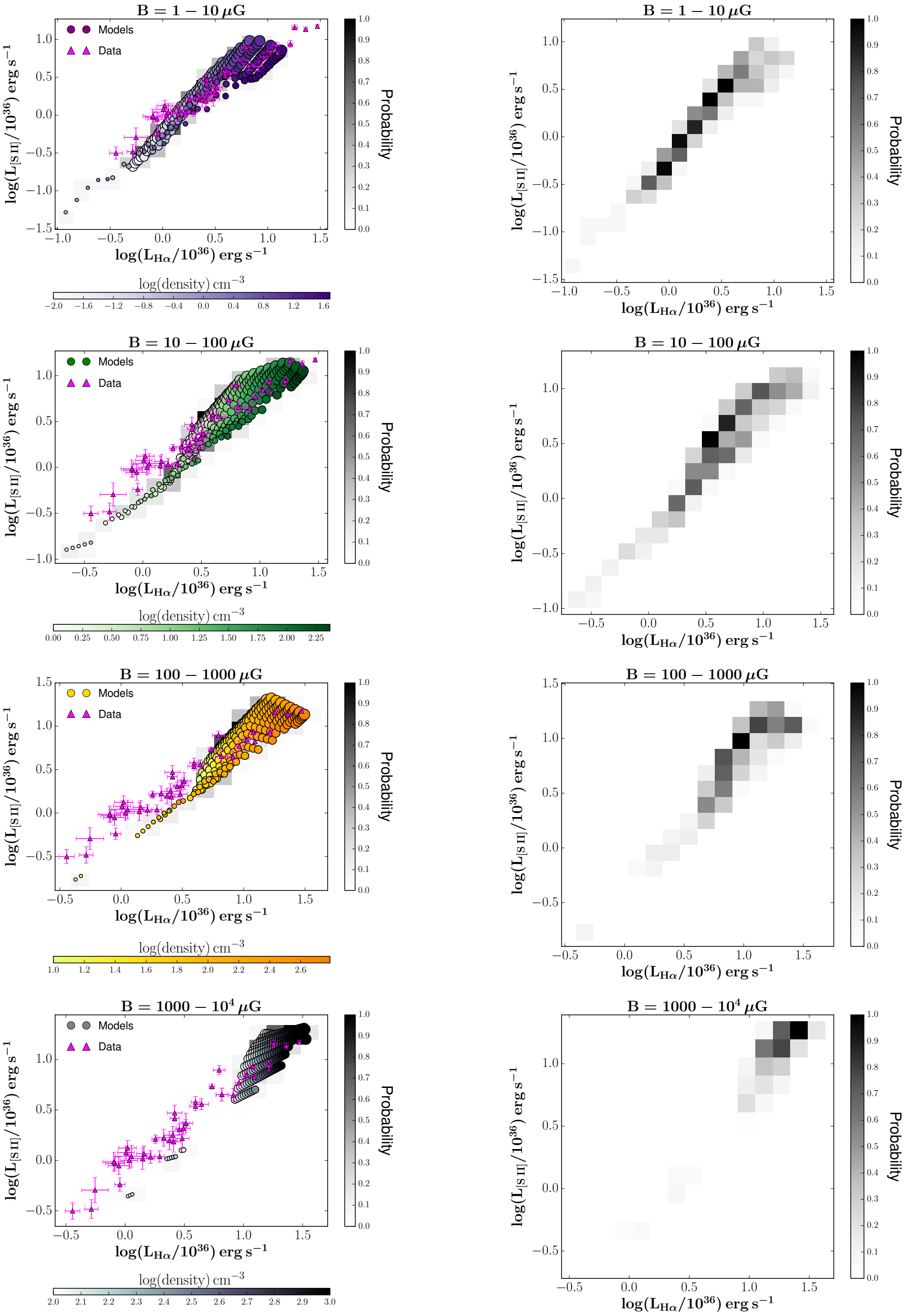

Figure 4.5: The joint [S II] - Hα luminosity function shown as probability distribution (gray colorbar; right column) for the magnetic fields between 1 and 10^4 μG. Darker colour indicates higher probability. Different rows of panels correspond to different magnetic field ranges. The circles show the distribution of the models on the Hα -[S II] plane (left column). Their colorbars indicate their density and their size the velocity. The magenta triangles are the candidate SNRs in nearby galaxies from the work of Kopsacheili et al. 2021

for incompleteness, making the sample free of selection effects.

By comparing the observational and the model LFs (Figure 4.3; comparison between red and blue dashed lines), we see that the models that present agreement with the observational Hα LF are those with magnetic fields $0.001 - 0.01\,\mu$G, $0.1 - 1\,\mu$G, $1 - 10\,\mu$G, and $10-100\,\mu$G, with the magnetic fields between $1-10\,\mu$G to almost completely match the observational Hα LF. Magnetic fields between $1-10\,\mu$G are expected for older SNRs, as the SNRs of the study of Kopsacheili et al. 2021 (e.g. Raymond et al. 2020 predict for the mature SNR Cygnus Loop a magnetic field $\mathrm{B} = 4\,\mu$G).

In the figures 4.4 and 4.5 we present the probability maps for the 2D ([S II] - Hα) LF for the different magnetic fields. The magenta triangles are the candidate SNRs from the study of Kopsacheili et al. 2021. In order to compare them with models, they must be free of selection effects. The incompleteness correction (that makes the sample free of selection effects) cannot be applied on the scatter plot of the candidate SNRs in the figures 4.4 and 4.5. Instead, we can calculate a model of the Hα - [S II] LF that we would observe under the same incompleteness conditions. Therefore, on each (Hα - [S II]) bin we apply the incompleteness function in order to calculate the probability distribution for the SNR populations expected to be observed under our model.

It is clear from the figures 4.4 and 4.5 that the observed ($\mathrm{L}_{\mathrm{H}\alpha}$, $\mathrm{L}_{[\mathrm{S\,II}]}$) distribution cannot be described by a single model. Models with high magnetic fields dominate in the upper right part of the diagram (high luminosities), while low magnetic fields result in lower luminosities. Therefore, in order to reproduce the full distribution of observed luminosities, we have to consider multiple magnetic fields, as expected.

4.4.2 Effect of density distribution

The SNR luminosity is highly sensitive to the density (n) of the medium in which it is expanding. Thus, we expect to have higher luminosity SNRs in regions with higher pre-shock densities. This behavior is predicted by models (Arbutina & Urošević 2005), but also it is seen in observational data, where there is a lack of bright SNRs in regions with low Hα background indicating low density environments (Kopsacheili et al. 2021). The same behaviour is observed in our models. For higher magnetic-field regimes, higher pre-shock densities result in higher luminosities.

4.4.3 Effect of velocity distribution

As the SNR evolves, more material accumulates behind the shock decreasing its velocity (e.g. Reynolds 2017). With the deceleration of the shock, the shock excitation also decreases resulting in lower luminosities. Hence, we expect that higher luminosity SNRs are associated with higher shock velocities, which agrees with the model predictions. In the figures 4.4and 4.5 we see that the shock velocities are higher for higher luminosities (larger circles mean higher velocities).

4.4.4 Magnetic Field

The pre-shock magnetic field can affect the properties of the shock. The typical values of the compressed interstellar magnetic field are $\sim 20\mu$G (i.e. 4 times the pre-shock magnetic field; Ballet 2006; Vink & Laming 2003). However, for young SNRs values higher than 100 μG have been measured (e.g. Vink 2017), indicating magnetic-field amplification near the shock. In general, we expect that SNRs with higher shock velocities and pre-shock densities, are correlated with stronger magnetic fields (Vink 2020).

Our models agree with these predictions. The circles in fig. 4.4 and 4.5 show the distribution of the models on the Hα- [S II] plane, with each panel showing different regimes of magnetic fields. As we see, this distribution becomes steeper for stronger magnetic fields. For magnetic fields > 100 μG there is a deficit of models in the region of low luminosities, and the probability of the few models there, is very low, as indicated by the light grey color of the probability maps.

4.4.5 Implications and Limitations

These theoretical models give us a very useful tool for exploring the properties of SNRs in the context of their evolution. Although the model presented here can be considered as a "toy" model, it lays the foundation for a population synthesis model for SNR populations. Such a model can be used to explore the effect of different underlying distributions for physical parameters, such as density, shock velocity, and magnetic field, on the observed luminosity distributions. When appropriate observational data are available, one could use these models to infer these distribution.

However, we recognize that there are limitations in the current state of models, that prevent us from making accurate calculations of the physical parameters. These limitations arise from several issues the most important of which are: i) we only consider the Sedov-Taylor phase, however we expect that a large fraction of the optical SNRs are in the radiative phase. For this reason, relations that describe the evolution of the physical parameters in the radiative phase should be included in our formalism; ii) The grid used to obtain the luminosity of SNRs as a function of their shock velocity, density and magnetic field, could be extended to a wider range of parameter values with a finer grid; iii) As is seen in figures 4.4 and 4.5, there is significant degeneracy of the observable parameters as a function of the SNR physical parameters: i.e. two SNRs with different shock velocity, density, and magnetic field may have the same Hα and [S II] luminosity. These degeneracies can be reduced to some degree by including in the models additional observable quantities (e.g. other spectral lines, or continuum bands). This will help using these models as a diagnostic tool for the underlying physical parameters and processes of the SNRs. Furthermore, by integrating over the physical parameters of the SNR population, we can estimate their integrated luminosity output in different bands or their total momentum/mechanical energy output.

4.5 Conclusions

In this work, we present for the first time theoretical models for the populations of supernova remnants. We use shock models, that give the luminosity of emission lines as a function of the physical parameters of the shock (shock velocity, pre-shock density and magnetic field). Considering the luminosity function as a probability distribution, we construct theoretical Hα and joint [S II] - Hα luminosity functions. We find remarkable agreement between the predicted LFs with the LFs of the observed SNR populations in nearby galaxies, after correcting the models for a filling factor. Also, remarkably the estimated filling factor agrees very well with that measured in observations of Galactic SNRs or estimated from detailed SNR simulations. This is the first step in developing a new generation of SNR population synthesis models.

Acknowledgements

We acknowledge funding from the European Research Council under the European Union’s Seventh Framework Programme (FP/2007-2013)/ERC Grant Agreement n. 617001. This project has received funding from the European Union’s Horizon 2020 research and innovation programme under the Marie Sklodowska-Curie RISE action, grant agreement No 691164 (ASTROSTAT). We also acknowledge support from the European Research Council under the European Union’s Horizon 2020 research and innovation program, under grant agreement No 771282. We would also like to thank Alexandros Chiotellis for the useful conversations.

5

Conclusions-Future Work

5.1 Conclusions

In this work, we present some new aspects on the study of SNR populations. These have to do with new, more efficient diagnostics for the identification of SNRs, identification of new SNR candidates in 4 nearby galaxies and the development of methods for the study of these populations, and the construction of theoretical models for populations of SNRs.

The first study focuses on the examination of new diagnostics for the optical identification of SNRs. The most common diagnostic so far is the [S II]/Hα ratio. Sources with ratio higher than 0.4 are considered as SNRs. This is an empirical diagnostic from SNRs identified in Small and Large Magellanic Clouds (SMC and LMC). However, this criterion is biased against low excitation SNRs, and as a result by using it, we miss systematically SNRs with low shock velocities, SNRs evolving in very dense media, or low metallicity media.

This led us to examine new diagnostics that are effective in the detection of low excitation SNRs. In order to do that, we combined shock and photoionization models that correspond SNRs and H II regions respectively. Using Support Vector Machines (SVM) as a classification method, we calculated lines and surfaces that separate shock from photoinization models in 2 and 3 dimensions respectively, where each dimension is an emission line ratio. The quality of the diagnostic depends on the best separation (highest completeness of shock models) and lowest contamination by photoionization models. We also propose a 1D diagnostic for SNR identification, that uses the [O I]λ6300Å line and is more effective in low excitation SNRs. These new diagnostics, can increase the number of identified SNRs up to $\sim 30\%$ compared to the [S II]/Hα criterion.

In order to test the accuracy of these diagnostics, we compared them with observational data. We used spectra of SNRs and H II regions (extra-galactic or spectra of regions of Galactic SNRs) and we find very good agreement in recovering the true nature of the sources (between $\sim 89\%$ and $\sim 99\%$). We also explored the efficiency of the diagnostics in different matallicities. The shock and photoionization models that we used are based on a wide range of metallicities: subsolar (SMC, 0.25×solar; LMC, 0.5×solar), solar and supersolar (2×solar). We find that there is higher incompleteness for the shock models (i.e. the fraction of shock models that are not included in the locus of SNRs) in supersolar-metallicity models, especially for the diagnostics that contain oxygen lines. This happens because higher metallicity SNRs present strong temperature gradients resulting in a wider range of oxygen-line values extended also to values beyond that separating surface or line that distinguishes SNRs from H II regions.

We have also examined possible contamination in our diagnostics by other objects and biases. A category of SNRs that we miss using these diagnostics (but also with the [S II]/Hα diagnostic) is the Balmer SNRs. These SNRs are characterized by weak or absent forbidden lines, and strong Balmer lines and thus we do not expect to identify them. However, this category is only a small fraction of optically emitting SNRs. On the other hand, planetary nebulae and Herbig-Haro (HH) objects produce forbidden lines. Although planetary nebulae present strong [O III] lines, they produce very weak [S II], [O I],and [N II] lines, which would place them in the high-excitation end of the H II regions. The shock excited HH objects, present very low luminosities, rendering them un-observable in extra-galactic surveys. In our Galaxy or in LMC and SMC, we could discriminate them from their morphology.

Although one needs diagnostic criteria like the aforementioned as indicators of the total populations of SNRs, [S II]/Hα provides secure samples of higher excitation SNRs and it is useful for comparisons with previous studies. However, the results of any source population are subject to the sensitivity of the observations and selection effects. Hence, in order to compare results from different studies, they must be free of selections effects. In our second work, we identify SNRs in four nearby galaxies (NGC 45, NGC 55, NGC 1313, and NGC 7793) following an automated method that allows us to quantify incompleteness effects. We calculated the incompleteness as function of the Hα and [S

II] luminosities, taking also into account the different backgrounds within the galaxies.

In these galaxies, using the [S II]/Hα > 0.4 criterion, we identified 43 candidate SNRs (30 of which are new identifications) which we consider as more secure sample, 54 possible candidate SNRs (less secure sample), and 21 larger structures that can be super-bubbles or more evolved SNRs. For our analysis we used only the more secure sample. We constructed the Hα and the joint Hα - [S II] luminosity functions for the incompleteness corrected data. The Hα luminosity function (LF) is described by a skewed Gaussian with a skewness of 1.7. The skewness is the result of the strict filter that we have set in our analysis, according to which, we keep sources for which the [S II]/Hα ratio is 3σ above the 0.4 threshold. The mean of the skewed Gaussian fitted to the Hα LF is $\mu(\log(\mathrm{L}/10^{36}\,\mathrm{erg\,s^{-1}})) = 0.07$ and the sigma is $\sigma(\log(\mathrm{L}/10^{36}\,\mathrm{erg\,s^{-1}})) = 0.58$.

The joint Hα - [S II] luminosity function is described by the combination of a skewed Gaussian and a truncated Gaussian. The Skewed Gaussian describes the density of the sources along the "spine" of the distribution of the candidate SNRs on the [S II]-Hα plane. The truncated Gaussian describes the spread of the sources around the "spine", i.e. the width of the LF. This width is $\sigma(\log(\mathrm{L}/10^{36}\,\mathrm{erg\,s^{-1}})) = 0.14$. The best fit parameters of the skewed Gaussian are $-0.03, 0.48$, and 1.73 for the mean, sigma, and skewness respectively in units of $\log(\log(\mathrm{L}/10^{36}\,\mathrm{erg\,s^{-1}}))\,\mathrm{erg\,s^{-1}}$ along the "spine" line: $\mathrm{L} = 0.88\log(\mathrm{L_{H\alpha}}) - 0.06$.

In addition, we have introduced the excitation function which is described by the [S II]/Hα ratio and it provides information on the degree of excitation of SNR populations. More specifically, we calculated the orthogonal distance of each source on the Hα - [S II] plane from the [S II]/Hα=0.4 line. This calculation shows that there is a trend for more luminous SNRs to have lower excitation. This is probably the result of more luminous SNRs being in denser regions or embedded in H II regions.

Samples free of selection effects, as the ones we described, can be also compared with theoretical models. In our third project, we develop for the first time, models on SNR populations. We use shock models in order to construct the Hα and the joint [S II] - Hα luminosity functions of SNRs under a range of ISM conditions based on a simple model for their evolution. By treating the luminosity function as a probability distribution, we can calculate the probability for an SNR to have a certain Hα luminosity given a shock velocity, ISM density, and age. We include in this calculation a simple model for SNR evolution based on the Sedov-Taylor solution. Such models can be used to estimate physical parameters of the SNRs, that we cannot measure directly, by comparing observational with theoretical luminosity functions.

The results of this analysis are very promising despite the simplicity of our approach. For example, we recover the expected behavior that higher densities and shock velocities give higher probabilities for more luminous SNRs, while there is very low probability to obtain a low luminosity SNR with high shock velocity and in a high density region.

Remarkably, we find very good agreement between the theoretical LFs and the observed Hα LF presented in Chapter 2. In the case of the joint Hα-[S II] LF we find good agreement between the models and the observed LF when we consider a wider range of magnetic fields.

Concluding, all of the projects presented in this thesis, set the foundation for a more systematic study of the different SNRs populations (not only the high excitation SNRs), and the objective comparison between different studies or between observational results and theoretical models. We also set the framework for population synthesis models of SNRs, which will make the study of their physics and their feedback to the ISM more effective.

5.2 Future work

Our future work focuses mainly on making our models more accurate, considering more parameters that better describe the real physical conditions, and on their application on real data. Thus, more specifically our future goals are:

1) To expand our diagnostics and the shock models to more realistic ISM conditions, for example to account also for SNRs embedded in H II regions, and to develop velocity diagnostics.

2) Perform spectroscopic analysis of the candidate SNRs in order to confirm their shock excited nature, apply the multi-dimensional diagnostics and measure their physical properties (e.g. density, velocity).

3) To calculate the theoretical luminosity functions considering a more complete evolutionary sequence for SNRs (not only the Sedov-Taylor phase.)

4) To add more dimensions (i.e. more emission lines) to the theoretical models, which will enable us to discriminate between different distributions for the underlying physical parameters (e.g. density or magnetic field distribution).

5) To test the theoretical models using Galactic SNRs for which the physical parameters

can be measured more accurately.
6) To explore the high-energy emission of the SNRs in the galaxies that we identified the optical SNRs, analyzing X-ray data and to look for correlations between the optical SNRs and X-ray emission.

Bibliography

Achterberg A., Ball L., 1994, A& A, 285, 687 48, 69

Allen M. G., Groves B. A., Dopita M. A., Sutherland R. S., Kewley L. J., 2008, ApJS, 178, 20 xix, 18, 19, 20, 28, 74, 80, 81, 82, 83

Arbutina B., Urošević D., 2005, MNRAS, 360, 76. doi:10.1111/j.1365-2966.2005.09033.x 72, 89

Annunziatella M., Mercurio A., Brescia M., Cavuoti S., Longo G., 2013, PASP, 125, 68 50

Asvarov A. I., 2014, A&A, 561, A70. doi:10.1051/0004-6361/201322774 2

Baldwin, J. A., Phillips, M. M., & Terlevich, R. 1981, PASP, 93, 5 36

Ballet J., 2006, AdSpR, 37, 1902. doi:10.1016/j.asr.2005.03.047 90

Bell A. R., Schure K. M., Reville B., 2011, MNRAS, 418, 1208. doi:10.1111/j.1365-2966.2011.19571.x 13

Bell A. R., 1978, MNRAS, 182, 147. doi:10.1093/mnras/182.2.147 13

Bell A. R., 1978, MNRAS, 182, 443. doi:10.1093/mnras/182.3.443 13

Berg, D. A., Skillman, E. D., Croxall, K. V., et al. 2015, ApJ, 806, 16 32

Bertin, E., & Arnouts, S. 1996, A&AS, 117, 393 50

Bibby J. L., Crowther P. A., 2010, MNRAS, 405, 2737. doi:10.1111/j.1365-2966.2010.16659.x 51

Binder B., Williams B. F., Eracleous M., Plucinsky P. P., Gaetz T. J., Anderson S. F., Skillman E. D., et al., 2015, AJ, 150, 94 48, 69

Binette, L., Dopita, M. A., & Tuohy, I. R. 1985, ApJ, 297, 476 19

Blair W. P., Chandar R., Dopita M. A., Ghavamian P., Hammer D., Kuntz K. D., Long K. S., et al., 2014, ApJ, 788, 55. doi:10.1088/0004-637X/788/1/55 67

Blair, W. P., Winkler, P. F., & Long, K. S. 2013, ApJS, 207, 40 2, 18

Blair, W. P., Winkler, P. F., & Long, K. S. 2012, ApJS, 203, 8 18

Blair W. P., Long K. S., 2004, ApJS, 155, 101. doi:10.1086/423958 69

Blair W. P., Long K. S., 1997, ApJS, 108, 261. doi:10.1086/312958 2, 17, 46, 48, 51, 67, 79

Blair W. P., Long K. S., 1997, ApJS, 108, 261. doi:10.1086/312958

Blair, W. P., Kirshner, R. P., & Chevalier, R. A. 1982, ApJ, 254, 50

Boumis P., Xilouris E. M., Alikakos J., Christopoulou P. E., Mavromatakis F., Katsiyannis A. C., Goudis C. D., 2009, A&A, 499, 789. doi:10.1051/0004-6361/200811474 1, 17, 45, 79

Boumis P., Meaburn J., López J. A., Mavromatakis F., Redman M. P., Harman D. J., Goudis C. D., 2004, A&A, 424, 583

Bresolin, F. 2007, ApJ, 656, 186 32

Castellanos M., Díaz A. I., Terlevich E., 2002, MNRAS, 329, 315. doi:10.1046/j.1365-8711.2002.04987.x 32, 51

Cioffi D. F., McKee C. F., Bertschinger E., 1988, ApJ, 334, 252. doi:10.1086/166834 14, 15, 74

Colbert E. J. M., Petre R., Schlegel E. M., Ryder S. D., 1995, ApJ, 446, 177 48, 69

Condon J. J., Yin Q. F., 1990, ApJ, 357, 97. doi:10.1086/168894 45

Cox D. P., Smith B. W., 1974, ApJL, 189, L105. doi:10.1086/181476 14

Daltabuit, E., Dodorico, S., & Sabbadin, F. 1976, A&A, 52, 93 18

Ddelaney T., Rudnick L., 2002, cosp, 34, 2438

Della Bruna L., Adamo A., Bik A., Fumagalli M., Walterbos R., Östlin G., Bruzual G., et al., 2020, A&A, 635, A134 48

Desai K. M., Chu Y.-H., Gruendl R. A., Dluger W., Katz M., Wong T., Chen C.-H. R., et al., 2010, AJ, 140, 584. doi:10.1088/0004-6256/140/2/584 14

Dodorico, S., Benvenuti, P., & Sabbadin, F. 1978, A&A, 63, 63 18, 27

Dopita M. A., Blair W. P., Long K. S., Mutchler M., Whitmore B. C., Kuntz K. D., Balick B., et al., 2010, ApJ, 710, 964. doi:10.1088/0004-637X/710/2/964 18, 67

Dopita, M. A., Groves, B. A., Fischera, J., et al. 2005, ApJ, 619, 755 20

Dopita, M. A., Groves, B. A., Sutherland, R. S., Binette, L., & Cecil, G. 2002, ApJ, 572, 753 19

Draine B. T., 2011, piim.book 9, 67, 74, 80

Dubner G., Giacani E., 2015, A&ARv, 23, 3. doi:10.1007/s00159-015-0083-5 13

Dufour, R. J. 1975, ApJ, 195, 315 32

Edmunds M. G., 2017, hsn..book, 2455. doi:10.1007/978-3-319-21846-5_24 14

Esteban, C., Bresolin, F., Peimbert, M., et al. 2009, ApJ, 700, 654 32

Evans, I. N., & Dopita, M. A. 1985, ApJS, 58, 125 36

Fesen R. A., Neustadt J. M. M., How T. G., Black C. S., 2019, MNRAS, 486, 4701

Fesen, R. A., Blair, W. P., & Kirshner, R. P. 1985, ApJ, 292, 29 18, 32, 36, 72, 74, 79

Fich, M., & Silkey, M. 1991, ApJ, 366, 107 32

Fioc, M., & Rocca-Volmerange, B. 1997, A&A, 326, 950 19

Franchetti N. A., Gruendl R. A., Chu Y.-H., Dunne B. C., Pannuti T. G., Kuntz K. D., Chen C.-H. R., et al., 2012, AJ, 143, 85. doi:10.1088/0004-6256/143/4/85 67

Green D. A., 2019, JApA, 40, 36. doi:10.1007/s12036-019-9601-6 1, 13, 18, 45

Green, D. A. 2017, VizieR Online Data Catalog, 7278 18

Groves, B. A., Allen, M. G. 2013, ITERA: Tool for Emission-line Ratio Analysis. Astrophysics Source Code Library, ascl:1307.012 19

Groves, B. A., & Allen, M. G. 2010, New A, 15, 614 19

Groves, B. A., Dopita, M. A., & Sutherland, R. S. 2004, ApJS, 153, 9 19

Heng, K. 2010, PASA, 27, 23 36

Hummel, E., Dettmar, R.-J., & Wielebinski, R. 1986, A&A, 166, 97 48

Ivezić, Ž, Connolly, A. J., VanderPlas, J. T. & Gray, A. 2014, "Statistics, Data Mining and Machine Learning in Astronomy", Princeton University Press 21

Jiménez S., Tenorio-Tagle G., Silich S., 2019, MNRAS, 488, 978. doi:10.1093/mnras/stz1749 74

Kennicutt R. C., Lee J. C., Funes J. G., J. S., Sakai S., Akiyama S., 2008, ApJS, 178, 247 47

Kewley, L. J., Dopita, M. A., Sutherland, R. S., Heisler, C. A., & Trevena, J. 2001, ApJ, 556, 121 18, 19

Koo B.-C., Kim C.-G., Park S., Ostriker E. C., 2020, ApJ, 905, 35. doi:10.3847/1538-4357/abc1e7 14

Kopsacheili M., Zezas A., Leonidaki I., Boumis P., 2021, MNRAS, submitted 80, 85, 86, 87, 88, 89

Kopsacheili M., Zezas A., Leonidaki I., 2020, MNRAS, 491, 889. doi:10.1093/mnras/stz2594 72, 74, 83

Kwitter, K. B. & Aller, L. H. 1980, MNRAS, 195, 939 32

Lee M. G., Sohn J., Lee J. H., Lim S., Jang I. S., Ko Y., Koo B.-C., et al., 2015, ApJ, 804, 63. doi:10.1088/0004-637X/804/1/63 32, 36, 46

Lee, J. H., & Lee, M. G. 2014, ApJ, 786, 130 xix, xix, 18, 67, 70, 71, 73

Lee J. H., Lee M. G., 2014, ApJ, 793, 134. doi:10.1088/0004-637X/793/2/134 xix, xix, 67, 70, 71, 73

Leitherer, C., Schaerer, D., Goldader, J. D., et al. 1999, ApJS, 123, 3 19

Leonidaki I., Boumis P., Zezas A., 2013, MNRAS, 429, 189. doi:10.1093/mnras/sts324 xix, xix, xix, 2, 17, 18, 27, 31, 32, 46, 51, 69, 70, 71, 73, 79

Leonidaki I., Zezas A., Boumis P., 2010, ApJ, 725, 842. doi:10.1088/0004-637X/725/1/842 17, 46, 47, 69

Levesque, E. M., Kewley, L. J., & Larson, K. L. 2010, AJ, 139, 712 19

Lima-Costa F., Martins L. P., Rodríguez-Ardila A., Fraga L., 2020, A&A, 642, A203. doi:10.1051/0004-6361/202038088 51

Lin Z., Hu N., Kong X., Gao Y., Zou H., Wang E., Cheng F., et al., 2017, ApJ, 842, 97. doi:10.3847/1538-4357/aa6f14 51

Long K. S., Winkler P. F., Blair W. P., 2019, ApJ, 875, 85. doi:10.3847/1538-4357/ab0d94 32, 46, 69, 79

Long, K. S., Blair, W. P., Milisavljevic, D., Raymond, J. C., & Winkler, P. F. 2018, ApJ, 855, 140 18, 51

Maggi P., Filipović M. D., Vukotić B., Ballet J., Haberl F., Maitra C., Kavanagh P., et al., 2019, A&A, 631, A127. doi:10.1051/0004-6361/201936583

Maggi P., Haberl F., Kavanagh P. J., Sasaki M., Bozzetto L. M., Filipović M. D., Vasilopoulos G., et al., 2016, A&A, 585, A162. doi:10.1051/0004-6361/201526932 69

Maragkoudakis, A., Zezas, A., Ashby, M. L. N., & Willner, S. P. 2018, MNRAS, 475, 1485 35

Martizzi D., Faucher-Giguère C.-A., Quataert E., 2015, MNRAS, 450, 504. doi:10.1093/mnras/stv562 15

Massey, P., Strobel, K., Barnes, J. V., & Anderson, E. 1988, ApJ, 328, 315 51

Mathewson, D. S., & Clarke, J. N. 1973, ApJ, 180, 725 15, 18, 52, 74, 83

Matonick D. M., Fesen R. A., 1997, ApJS, 112, 49 xix, xix, xix, 31, 32, 67, 70, 71, 73

Matonick D. M., Fesen R. A., Blair W. P., Long K. S., 1997, ApJS, 113, 333. doi:10.1086/313061 79

Milisavljevic D., Fesen R. A., 2013, ApJ, 772, 134. doi:10.1088/0004-637X/772/2/134 1, 17, 45, 79

O'Brien A. N., Filipović M. D., Crawford E. J., Tothill N. F. H., Collier J. D., De Horta A. Y., Wong G. F., et al., 2013, Ap& SS, 347, 159 48, 69

Pannuti T. G., Swartz D. A., Laine S., Schlegel E. M., Lacey C. K., Moffitt W. P., Sharma B., et al., 2015, AJ, 150, 91 48, 69

Pannuti T. G., Schlegel E. M., Filipović M. D., Payne J. L., Petre R., Harrus I. M., Staggs W. D., et al., 2011, AJ, 142, 20 48, 69

Pannuti T. G., Duric N., Lacey C. K., Ferguson A. M. N., Magnor M. A., Mendelowitz C., 2002, ApJ, 565, 966 48, 69

Petre R., Okada K., Mihara T., Makishima K., Colbert E. J. M., 1994, PASJ, 46, L115 48, 69

Pettini M., Pagel B. E. J., 2004, MNRAS, 348, L59 47

Ramakrishnan V., Dwarkadas V. V., 2020, ApJ, 901, 119. doi:10.3847/1538-4357/abb087 69

Raymond J. C., Chilingarian I. V., Blair W. P., Sankrit R., Slavin J. D., Burkhart B., 2020, ApJ, 894, 108. doi:10.3847/1538-4357/ab886d 89

Reynolds S. P., 2017, hsn..book, 1981. doi:10.1007/978-3-319-21846-5_89 89

Riaz, B., Briceño, C., Whelan, E. T., & Heathcote, S. 2017, ApJ, 844, 47 36

Russell S. C., Dopita M. A., 1992, ApJ, 384, 508. doi:10.1086/170893

Russell, S. C., & Dopita, M. A. 1990, ApJS, 74, 93 32

Sabbadin, F., Minello, S., & Bianchini, A. 1977, A&A, 60, 147 36

Schlegel E. M., Petre R., Colbert E. J. M., 1996, ApJ, 456, 187 48, 69

Sedov L. I., 1959, sdmm.book 8

Slane, P., Smith, R. K., Hughes, J. P., & Petre, R. 2002, ApJ, 564, 284 45

Slavin J. D., Smith R. K., Foster A., Winter H. D., Raymond J. C., Slane P. O., Yamaguchi H., 2017, ApJ, 846, 77. doi:10.3847/1538-4357/aa8552 83

Smith I. A., Ryder S. D., Bottcher M., Tingay S. J., Stacy A., Pakull M., Liang E. P. 2007, ApJ, 669, 1130 48, 69

de Souza, R. S., Dantas, M. L. L., Costa-Duarte, M. V., Feigelson, E. D,. Killedar, M. Lablanche, P.-Y., Vilalta, R., Krone-Martins, A. ,Beck, R., Gieseke, F. 2017 MNRAS, 472, 2808 18

Stampoulis, V., van Dyk, D. A., Kashyap, V. L., & Zezas, A. 2019, MNRAS, 485, 1085 18, 35

Stasińska, G. 2005, A&A, 434, 507 27

Stasińska, G. 1980, A&A, 85, 359 27

Stasińka, G. 1978b, A&AS, 32, 429 27

Stobbart A.-M. Roberts T. P., Warwick R. S., 2006, MNRAS, 370, 25 48, 69

Sutherland, R. S., & Dopita, M. A. 1993, ApJS, 88, 253 19

Taylor G., 1950, RSPSA, 201, 159. doi:10.1098/rspa.1950.0049 8

Tsamis, Y. G., Barlow, M. J., Liu, X.-W., Danziger, I. J., & Storey, P. J. 2003, MNRAS, 338, 687 32

Tody D., 1993, ASPC, 52, 173 50

Tody D., 1986, SPIE, 627, 733. doi:10.1117/12.968154 50

Vanhala H. A. T., Cameron A. G. W., 1998, ApJ, 508, 291. doi:10.1086/306396 14

Vázquez, G. A., & Leitherer, C. 2005, ApJ, 621, 695 19

Vilchez, J. M. , & Esteban, C. 1996, MNRAS, 280, 720 32

Vink J., 2020, *Physics and Evolution of Supernova Remnants* 11, 90

Vink J., 2017, hsn..book, 2063. doi:10.1007/978-3-319-21846-5_92 12, 13, 90

Vink J., 2012, A&ARv, 20, 49. doi:10.1007/s00159-011-0049-1 69

Vink J., Laming J. M., 2003, ApJ, 584, 758. doi:10.1086/345832 90

Vink J., Bloemen H., Kaastra J. S., Bleeker J. A. M., 1998, A&A, 339, 201

Vogt, F. P. A., Dopita, M. A., Kewley, L. J., et al. 2014, ApJ, 793, 127 18

Vučetić, M. M., Arbutina, B., & Urošević, D. 2015, MNRAS, 446, 943 17, 71

Williams B. J., Katsuda S., Cumbee R., Petre R., Raymond J. C., Uchida H., 2020, ApJL, 898, L51. doi:10.3847/2041-8213/aba7c1 79

Williams B. J., Hewitt J. W., Petre R., Temim T., 2018, ApJ, 855, 118. doi:10.3847/1538-4357/aaadb6 12

Williams B. J., Temim T., 2017, hsn..book, 2105. doi:10.1007/978-3-319-21846-5_94 14

Williams B. J., Chomiuk L., Hewitt J. W., Blondin J. M., Borkowski K. J., Ghavamian P., Petre R., et al., 2016, ApJL, 823, L32

Williams B. J., Borkowski K. J., Reynolds S. P., Blair W. P., Ghavamian P., Hendrick S. P., Long K. S., et al., 2006, ApJL, 652, L33. doi:10.1086/509876 13

Zurita, A., & Bresolin, F. 2012, MNRAS, 427, 1463

Zurita A., Bresolin F., 2012, MNRAS, 427, 1463. doi:10.1111/j.1365-2966.2012.22075.x 32, 51

99

Declaration

I herewith declare that the work presented in this thesis is of the candidate alone, apart from the Chapters 2 and 3.

Chapter 2 is published in the Monthly Notices of the Royal Astronomical Society as: Kopsacheili M., Zezas A., Leonidaki I., 2020, MNRAS, 491, 889

Chapter 3 is submitted in the Monthly Notices of the Royal Astronomical Society as: Kopsacheili M., Zezas A., Leonidaki I., Boumis P., 2021

Heraklio, April 2021